Development of Novel Anti-reflection Coatings for Millimeter/Submillimeter-wave Telescopes and Optimization of Cosmic Microwave Background Instruments

A DISSERTATION
SUBMITTED TO THE FACULTY OF THE GRADUATE SCHOOL
OF THE UNIVERSITY OF MINNESOTA
BY

Qi Wen

IN PARTIAL FULFILLMENT OF THE REQUIREMENTS
FOR THE DEGREE OF
DOCTOR OF PHILOSOPHY

Advisor: Shaul Hanany

July, 2021

Acknowledgements

I would first like to thank my advisor, Shaul Hanany, for teaching me things including and beyond experimental cosmology. His attention to detail and persistence in the face of challenges are extraordinary. Throughout the years, he has been pushing me to improve myself in research, collaborating, public speaking and so on.

I want to thank my colleagues in Cosmolab - Christopher Geach and Karl Young, Chaoyun Bao and François Aubin, Reid Wagner, Kate Raach, and Wenqian Sun, Chiou Yang Tan, Xin Zhi Tan, Irene Moskowitz, Brandon Nguyen, Campbell Haasch, Daniel Helgeson - for their help, company, and probably also many joyful distractions in PAN 314. The memories with them of sharing snacks in group meetings, 'volunteering' each other for management tasks, doing science outreach in Minnesota State Fairs, etc., are fun and precious.

A lot of achievements described in this thesis would be impossible without collaborative efforts. I want to thank my collaborators in the ARC team, the PICO study team, and a number of proposal-writing teams; it was my pleasure to work with and learn from all of them. I want to send my special thanks to Tomotake Matsumura, who supported me in various ways from day one, and taught me a lot about how to become a better researcher; and to Aritoki Suzuki, who patiently answered (too) many questions from me about detector and readout technologies, and was willing to help whenever I asked.

I want to thank Prof. Keith Olive, Prof. Terry Jones, Prof. Robert Lysak for serving on my committee throughout my graduate school years and for reviewing

this thesis. I appreciate the generous supports they have provided, including helpful feedback for my research and recommendations for applying for teaching assistantship in the physics department.

To my dear friends: the years in graduate school could be intimidating without you. Thanks for being around!

Finally to my family, I would like to thank my parents for being supportive all the time. They are the reason that I have the courage to pursue what I have passion for. Xueyan Tang, my girlfriend (now fiancée!), has suffered the most in the last few years from my sometime negative emotions. In many of the dark days, she was the only reason that I smiled. Babe, thanks for loving me and making me happy.

Dedication

To my loving and supporting parents, Jingzhi Qiu and Xinyu Li.

Abstract

I report the development of the anti-reflection coatings (ARC) using laser ablated sub-wavelength structures (SWS) in millimeter and sub-millimeter (MSM) wavelengths. This technology provides a promising solution for broadband, cryogenically robust ARC on high-index materials (HIM) - alumina, sapphire and silicon - for a broad range of MSM telescopes.

The effective behaviors of SWS are studied using numerical simulations by finite element method. We observe complex behaviors of SWS when the pitch of SWS is not negligibly small compared to the electromagnetic wavelength. Based on the study, a practical guide to design optimal SWS ARC is provided.

Ultrashort pulsed lasers are used to fabricate SWS on HIM, majority of which are difficult to be modified by other traditional fabrication methods such as dicing and chemical etching. We have successfully ablated structures with height from a few hundred μm to around 2.5 mm. Excellent anti-reflection performances have been demonstrated by experimental measurements of transmittance/reflectance as well as by numerical simulations based on the measured structure shapes. Higher than 20 mm^3/min average ablation rates have been experimentally verified on alumina and sapphire through an optimization effort using a high-power picosecond laser. The demonstrated high rates strongly support the feasibility of laser ablated SWS ARC on large ($\geq$ 30 cm) optical elements.

A novel ablation model that relates the structure height and laser cumulative fluence is presented. Using a best-fit procedure with experimental data, for both alumina and sapphire, we find threshold fluence $\phi_{th} \approx 2$ J/cm^2 and average absorption length $\bar{\delta} \approx 650$ nm for peak fluence values between 30 and 70 J/cm^2. With the best-fit values, the model and data values for cumulative fluence agree to within 10%. The model is used to predict average ablation rate as a function of SWS height and average laser power.

I also report the results of several projects that aim to optimize cosmic microwave background instruments. These projects include (1) an optical design study of cross Dragone system for PICO, the Probe of Inflation and Cosmic Origins, a next-generation space telescope; (2) a mechanical design of the focal plane for PICO; (3) a trade study on the aperture size for Tau Surveyor, a balloon-borne instrument aiming to measure the optical depth to reionization τ; (4) development of low-conductance, lenslet coupled, multichroic bolometers for balloon-borne platforms.

Contents

List of Tables

List of Figures

Chapter 1

Introduction

Over the last few hundred years, humanity has been advancing the capabilities of telescopes to observe objects beyond our own planet. The ability of exploring the cosmos with telescopes in different wavelengths of light has tremendously enriched our understanding of the content and evolution of the Universe. For example, the measurements of the cosmic microwave background (CMB) in the millimeter and sub-millimeter (MSM) wavelengths, since the discovery of it in 1964 by Penzias and Wilson [1], have provided decisive evidences for a precise picture of a currently dark energy, dark matter dominated universe that originated from Big Bang [2].

MSM telescopes offer great opportunities to answer some unsolved fundamental questions in cosmology, astrophysics and particle physics. Probing imprints of the primordial gravitational waves on the CMB polarizations can provide insights of the cosmic inflation, a theoretically predicted period of nearly exponential expansion of the early universe during only a fraction of a second after the Big Bang [3, 4]. Better constraint of the optical depth to reionization through CMB polarization measurement on larger angular scales will improve the constraint on the neutrino masses [5], whose origin and structure remain unclear and suggest physics beyond the Standard Model of particle physics. Examining molecular clouds in the local universe helps us gain understanding of the star formation in

Milky Way and nearby galaxies [6, 7]. Imaging of the event horizon of supermassive black holes through very-long-baseline interferometry enables us to probe the general relativity in the strong-filed regime [8].

Modern telescopes are complex systems composed of many hardware and software components. The innovations and developments of these components made by scientists and engineers across generations are the building blocks of the continuous improvement in telescope performances. When exciting and sometimes puzzling scientific discoveries are made, new challenges are often created as well.

In recent years, to increase observing sensitivity, and to improve the foregrounds cleaning, many MSM experiments share a preferred strategy of employing high-throughput optics at cryogenic temperatures that feed multi-color pixels on the focal plane that are sensitive to multiple electromagnetic frequency bands [9–14]. This strategy demands the use of high-index materials (HIM), such as alumina, sapphire and silicon, to provide the high optical power needed while maintaining a low thermal emission contaminations. However, the development of broadband, cryogenically robust anti-reflection coatings (ARC) on these materials turned out to be a great challenge.

This thesis presents the development of the ARC on HIM using laser abated sub-wavelength structures (SWS). The motivations, concepts and design procedures of SWS ARC are discussed in Chapter 2. The experimental demonstrations of laser ablated SWS ARC and optimization of the average ablation rates are summarized in Chapter 3. In Chapter 4, an ablation model that describes the relation between structure shape and laser parameters is presented. This thesis also presents an optical design study and a mechanical design of the focal plane for PICO, a next-generation space MSM telescope, in Chapter 5. In Chapter 6, a trade study between one large-aperture telescope and multiple small-aperture telescopes contained within one receiver is given in the context of Tau Surveyor, a proposed balloon-borne experiment. The last Chapter 7 reports the experimental characterizations of low-conductance, multichroic detectors for balloon-borne telescopes.

Chapter 2

SWS ARC: Coating Designs

In recent years, alumina, sapphire and silicon, which we call HIM, have increasingly drawn attention for their uses in MSM astrophysical instruments. HIM have high refractive indices which enable the lenses made out of them to provide high optical correction power. HIM also have the lowest absorptive losses and the highest thermal conductivities among all MSM materials. These physical properties make HIM ideal materials to be used for lenses, filters and wave plates in modern cryogenic MSM instruments.

However, the high refractive indices of HIM, combined with their strong hardness and much different thermal contractions compared to commonly used coating materials, create great challenges in design and fabrication of cryogenically robust ARC. Many current and next-generation MSM experiments that strive for probing the signal of primordial gravitational waves are demanding solutions for broadband ARC on HIM.

This chapter discusses the basics of reflective loss, the traditional ARC methods and their limitations when used on HIM. The SWS are introduced as a promising solution for achieving broadband and cryogenically robust ARC on HIM. The rest part of this chapter focuses on the use of effective medium theory to quantitatively understand and to design SWS.

2.1 High-index Materials and Reflective Loss

The sensitivity of a telescope depends on its ability of collecting photons from astronomical sources of interest. To increase sensitivity, many MSM experiments utilize optical systems that feed detector arrays with thousands of pixels [9, 13, 15–20]. Such high-throughput optical designs require high corrective power from the optical elements, which are often at cryogenic temperatures, to maximize the aberration-limited focal plane areas. Similar to the cameras that people use daily, many astronomical telescopes take advantages of lenses to efficiently correct the optics given limited instrument space. The preferred lens materials are silicon and alumina, as now adopted by Advanced ACT, SPT3G, POLARBEAR-2, SO, CMB-S4, AliCPT [9, 13, 15, 17–19], thanks to their high refractive indices, see Table 2.1.

HIM have other superior properties, comparing to plastics as shown in Table 2.1, that make them desirable to be used for lenses, filters and wave plates in MSM astronomical instruments. At cryogenic temperatures, HIM have lower loss tangent, which indicates lower absorption loss through the optical path. HIM have much higher thermal conductivities, which help maintain the cryogenic temperatures more uniformly over the entire surface of these refractive optical elements. The ability of efficiently heat sinking an entire optical element is especially important for large-aperture designs; AliCPT chose alumina as the lens material for their 80 cm lenses [18]. Sapphire is birefringent, which makes it a good half-wave plate (HWP) material. Sapphire HWPs have been and will be used in several experiments [11, 20, 21]

Alumina, in particular, is a good thermal filter material for MSM instruments to reject THz emissions. In Figure 2.1, I plot the loss tangent data of 99.5% alumina measured at $T = 30$ K and $T = 300$ K from a series of experiment conducted by Inoue et al. [22, 23]. From the measured data at 30 K, it can be seen that at cryogenic temperature, alumina's loss tangent stays low and flat at around 4E-4 up to about 600 GHz, then increases to about 2E-3 close to 2 THz.

An ideal thermal filter is the one that rejects out-of-band emission but allows in-band transmission. Due to lack of measurement at other temperatures that I could find in literature, I fit the data with a toy model as shown below

$$\tan\delta = Max(4\times10^{-4},\ 2.5\times10^{-7}\ T^{0.43}\nu), \tag{2.1}$$

where ν is the frequency in the unit of GHz. The predicted results using the model at different temperatures are shown by the lines. Based on the model, at $T = 40$ K, alumina needs to be about 10 mm thick to absorb 99% of light at 2 THz.

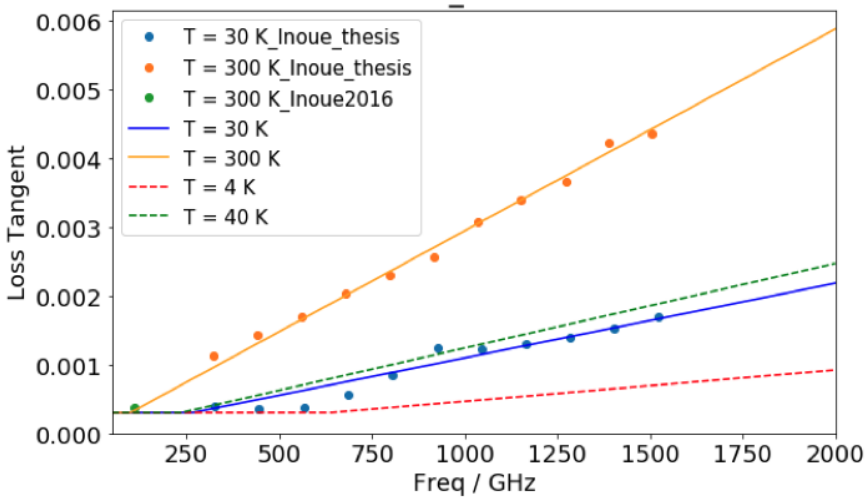

Figure 2.1: Loss tangent vs frequency at different temperatures. The points are measurements, while lines are the prediction based on Eq. 2.1.

However, the price to pay for using HIM for refractive optical elements is the high reflection caused by their high refractive indices.

The losses of the photons due to a refractive optical element are quantified by the transmittance T, the refletance R, and the absorptance A, which are the ratios of the transmitted, reflected and absorbed over the incident power respectively. The relationship among these quantities is that $T + R + A = 1$. In the following discussions in this chapter, I neglect the absorptance, i.e. let $A = 0$, unless

Material	**Refractive index**	**Loss tangent**[a]($\times 10^{-4}$)		**Thermal conductivity**[c]	**Thermal contraction**[c]
		300 K	77 K	[W/ m K]	$\mathbf{\Delta L/L}$ (%)
HDPE	1.5	2 - 4	1 - 2[b]	0.8	1.9
Teflon/PTFE	1.4	2 - 7	1 - 3[b]	0.23	1.9
Alumina	3.1	3 - 20	0.3 - 3	160	0.063
Sapphire	O 3.1; E 3.4[d]	2 - 10	0.03 - 0.5	1100	0.077
Silicon	3.4	0.1 - 2	0.1 - 1	1000	0.023
References	[24]	[24, 25]	[23, 25–28]	[29–32]	[29, 33]

a Measured at 300 GHz or nearby. Range of values indicate spread of measurements.
b Extrapolated based on the power law in temperature measured between 28 K and 84 K at 18 GHz.
c Thermal conductivity measured at 77 K or nearby; thermal contraction measured from 293 K to 77 K.
d Sapphire is birefringent

Table 2.1: Summary of materials widely used for optical elements in the MSM wave band. Among these materials, HIM have lower loss at cryogenic temperatures, higher thermal conductance, and small thermal contraction.

specifically stated otherwise. We will have more discussions about absorption in later chapters where we look at some practical applications.

The most important parameter that determines T and R is the refractive index n of the material of the optical element. To understand the dependence of T and R on the refractive index quantitatively, we look at the simplest model of a refractive optical element: a flat substrate in the vacuum with index n and with thickness t. For this simple model, one can derive from Maxwell's equations and find that at normal incidence:

$$T = \frac{4n^2}{4n^2 + (n^2-1)^2 \sin^2(2\pi nt/\lambda)}, \tag{2.2}$$

$$R = 1 - T = \frac{(n^2-1)^2 \sin^2(2\pi nt/\lambda)}{4n^2 + (n^2-1)^2 \sin^2(2\pi nt/\lambda)}, \tag{2.3}$$

where λ is the wavelength. It is easy to see that when $\sin(2\pi nt/\lambda) = 0$, $T = 1$ and $R = 0$. When $\sin(2\pi nt/\lambda) = \pm 1$,

$$T = \frac{4n^2}{(n^2+1)^2} \equiv T_{min}, \tag{2.4}$$

$$R = \frac{(n^2-1)^2}{(n^2+1)^2} \equiv R_{max}. \tag{2.5}$$

Note that the expression of R_{max} is different from the well-known Fresnel equation

$R = \frac{(n-1)^2}{(n+1)^2}$ for normal incidence, where the latter quantifies the reflection when there is only one interface between vacuum and the material.

We can also use the Transfer Matrix Method (TMM) [34], a standard way to theoretically calculate T and R given arbitrary number of layers of medium. TMM calculations depend on the indices of all layers, including that of the ambient environment which is assumed to be 1 throughout this thesis, and on the thickness of the layers, the frequency of the EM waves, the polarization, and the incident angle. Figure 2.2 shows a couple of examples of the transmittance v.s. frequency calculated by TMM. Both examples assume normal incidence, and the only difference in the inputs between the two is the refractive index of the material. The results show that the transmittance oscillates between 1 and $1 - R_{max}$, as defined in Eq. 2.5, with a fringe pattern that depends on the index n.

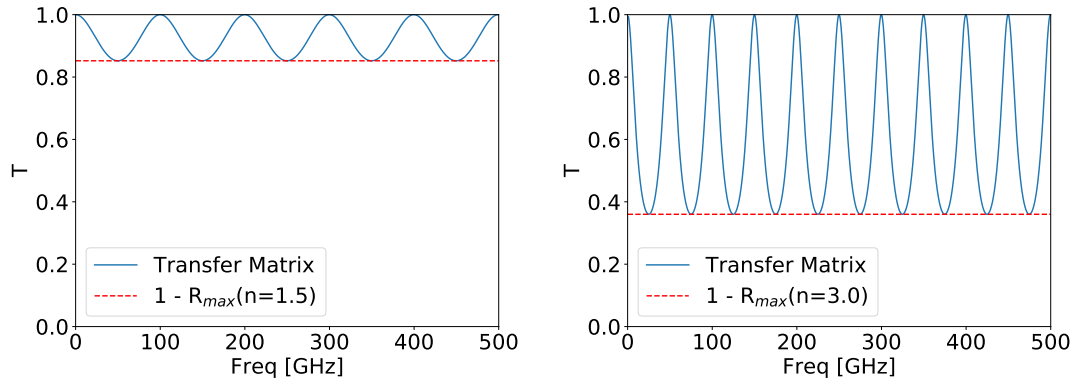

(a) (b)

Figure 2.2: (a) The blue curve shows the transmittance as a function of photon frequency for normal incidence calculated by the TMM, assuming a 1 mm thick layer with refractive index $n = 1.5$; the red horizontal dashed line is calculated by $1-$ Eq. 2.5. (b) Same as (a) except that the refractive index $n = 3.0$.

Figure 2.3 shows the calculation of R_{max} based on Eq. 2.5 for various refractive indices, which cover the index range of interest as mentioned in the last paragraph. Clearly, a larger refractive index leads to larger reflection. For example, HIM, which have refractive indices $n > 3$, can cause reflection as large as more than

60%. In real applications, the average transmittance over the observing bandwidth is more relevant. According to Figure 2.2, over a broad band covering multiple 'fringes' of the T vs Freq, the average reflectance is roughly half of R_{max}, which is still more than 30% for $n > 3$. Moreover, there are typically more than just one HIM optical element along the optical path. Such losses of photons due to the reflection would cause significant deterioration of the sensitivity of a telescope.

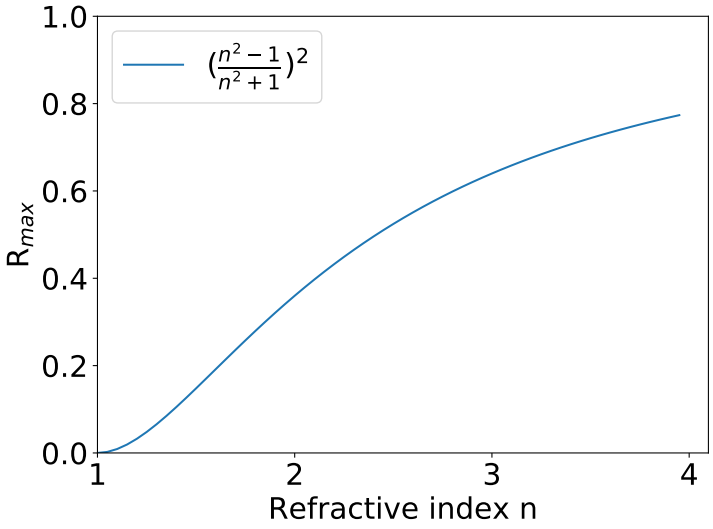

Figure 2.3: R_{max} as a function the refractive index of the material for normal incidence.

The large reflection would also cause systematic effects for MSM instruments. When light has oblique incidence on the material surfaces, two orthogonal polarizations are reflected differently [34]. Such differential reflectance is proportional to the overall reflection, and causes 'instrumental polarization', defined as the conversion of unpolarized to polarized light by the instrument. Since the B-mode signal is fainter by at least a factor of 1,000 relative to the CMB temperature anisotropy, the instrument polarization needs to be controlled to sub-percent accuracy. Therefore, minimizing reflections is crucial for controlling the systematics caused by the instrument polarization. Additionally, the large reflections lead to light bouncing

between optical elements inside an instrument and generate non-negligible ghost rays. Such effects have been reported in ALMA instruments [35, 36].

In conclusion, HIM provide many desired properties for being used as the refractive optical elements in MSM instruments, but without effective ARC the high reflection from HIM could cause significant sensitivity deterioration and systematic effects.

2.2 Broadband ARC

In recent years, multi-color pixel (MCP) technology, which enables each pixel on the focal plane to be sensitive to multiple frequency bands, has been adopted by many MSM experiments to more efficiently use the aberration-limited focal plane areas. This means that in an optical system the same optical path is shared by different frequency bands, and thus the overall frequency bandwidth of the optical system needs to be broad. Such requirement applies to all the optical elements inside an instrument, including all the ARCs. The fractional bandwidth, defined as the frequency bandwidth divided by the central frequency, of an individual single-color pixel is typically around 25%, while with MCP technology it is often required to be around 100% [9, 10, 17] or even above [20].

Given the challenges described above and in the last section, a desired design of the ARC applied on the HIM in many MSM instruments needs to be (1) **broadband**; (2) **cryogenically robust**, since the HIM optical elements typically work at cryogenic temperatures; (3) **effective in reflection reduction**, meaning it should suppress the in-band maximum reflectance R_{max} from above 60% without ARC down to at least below 10 % with ARC.

2.2.1 Multi-layer ARC

The simplest ARC is a single-layer $\lambda/4$ coating. With a layer of an additional material added between the air and the substrate, the reflection is reduced to

zero at the wavelength λ if: (1) the refractive index of the coating material is equal to the square root of the index of the substrate, i.e. $n_{ARC} = \sqrt{n_{sub}}$; (2) the coating thickness d is such that the optical path through the coating, i.e. $n_{ARC}d$, is equal to $\lambda/4$. Figure 2.4 shows the transmittance as a function of frequency with and without a $\lambda/4$ coating that is designed at 150 GHz. The two panels are calculated using the same coating but with two different thickness of the substrate. The results show that the reflectance is reduced to 0 at 150 GHz, but increases while the frequency deviates from 150 GHz. One of the major limitations of a single-layer $\lambda/4$ coating is its narrow ARC bandwidth.

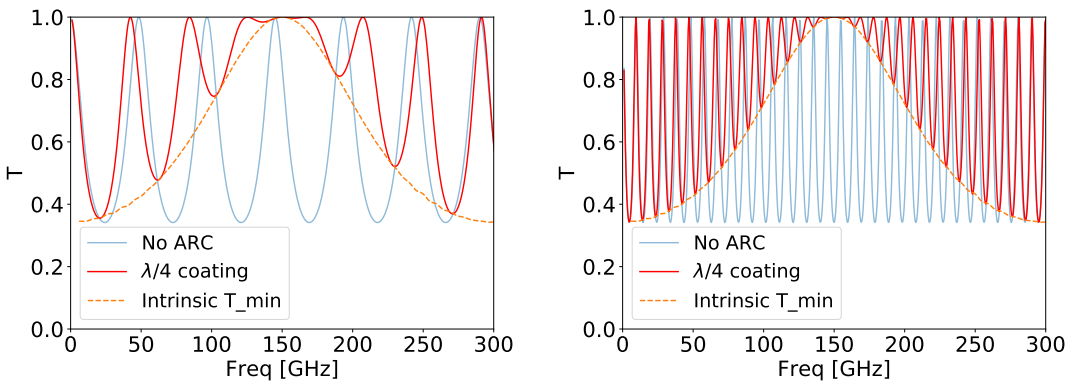

Figure 2.4: Transmittance predicted using TMM, with and without a $\lambda/4$ coating designed at 150 GHz on both sides of the substrate. The refractive index of the substrate n_{sub} is assumed to be $n_{sub} = 3.1$, and the thickness of the substrate t_{sub} is assumed to be (a) $t_{sub} = 1$ mm and (b) $t_{sub} = 5$ mm. The orange curves are the same cubic spline interpolation of the local minima assuming a $t_{sub} = 10$ mm substrate thickness.

We set criterion on the transmittance to quantify the ARC bandwidth. If one requires $T \geq 90\%$ within the entire ARC band, the ARC bandwidth in each panel of Figure 2.4 turns out to be (a) between 115 and 180 GHz and (b) between 122 and 178 GHz; or 43.3% and 37.3% respectively in terms of the fractional bandwidth. The difference in the ARC bandwidth between the two panels is

because that the transmittance depends on the phase of the EM waves, which depends on the thickness of the substrate.

On the other hand, the intrinsic minimum transmittance of a coating does not depend on the phase of the EM waves. For example, the same orange dashed curve that represents the intrinsic minimum transmittance is plotted in both panels in Figure 2.4. The orange dashed curve was obtained numerically by interpolating the local minima of T vs frequency with a cubic spline interpolation [37]. A thicker $t_{sub} = 10$ mm substrate was assumed for the interpolation because thicker samples provide more 'fringes' and therefore more local minima for higher accuracy. How the number of local minima affects the accuracy of the interpolation is an interesting topic, but it is beyond the scope of the discussion. In Figure 2.4, the intrinsic minimum transmittance obtained agrees well with the local minima in both panels with thinner substrates. Using the intrinsic minimum transmittance, denoted as T_{min}, the bandwidth where the $T_{min} \geq 90\%$ is between 123.0 and 177.5 GHz, or 36.3% fractional bandwidth. Such a definition of the ARC bandwidth using the intrinsic minimum transmittance provides an objective indicator for the minimum bandwidth achievable by a coating regardless of the exact phase of the EM waves. This becomes especially useful when comparing different ARC designs.

Multi-layer ARC provide broader ARC bandwidth than single-layer ARC. Multi-layer ARC have several layers of different materials with selective refractive indices, which gradually vary between the index of the air and the index of the substrate. The most common selections of the refractive indices for multi-layer ARC are Chebyshev (or "equal-ripple") and Binomial (or "maximally flat"), which are well studied for impedance matching in transformers [38, 39]. Figure 2.5 shows the predicted anti-reflection performances with multi-layer ARC. Because of the symmetry in transmittance around the central frequency, the theoretical upper limit of the fractional bandwidth for multi-layer index profiles is 200%.

Despite of having very effective ARC index profiles in theory, the multi-layer ARC approach creates challenges in finding the suitable coating materials for HIM. For modern MSM astronomical instruments, the ideal multi-layer ARC coating

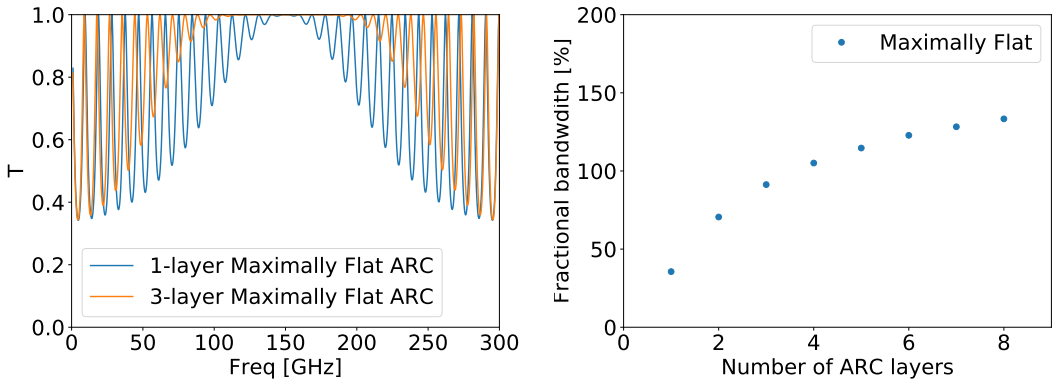

(a) (b)

Figure 2.5: The TMM predicted performance of multi-layer ARC using "Maximally Flat" index profiles on a substrate with $n_s = 3.1$. (a) Transmittance as a function of frequency assuming a 5 mm substrate thickness. (b) Fractional bandwidth as a function of the number of coating layers, for where the intrinsic minimum transmittance $T_{min} \geq 0.9$.

materials are required to have following properties:

- low absorption in the mm/sub-mm bandsl
- specific thickness and refractive indices that closely match the index profiles;
- similar thermal expansion coefficients to that of the substrate material.

Many plastic materials, such as HDPE and Teflon, may satisfy the first two requirements but not the third, as shown in the Table 2.1. Modern mm/sub-mm astronomical instruments have optical elements operating at very low temperatures, e.g. below 77 K. Therefore, the ARC have to be cryogenically robust during the cooling-down and warming-up processes between the room temperature and cryogenic temperatures. The differential thermal expansions among different materials during the cryogenic cycles create great challenges for developing robust multi-layer ARC.

2.2.2 SWS ARC

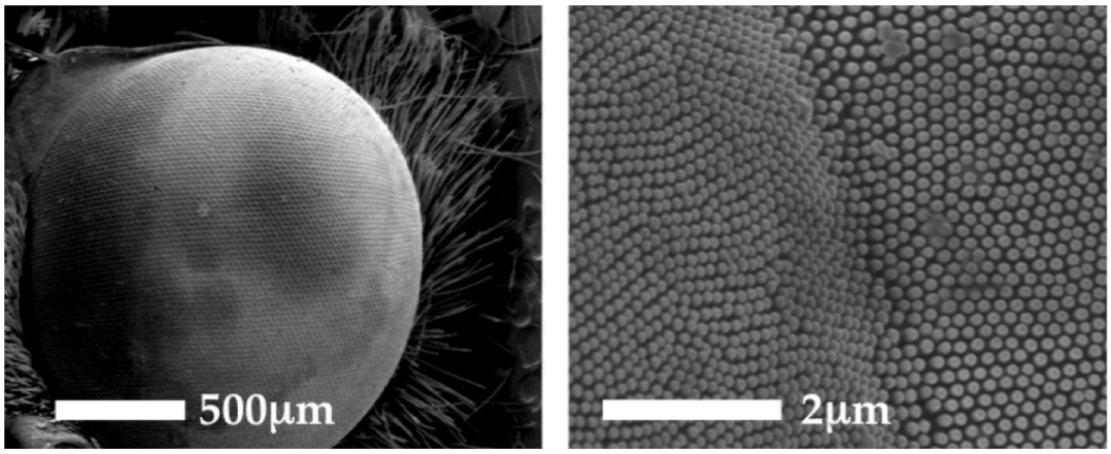

Figure 2.6: SEM images of a moth eye showing the sub-micron structures that give the moth eye its anti-reflective behavior.

Nature often has the best strategies for solving hard problems, and it turned out that the ARC is another great example of the biomimetic inspirations that humans can learn from nature [40, 41]. Figure 2.6 shows the SEM images of a moth's eye [42], and reveal that there are nanostructure patterns or SWS on the cornea. Because the structure pattern size is smaller than the wavelength, light interact with these SWS as if there are effective refractive indices gradually changing from the index of the air to the index of the material at the bottom. Such a gradient change of the effective refractive indices leads to reduction of reflection from the moths' eyes over a broad band, and therefore not only helps moths avoid being found by predators but also improves moths' visions in dark environment.

The SWS ARC is a technique that mimics the moth-eye anti-reflection strategy. By having an array of periodic structures with structure pitch that is smaller than the wavelengths of interest, SWS ARC synthesizes effective refractive index profiles that reduce the reflection. The effective refractive indices depend on the shape of SWS as well as the wavelength. The "translation" between physical

shape of SWS and the effective refractive indices is the most important task in the designing process, and it will be discussed in the Section 2.3.

For the synthesis of effective refractive indices to happen, the pitch of the SWS, denoted as p, needs to satisfy the condition [43, 44]

$$\begin{aligned} p &\leq \frac{\lambda}{(n_{sub}^2 - n_i^2 \sin^2\theta \sin^2\phi)^{1/2} + n_i \sin\theta \cos\phi} \\ &\leq \frac{\lambda}{(n_{sub}^2 - n_i^2 \sin^2\theta \sin^2\phi)^{1/2} + n_i \sin\theta \cos\phi}\Big|_{\phi=0} \\ &= \frac{\lambda}{n_{sub} + n_i \sin\theta}, \end{aligned} \tag{2.6}$$

where λ is the wavelength in the vacuum, n_{sub} is the refractive index of the material, n_i is the refractive index of the incident medium and in our case $n_i = 1$, θ is the incident angle of the light, and ϕ is the azimuth angle. This condition ensures that no diffraction happens. Since no diffraction is also referred as the "zeroth-order diffraction", SWS are sometimes called "zeroth-order diffraction gratings" [45]. With a fixed pitch, there exists a cut-off frequency ν_d above which the wavelength is too small to satisfy Eq. 2.6 and higher-order diffractions start to happen.

One distinct advantage of the SWS ARC, especially when comparing to the traditional multi-layer ARC, is that the SWS are fabricated directly on the substrate material. This characteristic that the coating and the substrate share the same material makes SWS ARC a promising ARC solution for HIM in MSM astrophysical instruments, because:

- the loss tangent of the coating is low thanks to the low loss of HIM;
- broadband can be achieved by controlling the shapes of SWS, and no more need for stacking multiple layers of different materials together;
- SWS ARCs are cryogenically robust, since the thermal expansion coefficient is uniform.

The SWS ARC also enables the realization of continuous-gradient index (CGI) profiles, many of which provide excellent broadband anti-reflection performances [46]. A CGI profile is a refractive index profile that follows continuous change along the light path, as compared to the discrete changes in the case of multi-layer profiles mentioned in the last section. In theory, a CGI profile can be approximated by a multi-layer profile as long as the number of layers is sufficiently large; in practical applications this is hardly possible due to the difficulty of finding proper materials. But with SWS, a CGI profile can be realized naturally by having the geometry of the structures smoothly change from air to substrate.

In general, the bandwidth of a CGI-profile ARC is proportional to the aspect ratio of the SWS. The aspect ratio is defined as the ratio between structure height H and pitch p. The upper edge of the ARC band ν_u is typically just the cut-off frequency ν_d above which higher-order diffractions start to happen and $\nu_u = \nu_d \propto \frac{c}{p}$; the lower edge of the band ν_l depends on the structure height H and TTM calculations showed that $\nu_l \propto \frac{c}{H}$. The dependence of ν_l on H can also be intuitively understood from a dimensional-analysis perspective: larger H should relate to longer wavelength and therefore to lower frequency. Combining these arguments, the bandwidth ratio is proportional to the aspect ratio, i.e. $\frac{\nu_u}{\nu_l} \propto \frac{H}{p}$.

The main theme for broadening the bandwidth of a CGI-profile ARC is quite clear: increase the aspect ratio of the fabricated SWS. Yet, the aspect ratio is limited by many factors in actual fabrications, such as the fabrication technique and the strength of structures. More about the fabrication using laser ablation on HIM are discussed in Chapter 3 and Chapter 4. Given the limitations in real world, it is worthwhile looking for designs that optimize the ARC performance.

Klopfenstein index profile, as shown in the panel (a) of Figure 2.7, is the optimal CGI profile for broadband ARC [47, 48]. It is the optimum in the sense that for any specified maximally allowed reflectance, Klopfenstein index profile has the minimum depth; or for any given depth of the ARC, Klopfenstein index profile produces the broadest bandwidth defined by a specified reflectance. The free parameter Γ_m controls the in-band reflection magnitude as well as the bandwidth;

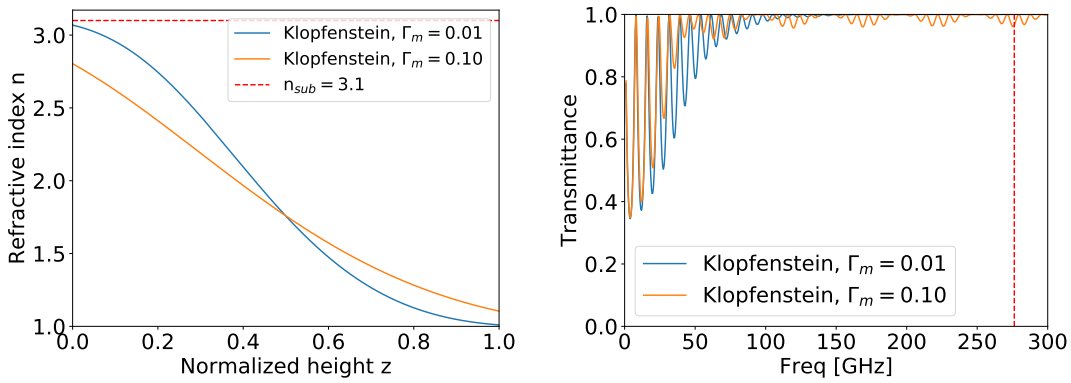

(a) (b)

Figure 2.7: (a) Klopfenstein index profiles with $n_{sub} = 3.1$, and $\Gamma_m = 0.01, 0.1$; (b) TMM predictions for the Klopfenstein index profiles from the panel (a) on both sides of the substrate. The assumed parameters are structure height $H = 1.5$ mm, thickness of the substate $t_{sub} = 5$ mm and pitch $p = 350$ μm. The vertical dashed line shows the high-frequency cut-off calculated according to Eq. 2.6.

larger Γ_m leads to larger in-band reflection but also pushes the lower edge of the band to lower frequencies. For example, in the panel (b) of Figure 2.7, the in-band reflection with $\Gamma_m = 0.1$ is higher than that with $\Gamma_m = 0.01$, but the low-frequency edge for a $T > 90\%$ band is around 40 GHz with $\Gamma_m = 0.1$ while it is around 70 GHz with $\Gamma_m = 0.01$.

Optimal index profiles need to be translated into physical shapes of SWS for them to be useful. Designing of SWS ARC is a process that deals with this task.

Two conceptually different approaches exist when it comes to designing of SWS ARC. One approach starts by finding an optimal index profile that provides satisfying anti-reflection performances predicted by TMM, and then translates that optimal index profile into a physical shape of the SWS. The other approach relies on computational resources and directly finds an optimal shape of the SWS by running rigorous electromagnetic (EM) simulations over different shapes. One of the advantages of the first approach is that it does not need heavy computational time, as long as the translation from the index profile to the physical shape of the

SWS has been accurately established. Next section discusses how to accurately map between the effective indices and physical shapes of SWS.

2.3 Effective Medium Theory

Rytov solved the effective refractive index for 1D periodic SWS, as shown in Figure 2.8, when the period is much less than the wavelength [49]. In Figure 2.8, ε_1 and ε_2 are the permittivities of two materials, p is the period, and w is the grating width of the material 1. If period is much less than the wavelength, i.e. $p/\lambda << 1$, the electromagnetic waves do not resolve the detailed structures. When the electromagnetic waves propagate in the direction perpendicular to x axis (i.e. parallel to the interfaces between material 1 and 2), Rytov showed that depending on the polarization, the effective permittivities are:

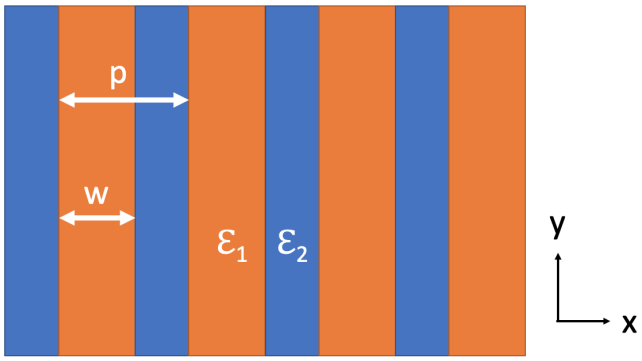

Figure 2.8: 1D periodic stratified medium.

$$\varepsilon_{\parallel}^{(0)} = f\varepsilon_1 + (1-f)\varepsilon_2, \tag{2.7}$$

$$\varepsilon_{\perp}^{(0)} = (\frac{f}{\varepsilon_1} + \frac{1-f}{\varepsilon_2})^{-1}, \tag{2.8}$$

for the zeroth-order and

$$\varepsilon_{\parallel}^{(2)} = \varepsilon_{\parallel}^{0}[\,1 + A(\frac{p}{\lambda})^2], \tag{2.9}$$

$$\varepsilon_{\perp}^{(2)} = \varepsilon_{\perp}^{0}[\,1 + B(\frac{p}{\lambda})^2]\,, \tag{2.10}$$

for the second order, where $f = \frac{w}{p}$ is the filling factor of material 1. The parameters A and B are functions of f, ε_1 and ε_2; the explicit expressions can be found in [49, 50]. The effective permittivities depends on the polarization. The TE mode is denoted as $\parallel$ and the TM mode is denoted as $\perp$.

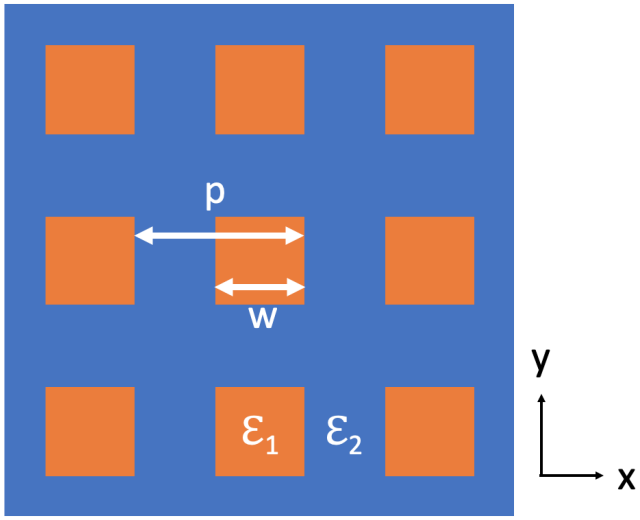

Figure 2.9: Top view of 2D SWS. Normal incidence is in the z direction.

For MSM experiments, instrument polarization due to the optics should be avoided. Since 1D SWS grating brings birefringence, using it as an ARC requires accurately alignment of the gratings on two sides to cancel out the induced polarization [44]. Moreover, the optimal index profiles described in the last section cannot be achieved for both polarizations at the same time, since they respond differently. An x-y symmetric 2D SWS grating, as illustrated in Figure 2.9, is ideal to be used as an ARC because it conserves the polarization of the normally incident waves in the z direction [46]. The work described in this thesis focuses on symmetric 2D SWS gratings.

However, no simple closed-form analytical solution of effective refractive index

n_{eff} for 2D SWS exists to our knowledge. For finding n_{eff}, this section discusses a semi-analytical approach proposed by Brauer and Bryngdahl [50] and a rigorous numerical approach using HFSS[1],

2.3.1 Quasi-static Limit ($p/\lambda << 1$)

Semi-analytical Approach

For a 2D symmetric rectangular grating shown in Figure 2.9, one may assume that the effective index is simply a weighted average based on the volume fraction

$$\overline{n} = f^2 n_1 + (1 - f^2) n_2, \tag{2.11}$$

where $f = w/p$ is the filling factor, $n_1 = \varepsilon_1^2$ and $n_2 = \varepsilon_2^2$. However, this approximation turned out to be too large [50].

Brauer and Bryngdahl were inspired by the formulation of n_{eff} in the 1D case by Rytov, as shown in Eq (2.3 - 2.6), and they extended the idea to 2D [50]. In this extension, there are essentially two steps. The first step is that they would find the effective permittivity of each row (column) of pillars using Rytov's 1D formula. After this first step, the 2D periodic pillars are now equivalent to 1D periodic stratified medium along the column (row) direction. Since now the configuration is simply 1D, the Rytov's 1D formula is applied again in the second step.

Because of the polarization dependence in Rytov's 1D formula, Brauer and Bryngdahl's extension also denpends on the polarization. As a result, the direction of the approximation in the first step, i.e. along the row or along the column, affects the calculation and therefore there are two different effective permittivities. In the quasi-static limit ($p/\lambda << 1$), the zeroth order approximations are applied and they give effective permittivities

$$\hat{\varepsilon}_{2D}^{(0)} = f\varepsilon_{\perp}^{(0)} + (1 - f)\varepsilon_2, \tag{2.12}$$

[1] A 3D electromagnetic simulation software using finite element method.

$$\check{\varepsilon}_{2D}^{(0)} = (\frac{f}{\varepsilon_{\parallel}^{(0)}} + \frac{1-f}{\varepsilon_2})^{-1}, \tag{2.13}$$

where $\varepsilon_{\perp}^{0}$ and $\varepsilon_{\parallel}^{0}$ are calculated using Eq. 2.8 and Eq. 2.7 respectively. The corresponding zeroth-order effective indices are $\hat{n}_{2D}^{(0)} = (\hat{\varepsilon}_{2D}^{(0)})^2$ and $\check{n}_{2D}^{(0)} = (\check{\varepsilon}_{2D}^{(0)})^2$

Brauer and Bryngdahl proposed that the accurate approximation of n_{eff} is not any one of the $\overline{n}$, $\hat{n}_{2D}$ and $\check{n}_{2D}$, but a weighted average of all three:

$$n_{eff} = \frac{1}{5}(\overline{n} + 2\hat{n}_{2D}^{(0)} + 2\check{n}_{2D}^{(0)}). \tag{2.14}$$

Figure 2.10 shows each one of the above indices as functions of filling factor, assuming that $n_1 = 3.4$ and $n_2 = 1.0$ (silicon pillars in vacuum).

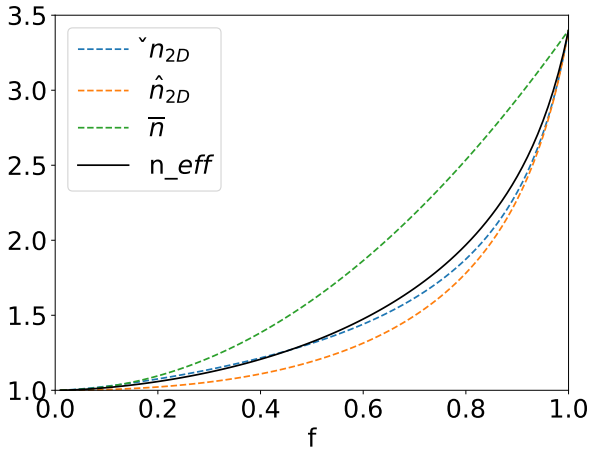

Figure 2.10: Zeroth-order effective indices vs filling factor according to Brauer and Bryngdahl. Assumptions: $n_1 = 3.4$ and $n_2 = 1.0$.

Numerical Simulation (HFSS)

To verify the validity of the effective refractive index n_{eff} calculated by Brauer and Bryngdahl's method, rigorous simulations were carried out using finite element analysis on HFSS.

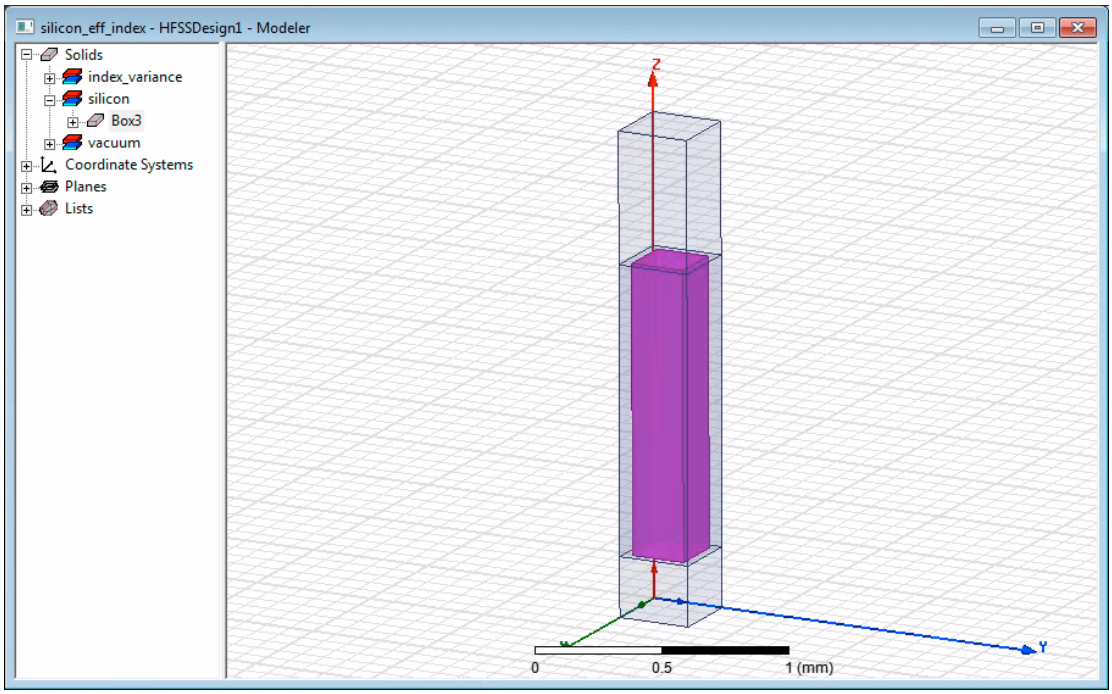

Figure 2.11: HFSS simulation setup to emulate "air-material-air" configuration. Note that the dimensions shown are just for illustration purpose.

An example of the HSFF simulation setup is shown in Figure 2.11. The purple square pillar is silicon with refractive index $n = 3.4$, and the rest of the larger transparent square pillar is vacuum with $n = 1$. Periodic boundary conditions are applied on the four lateral sides of the larger pillar to emulate periodic 2D SWS grating as shown in Figure 2.9. The upper/lower sides are set to be Floquet Ports via which the electromagnetic waves are transmitted/received. The pitch is the width of the larger pillar and the filling factor f is the ratio between the widths of two pillars.

If EMT is valid, then the middle region where the purple pillar sits in is emulating an effective medium. The transmittance and reflectance in such an "air-material-air" configuration can be modeled by TMM. By fitting the HFSS simulation results with TMM, one can obtain the effective refractive index n_{eff}.

To simulate the case of quasi-static limit and compare to the zeroth-order

approximations of n_{eff} from Brauer and Bryngdahl, the pitch was set to be 10 μm and the reflectance was calculated between 1 and 300 GHz with normal incidence. Within the entire frequency range, the ratio p/λ is smaller than 0.01, a value that reasonably represents the quasi-static limit $p/\lambda \ll 1$. The height of the purple pillar (SWS) was 0.5 mm, and the filling factor f was swept over between 0.05 and 1 with 0.05 increment by adjusting the width of the purple pillar.

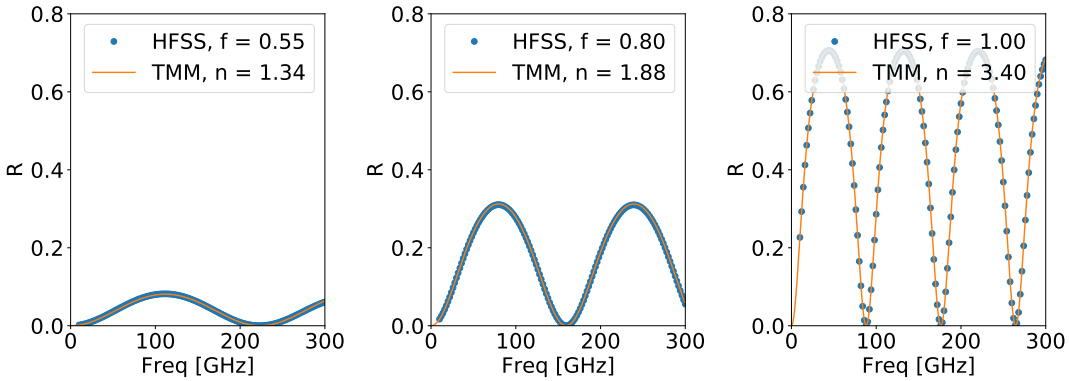

Figure 2.12: HFSS simulated reflectance in quasi-static limit with filling factor $f = 0.55, 0.70$ and 1.00 (blue dots), and TMM fitting with refractive index n (orange curve).

Figure 2.12 shows some of the simulation results ($f = 0.55, 0.70, 1.00$). Assuming the effective medium has the thickness equal to the height of the SWS, i.e. 0.5 mm in this case, the TMM calculations were used to fit for n_{eff}. The results showed that for all simulated configurations with filling factors between 0 and 1, the HFSS data agreed well with TMM fitting.

In Figure 2.13, the n_{eff} obtained from both the Brauer and Bryngdahl's method and HFSS simulations are plotted. The results from two methods agree with each other reasonably well, with the largest discrepancy of about 4.5% at $f = 0.8$. An adjustment of the weights of $\overline{n}$, $\hat{n}_{2D}$ and $\check{n}_{2D}$ in Eq. 2.14 may reduce the discrepancies when compared to HFSS fitting method; for example $n_{eff} = \frac{1}{7}(\overline{n} + 5\hat{n}_{2D} + \check{n}_{2D})$ brings down the discrepancies to lower than 2.5%.

In conclusion, in the quasi-static limit, where the pitch of the SWS is much

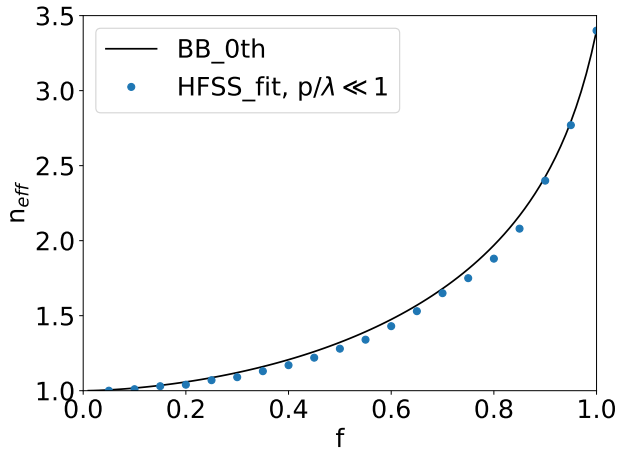

Figure 2.13: n_{eff} vs filling factor in the quasi-static limit. Black curve is obtained using Brauer and Bryngdahl's 0th-order approximation, and blue dots are obtained by fitting the HFSS simulation data. Assumptions: $n_1 = 3.4$ and $n_2 = 1.0$.

smaller than the wavelength, HFSS simulation confirmed that 2D symmetric SWS interact with normally incident light as if they are homogeneous effective medium. The effective refractive index of 2D SWS depends on the filling factor and can be calculated using Brauer and Bryngdahl's zeroth-order approximations.

2.3.2 Non-quasi-static Limit

The "non-quasi-static limit" is nominally defined as $p/\lambda > 0.05$ in this thesis.

Fabrication Limitations and Non-negligible Pitch

From a fabrication perspective, there are strong motivations to have pitch as large as possible for SWS. First of all, generally speaking a smaller pitch demands higher fabrication precision, and even if the precision is achievable it would typically lead to higher cost. Second of all, with a smaller pitch, the fabrication time could take longer because more structures have to be made on a fixed area (excluding etching technique). In the case of laser ablation, the ablation rate also degenerates with

a smaller pitch when height is fixed; this will be discussed in Chapter 4. Last but not least, larger pitch means smaller aspect ratio for a given height, and smaller aspect-ratio structures tend to be more robust to impacts.

Taking the fabrication into consideration, the pitch is typically selected just small enough so that higher-order diffractions are avoided. According to Eq. 2.6, $p/\lambda < 1/n_{sub}$, for SWS fabricated on HIM whose index is between 3 and 3.5, the high-frequency edge of the ARC band is close to where $p/\lambda \approx 0.3$. Clearly, p/λ is non-negligible and quasi-static limit condition is not valid any more. Zeroth-order approximations of n_{eff} are therefore expected to be inaccurate in the design of SWS ARC.

Figurate 2.14 illustrates what could happen if only the zeroth-order approximations of n_{eff} are applied while designing a SWS ARC. In this example, the design target is a single-layer $\lambda/4$ coating on silicon ($n_{sub} = 3.4$) that is to be achieved by SWS. Ideally, if the pitch can be infinitely small compared to all in-band wavelengths, the task is simply translating the desired index profile to SWS using zeroth-order approximations. For a single-layer $\lambda/4$ coating, $n_{coating} = \sqrt{n_{sub}}$, so in the quasi-static limit one just needs to find the filling factor in Figure 2.13 that corresponds to $n_{eff} = \sqrt{3.4}$. In the HFSS simulation, the physical shape of SWS is a pillar with filling factor obtained using Brauer and Bryngdahl's 0th-order approximation. If the pitch of the SWS was indeed small, e.g. $p = 10$ μm, one would expect that the HFSS simulation should match the TMM prediction using the index profile. However, considering the fabrication limitations the pitch was set to be 300 μm. As a result, near the central frequency 200 GHz ($\lambda = 1.5$ mm), the ratio $p/\lambda \approx 0.2$. It turned out that the result from HFSS simulation noticeably deviated from the TMM prediction when frequency is above 200 GHz where $p/\lambda > 0.2$. One consequence of such deviation was that the achieved ARC bandwidth using SWS was smaller than the designed.

Therefore, due to the realistic fabrication limitations, the behavior of SWS in the non-quasi-static limit needs to be understood and considered in the design of SWS ARC.

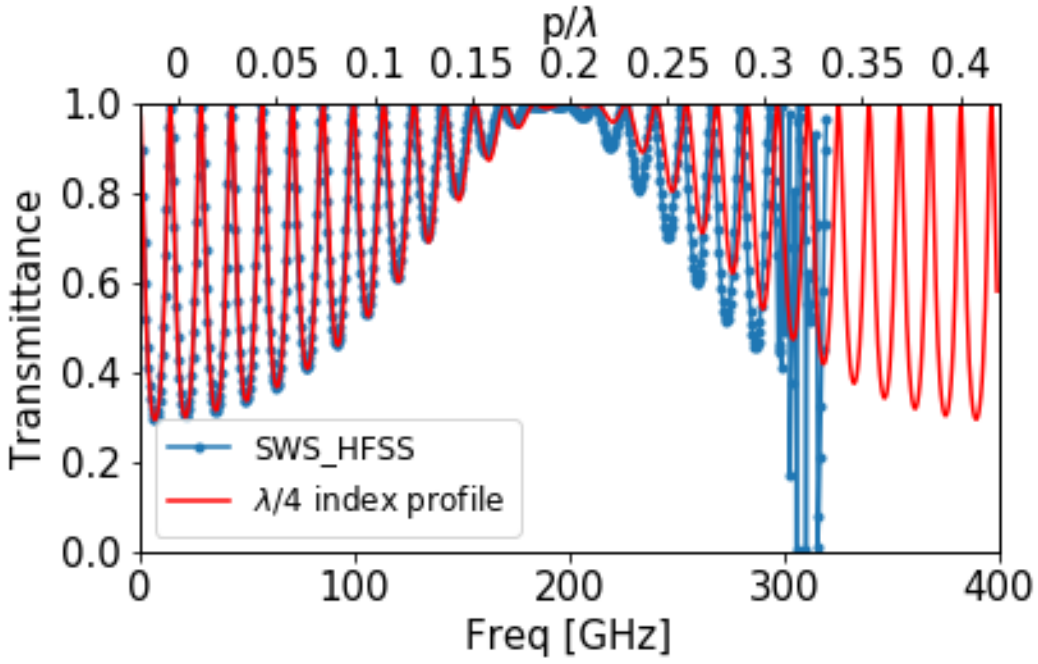

Figure 2.14: SWS $\lambda/4$ coating centered at 200 GHz on a 3 mm sbustrate with $n_{sub} = 3.4$. The red curve shows TMM prediction with the ideal $\lambda/4$ index profile, i.e. $n_{coating} = \sqrt{n_{sub}}$ and the optical length through the coating is one quarter of a wavelength at 200 GHz. The blue dots show the HFSS simulation with SWS pillars on two sides of the substrate to emulate the $n_{coating} = \sqrt{n_{sub}}$ coating medium. The SWS has a pitch of 300 um and the filling factor was found using Brauer and Bryngdahl's 0th-order approximation. Notice the higher-order diffraction starts happening beyond $p/\lambda = 0.294$.

Higher-order EMT

The original Rytov's approximations on n_{eff} for 1D SWS, as well as Brauer and Bryngdahl's extensions to 2D SWS, suggested that higher orders corrections should be added on top of the zeroth-order approximation when p/λ is not much less than one. There are other studies using numerical methods [45, 51, 52] that demonstrated increasing p/λ would increase n_{eff} of SWS.

According to Brauer and Bryngdahl, the 2nd-order n_{eff} is obtained by replacing the superscript from (0) to (2) through Eq (2.8) to (2.10). The 2nd-order terms $\varepsilon_{\parallel}^{(2)}$ and $\varepsilon_{\perp}^{(2)}$ in the new equations are calculated using Rytov's Eq. 2.9 and Eq. 2.13. Figure 2.15 shows the n_{eff} calculated using Brauer and Bryngdahl's 2nd-order approximations, at several different p/λ. It can be seen that compared to the zeroth-order approximation with $p/\lambda = 0$, the n_{eff} approximated with $p/\lambda = 0.10$ is roughly the same but the n_{eff} approximated with $p/\lambda = 0.20$ is clearly distinct.

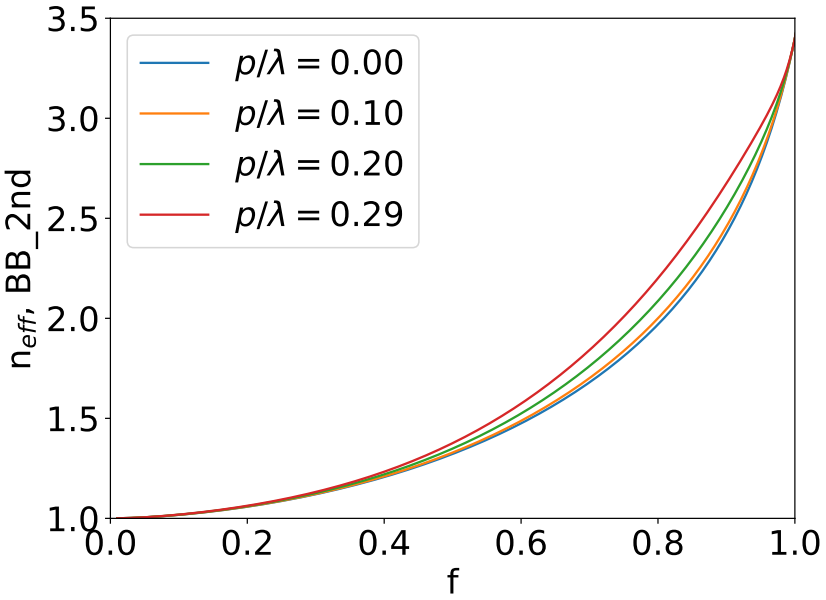

Figure 2.15: n_{eff} vs filling factor obtained from Brauer and Bryngdahl's 2nd-order approximations. Assumptions: $n_1 = 3.4$ and $n_2 = 1.0$.

Figure 2.15 shows that a fabricated array of SWS would realize different index profiles at different frequencies in the non-quasi-static limit. This explains what happened in Figurate 2.14: at low frequencies where p/λ is small, the realized n_{eff} by the SWS matches the ideal $\lambda/4$ index profile and so does the transmittance; at high frequencies where p/λ is large, the realized n_{eff} by the exactly same SWS is no longer the same and therefore does not match the desired index profile any

more.

A changing realized index profile from a fixed SWS in the non-quasi-static limit is a conundrum for a design process. An ideal index profile, such as Klopfenstin, can never be realized across the entire band unless $p/\lambda \ll 1$. In practice, the best one can do is choosing a frequency that matters the most and convert an index profile to a physical shape of SWS at the corresponding p/λ, so that the ARC performance near the chosen frequency more accurately matches what can be provided by the ideal index profile. For example, in the example of Figurate 2.14, it would be more proper to translate the $\lambda/4$ index profile to a physical SWS at the center frequency 200 GHz, i.e. at $p/\lambda = 0.2$.

Therefore, an accurate conversion between n_{eff} and a physical shape of SWS at different p/λ in the non-quasi-static limit is necessary. Similar to what I did for the quasi-static limit, I performed rigorous numerical calculations using HFSS to simulate non-quasi-static limit.

HFSS Simulations

The HFSS simulation setup was basically the same as described in the Section 2.3.1 except that the pitch was increased from 10 μm to 300 μm. The simulation was run between 1 and 300 GHz, so that the pitch-over-wavelength ratio covered between $p/\lambda = 0.01$ (at 1 GHz) and $p/\lambda = 0.30$ (at 300 GHz). The height of the purple pillar, as shown in Figure 2.11, was increased from 0.5 mm to 2 mm, in order to provide more fringe features; more fringe features helped improve the accuracy of the fitting. The filling factor f was swept over between 0 and 1, with 0.05 increment between 0 and 0.8 and with 0.01 increment between 0.8 and 1, again by only adjusting the width of the purple pillar. The reason to have smaller increment between 0.8 and 1 was because one would expect the slope of n_{eff} vs f to be steep in that region, as shown in Figure 2.15. The material of the pillar was silicon with $n_{sub} = 3.4$.

Figure 2.16 shows examples of the HFSS simulation results (in blue) with $f = 0.6, 0.7$ and 1.0. Note that $f = 1.0$ represents a homogeneous silicon layer.

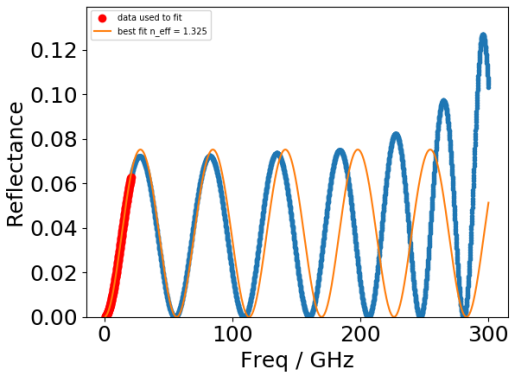

(a) $f = 0.55$, 0 - 20 GHz

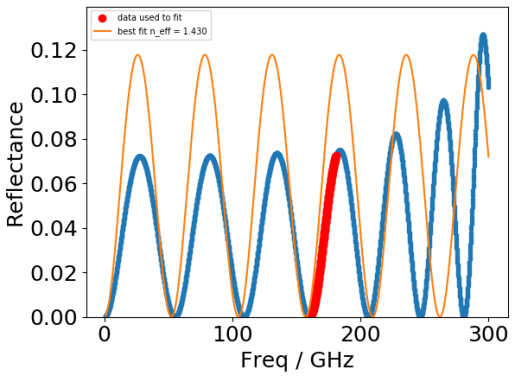

(b) $f = 0.55$, 160 - 180 GHz

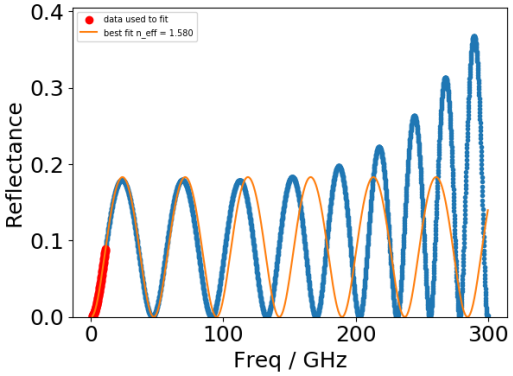

(c) $f = 0.70$, 0 - 20 GHz

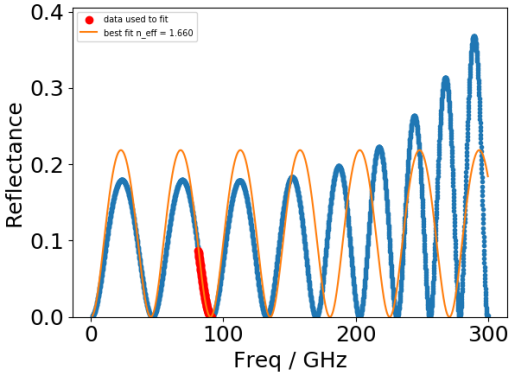

(d) $f = 0.70$, 160 - 180 GHz

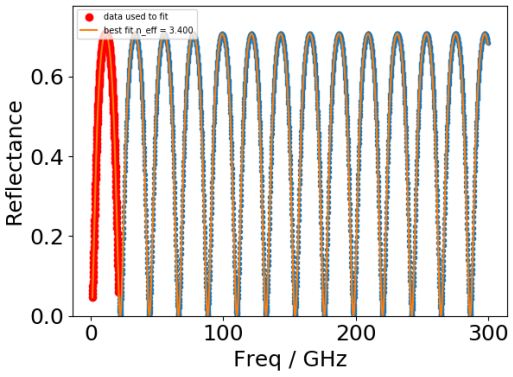

(e) $f = 1.00$, 0 - 20 GHz

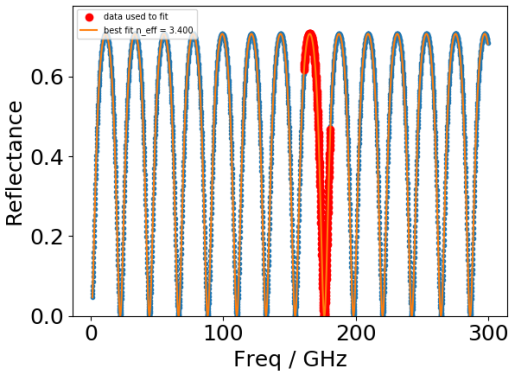

(f) $f = 1.00$, 160 - 180 GHz

Figure 2.16: Fitting to HFSS simulations with data in 20 GHz sub bands.

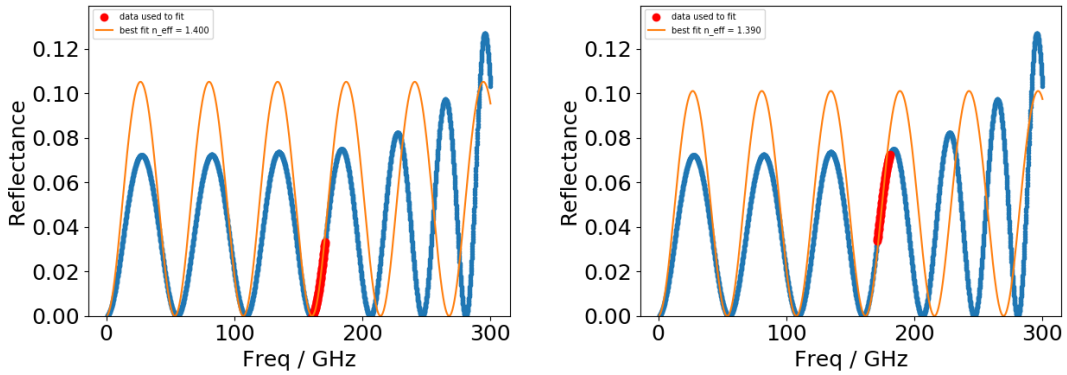

(a) $f = 0.55$, 160 - 170 GHz

(b) $f = 0.55$, 170 - 180 GHz

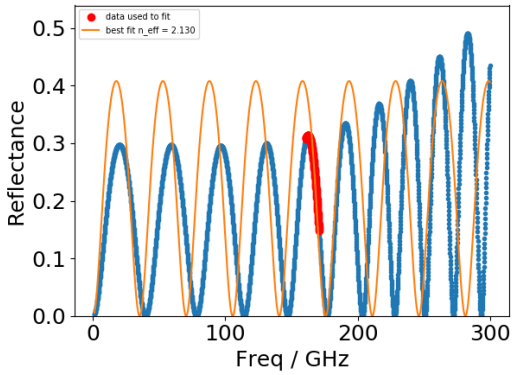

(c) $f = 0.70$, 160 - 170 GHz

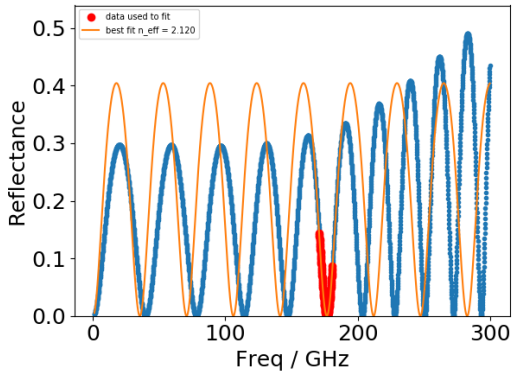

(d) $f = 0.70$, 170 - 180 GHz

Figure 2.17: Fitting to HFSS simulations with data in 10 GHz sub bands.

Very interestingly and as expected, the results show that the amplitude of maxima of reflectance increases as frequency increases in the cases of $f = 0.6$ and 0.7, but stays constant when $f = 1.0$. In addition, when $f = 0.6$ and 0.7, the densities of fringe features increase as frequency increases.

In a simple air-material-air configuration, one would expect that an increasing refractive index of the material would increase (1) reflectance and (2) density of fringes in T/R vs frequency plots. Such dependence of the amplitude and phase on the refractive index can be seen in Figure 2.2. So qualitatively, the HFSS simulations agree with what have been predicted by Brauer and Bryngdahl's method — n_{eff} increases when p/λ increases.

To verify the validity of EMT and to quantify the n_{eff}, I fit the data with TMM calculation by assuming that the thickness of the effective medium was equal to the height of the SWS. Since we expected that the n_{eff} would be a function of p/λ, fitting should be done at different frequencies. Therefore, I divided the entire 1 - 300 GHz band into 20 sub bands, each with a 20 GHz bandwidth. Since p was fixed at 300 μm, each sub band covered a segment of 0.05 in terms of p/λ. At each time, only the data in one of the sub bands was used for fitting. This is illustrated by the red dots in Figure 2.16. The orange curve in each panel is the reflectance calculated by TMM, with the effective index found only using the red data points.

When $f = 1.0$, as shown in the panel (e) and (f), the fitting results are the same, i.e. $n_{eff} = 3.40$. This is reasonable since $f = 1.0$ represents a homogeneous silicon layer, and n_{eff} should simply be equal to the refractive index of silicon $n_{sub} = 3.4$. When $f < 1.0$, as shown in the upper four panels, the fitting results using data in different sub-bands become different.

In the panel (a) and (c), where the lowest sub band 1 - 20 GHz was used for fitting, the orange curves obtained agree well with the red data points, verifying the validity of EMT when $p/\lambda < 0.02$. In fact, the orange curves also agree reasonably well with other blue data points up to about 100 GHz. Clear differences in phase show up above 100 GHz, and obvious differences in amplitude appear

above 200 GHz. The fitting results show that $n_{eff} = 1.395$ with $f = 0.6$ and $n_{eff} = 1.580$ with $f = 0.7$. The agreement between the orange curves and the HFSS data below 100 GHz indicates that in this region SWS do behave like an effective medium and the n_{eff} does not strongly depend on the p/λ ratio. The weak dependence on p/λ when $p/\lambda < 0.1$ agrees with the prediction of n_{eff} using Brauer and Bryngdahl's method, as shown in Figure 2.15.

In the panel (b) and (d), where the sub band 160 - 180 GHz was used for fitting, the orange curves obtained do not agree with the red data points. If one pays attention to the phase and amplitude, it can be seen that although the orange curves are roughly aligned with red data points in phase, they have large discrepancies in amplitude. The disagreement between the TMM fitting and HFSS data indicates that either the fitting is not proper or EMT is invalid in the region of $0.16 < p/\lambda/ < 0.18$.

Having the suspicion of the fitting procedure, I reduced the bandwidth of sub bands from 20 GHz to 10 GHz and ran the fitting again. Some results are shown in Figure 2.17 with sub bands 160 - 170 GHz and 170 - 180 GHz. The rationale for reducing the bandwidth of sub bands was because we expected a changing n_{eff} with respect to the frequency, and fitting with a constant effective index over a large frequency range would not be proper. As a matter of fact, it was for this reason that I chose 20 GHz bandwidth instead of wider in the first place. If it was indeed the cause for discrepancies in the fitting, with 10 GHz bandwidth that corresponds to 0.01 increment in p/λ, we should at least see some degrees of improvement. Yet the orange curves still do no agree with the red data points, and it does not seem to bring any obvious improvements compared to the panel (b), (d) in Figure 2.16.

The discrepancies between the TMM fitting and HFSS simulations described above were observed across all filling factors when $p/\lambda > 0.05$, and the discrepancies became larger at larger p/λ.

Triggered by the fact that near the red data points the orange curves tended to show larger amplitude while maintaining a similar phase compared to the HFSS

data, I looked into the amplitude and phase separately and quantitatively.

Effective Indices: n_{phase} **&** n_{amp}

With homogeneous materials, the refractive index controls both the phase and amplitude of T/R vs frequency. For example, in a simple air-material-air configuration given the thickness of the material t_{sub}, changing the refractive index of the material n_{sub} will change the fringe pattern of T/R vs frequency in a determinant manner, as shown in Figure 2.2. The amplitude of maximum reflectance R_{max} can be calculated using Eq. 2.5. The locations of R_{max} and $R = 0$ in the frequency space can be predicted based on [53]:

$$\frac{2\pi nt}{c/\nu_{R=0}} = m\pi \quad (m = 0, 1, 2, ...) \tag{2.15}$$

$$\frac{2\pi nt}{c/\nu_{R_{max}}} = (m' + \frac{1}{2})\pi \quad (m' = 0, 1, 2, ...) \tag{2.16}$$

Therefore, it is possible to estimate the n_{eff} from HFSS simulation purely based on the amplitude of local R_{max} or based on the locations of the local minima and maxima. I named such effective refractive indices as n_{amp} and n_{phase} respectively. For a normal homogeneous material, $n_{amp} = n_{phase} = n_{sub}$.

Figure 2.18 shows some examples of such analysis. In each panel, the local minima $R = 0$ and local maxima R_{max} are found in the upper sub panel, as shown in green and red dots respectively. Then the corresponding effective n_{amp} are calculated according to Eq. 2.5, while n_{sub} are calculated using Eq. 2.15 and Eq. 2.16; the results are shown in the lower sub panels. The number of the n_{amp} obtained is equal to the number of the local maxima, while the number of n_{phase} obtained is equal to the number of the local maxima plus the number of the local minima. Again, the HFSS data with $f = 1.00$ was used as a sanity check; the results shown in the panel (e) and (f) are consistent with $n_{amp} = n_{phase} = n_{sub} = 3.4$ within ± 0.01.

An interpolation was done on the discrete indices n_{amp} or n_{phase} over the entire

frequency band, to better illustrate the overall trend, as shown by the red curve in each lower sub panel. The trend line was constructed assuming that the higher-order correction due to p/λ obeys a power law, i.e.:

$$n_{eff} = n^{(0)} + a \times (\frac{p}{\lambda})^b, \tag{2.17}$$

where $n^{(0)}$ represents the n_{eff} in the quasi-static limit and is allowed to freely change, and a, b are two other free parameters. It turned out that at a fixed f, the $n^{(0)}$ from n_{amp} and n_{phase} are similar to each other with discrepancies less than 4%, but parameters a and b were quite different reflecting the different growth trends of n_{amp} and n_{phase} with respect to p/λ.

With the interpolation of n_{eff} as a function of p/λ, I calculated the TMM predicted reflectance at all frequencies using the n_{eff} at each frequency, as shown by the red curves in the upper sub panels. On one hand, the TMM calculations using n_{amp} precisely capture the change of the amplitude of the HFSS data, but show clear mis-match in phase, as shown in panel (a), (c). On the other hand, the TMM calculations using n_{phase} agree very well with the HFSS data in terms of the phase, but appear to have larger amplitude, as shown in panel (b), (d).

Another strong evidence of such interesting behavior of SWS in the non-quasi-static limit was that I succeeded to predict the HFSS data for the first time using TMM while using both n_{phase} and n_{amp} as the inputs for the prediction. In the TMM formulation, originally the same refractive index appears both inside and outside the trigonometric functions [34]. Inside the trigonometric functions, the index controls the phase of the result; outside the trigonometric functions, the index affects the amplitude. To separately control the phase and the amplitude, I used the n_{phase} obtained previously as the input inside the trigonometric functions and used n_{amp} as the input outside the trigonometric functions, and I obtained Figure 2.19. The red curve, which was the calculation result, agreed with the HFSS data very well. This result straightforwardly illustrated the behavior of SWS in the non-quasi-static limit.

In conclusion, SWS do not behave exactly like homogeneous material in the

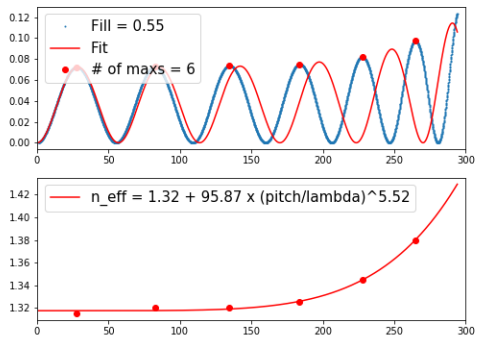

(a) $f = 0.55$, n_{amp}

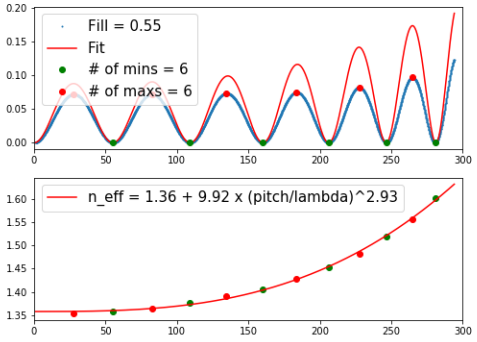

(b) $f = 0.55$, n_{phase}

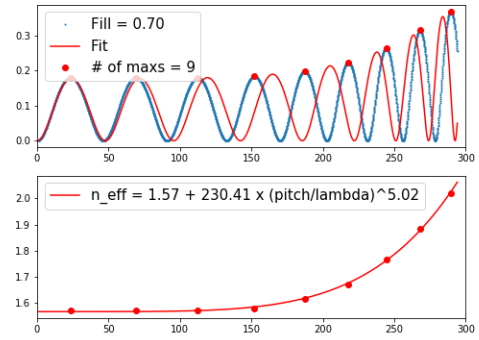

(c) $f = 0.70$, n_{amp}

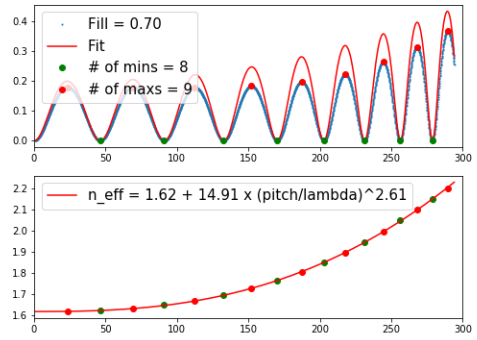

(d) $f = 0.70$, n_{phase}

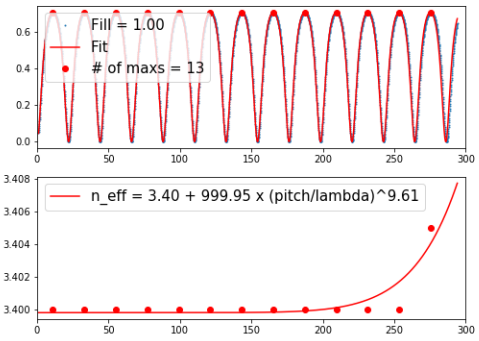

(e) $f = 1.00$, n_{amp}

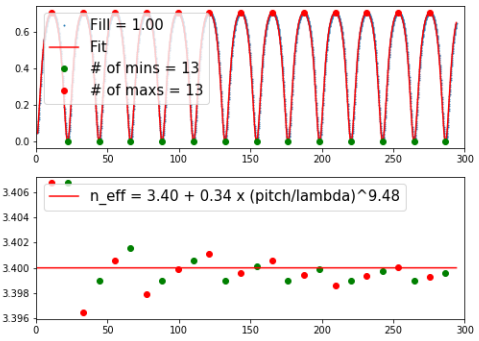

(f) $f = 1.00$, n_{phase}

Figure 2.18: Fitting to HFSS simulations using the amplitude of local R_{max} and locations of R_{max} and R_0. In each panel, the upper sub panel is R vs frequency in GHz, and the lower sub panel is n_{eff} vs frequency in GHz. The maxima of R are shown in red dots while the minima are shown in green dots; the corresponding effective indices are illustrated by the dots in the same color in the lower panel. The red curves show the fitting results.

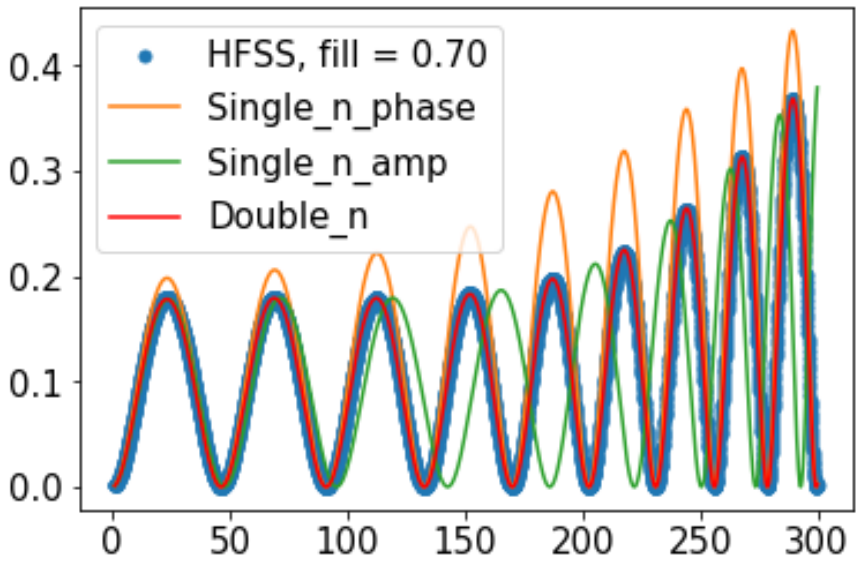

Figure 2.19: Fitting to R vs frequency in GHz from HFSS simulation ($f = 0.7$) with the original TMM (orange and green) and the modified TMM (red).

non-quasi-static limit, and a model with two co-existing effective indices n_{phase} and n_{amp} match the HFSS simulations.

2.3.3 Comparison of n_{eff} from Different Approximations

So far we have discussed four different methods for approximating the effective index n_{eff} of SWS in the non-quasi-static limit: (1) semi-analytical 2nd-order approximations from Brauer and Bryngdahl; (2) direct fitting to the HFSS simulation data in different sub bands using TMM; (3) fitting only to the phase of the HFSS simulation data; (4) fitting only to the amplitude of the HFSS simulation data. Now let us compare them quantitatively.

Figure 2.20 shows the n_{eff} vs filling factor f obtained from these four different methods at a few p/λ ratios. The blue curves are from method (1) and therefore are continuous in f. The other three approximations are all based on the HFSS simulations, which were done at a finite number of filling factors, and therefore are discrete in f. Note that there are some outliers in the case of n_{fit}, which

were obtained from the direct fitting using TMM. The outliers were caused by failures of finding the global minimum in the fitting process, because of the strange behaviors of SWS at large p/λ.

Ignoring the outliers, the red points ("n_{fit}") are basically overlapping with the gree points (n_{phase}), i.e. $n_{fit} \approx n_{phase}$. This observation agrees with the observations made before that the direct fitting tend to match the phase of the HFSS data rather than the amplitude, as shown in Figure 2.16. This is because when fitting a fringe pattern using least-square method, the sum of the squares of residuals is simply more sensitive on a mis-match in phase rather than on the difference in peak amplitude.

The differences between n_{amp} and n_{phase} again demonstrate the complex behaviors of SWS in the non-quasi-static limit. Especially at large p/λ and near $f = 0.6$, two effective indices can be different by more than 10%. A direct consequence is that **in the non-quasi-static limit there is simply no one-to-one relationship between a physical SWS and an effective index profile even at a fixed p/λ**.

When comparing the blue curves with what I obtained using numerical simulations with HFSS in Figure 2.20, it seems that by large Brauer and Bryngdahl's approximations are closer to the n_{phase} than to the n_{amp} in the most cases except at very large p/λ and large f.

2.3.4 Comparison of T/R Predicttions using n_{eff}

Although the comparisons of n_{eff} obtained from various methods are insightful and interesting, how accurately these effective indices can predict the T/R vs frequency using TMM is most important from a design perspective. Therefore in this section I will translate physical SWS into effective indices using different mappings and compare their TMM results against HFSS simulations.

When using Brauer and Bryngdahl's 2nd-order approximations, the translation from a physical shape of SWS to effective indices is straightforward. With a given

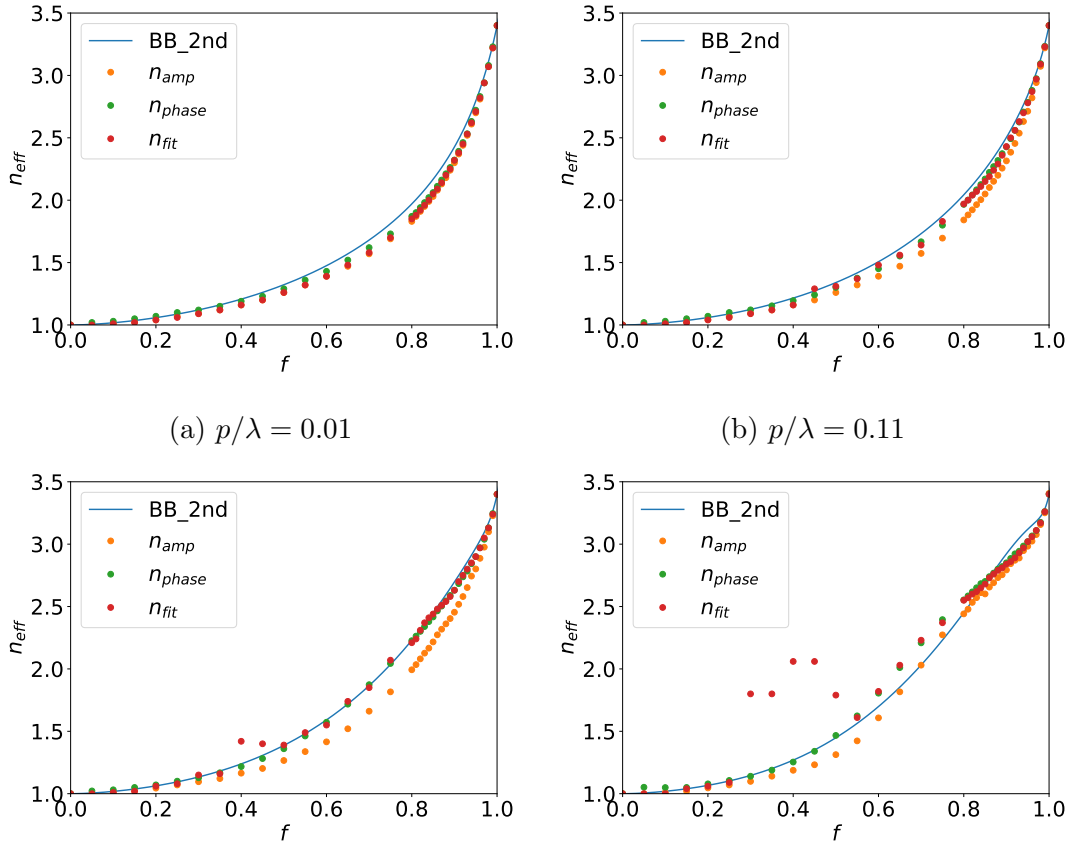

(a) $p/\lambda = 0.01$

(b) $p/\lambda = 0.11$

(c) $p/\lambda = 0.21$

(d) $p/\lambda = 0.29$

Figure 2.20: n_{eff} vs filling factor from different approximation methods at different p/λ ratio. The blue are from Brauer and Bryngdahl's 2nd-order approximations; the red are from the direct TMM fitting to the HFSS simulations in 20 GHz sub bands; the orange and green are fitting to HFSS data using amplitude and phase information respectively.

pitch, at any frequency we can calculate the p/λ ratio. Then we plug the filling factors of the shape and p/λ ratio into the 2nd-order version of Eq. 2.14 to get the corresponding n_{eff}.

When using n_{eff} obtained from HFSS simulations at discrete filling factors, we need to interpolate the discrete data first, so that we can do the translation for any filling factor between 0 and 1. Figure 2.21 shows an example of such an interpolation. The blue dots are calculated using Eq. 2.17 with already obtained parameters at each filling factor for n_{phase}, assuming $p/\lambda = 0.20$. The large green dot shows the interpolated n_{eff} with $f = 0.761$ at $p/\lambda = 0.20$. This process needs to be repeated with a different p/λ at each single frequency.

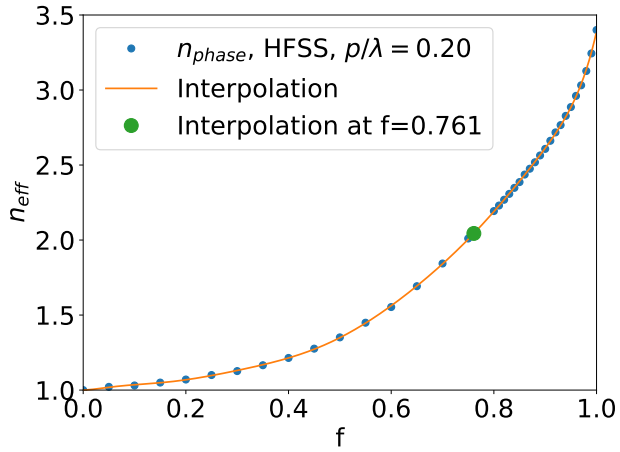

Figure 2.21: Example of the interpolation of discrete n_{phase} (or n_{amp}) to an arbitrary filling factor at a given p/λ.

The HFSS simulation result shown in Figure 2.14 is compared to TMM predictions using different n_{eff}; the comparison results are shown in Figure 2.22. The TMM calculations are carried on a frequency-by-frequency basis. The upper panel shows the T vs frequency, and the lower panel shows the deviations from the HFSS simulation. It can be seen that at the lowest frequencies below 50 GHz, or $p/\lambda < 0.05$, all of the TMM calculations match HFSS data very well with less than 0.1 deviations in transmittance only because of a small mis-match in phase.

This demonstrates again that in the quasi-static limit, the SWS behave like homogeneous materials, and Brauer and Bryngdahl's method is quite accurate. At higher frequencies, in the non-quasi-static limit, the deviations between TMM calculations and HFSS data become more obvious.

Surprisingly, the Brauer and Bryngdahl's method gives the closest agreement to the HFSS data. Especially around 200 GHz, where the ARC band is designed at, the deviations between the orange curve and blue data are smaller than a few percent. In fact, if we ignore the small phase shifts, the Brauer and Bryngdahl's method gives excellent prediction on the transmittance at all frequencies.

The results using n_{phase} or n_{amp} do not provide better agreement in phase or amplitude respectively, suggesting that the mapping we obtained based on the HFSS simulations of single floating pillars may be not correct for different configurations. In other words, the medium around the SWS possibly affects the effective behavior as well. After spending about a year doing HFSS simulations and coming up with all kinds of ideas just trying to find the "correct" mapping between n_{eff} and SWS physical shape, I finally concluded that there is no rigorous mapping in the non-quasi-static limit. From a practical design perspective, the formula proposed by Brauer and Bryngdahl is good enough for designing SWS ARC.

2.4 A Practical Design Guide

We have discussed several optimal index profiles in Section 2.2 and the relationship between physical shapes of SWS and effective indices in Section 2.3. In this section, I combine all these pieces together and provide a guide for how to design a SWS ARC. In a design process, there are essentially three steps:

- Step 1: **Determine the pitch** of SWS based on the highest band frequency using Eq. 2.6.

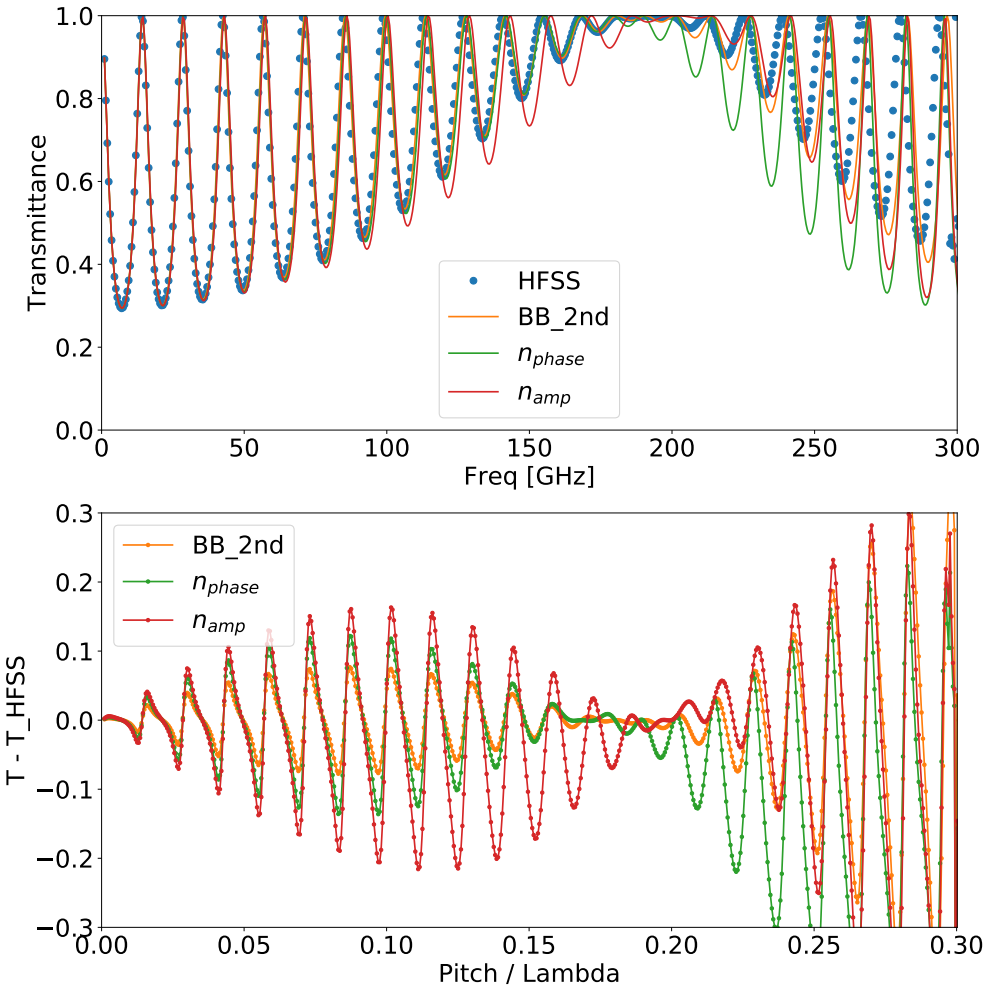

Figure 2.22: Comparisons between TMM predictions using different n_{eff} and the HFSS simulation shown in Figure 2.14. The SWS ARC are square pillars with $f = 0.761$ and pitch 300 mum.

- Step 2: Based on the specific requirements (e.g. ARC bandwidth, average transmittance), **determine the proper ARC index profile** by predicting the T/R vs frequency using TMM.

- Step 3: **Pick a frequency** near which the accuracy of the prediction is the most important, and **calculate the n_{eff} vs. filling factor** at the corresponding p/λ using Brauer and Bryngdahl's formula [50].

- Step 4: **Translate the index profile from Step 2 into a physical shape of SWS, using the n_{eff} vs. filling factor obtained in Step 3.**

Some design examples on alumina filters for different experiments are given below to help explain these steps.

2.4.1 Broadband ARC for Tau Surveyor

Tau Surveyor is a proposed balloon-borne experiment, which will be briefly discussed in Chapter 6. Tau Surveyor is designed to have a sapphire-based AHWP and an alumina filter, both of which will use laser ablated SWS as broadband ARC in a frequency band between 120 GHz and 420 GHz. The minimum in-band transmittance is required to be larger than 90%, and the average transmittance assuming loss tangent of 0 over the entire frequency band is required to be larger than 98%.

Assuming normal incidence and $n_{sub} = 3.1$, the largest pitch allowed is 230 μm according to Eq. 2.6 with the highest frequency at 420 GHz . Considering a 10 GHz tolerance above 420 GHz, I determined the designed pitch to be 225 μm.

For such a broadband application, I decided to use Klopfenstein index profile. Relative to the central frequency 270 GHz, the fractional bandwidth of the entire band is 111%; if using a discrete multi-layer index profile, at least four layers would be needed according to Figure 2.5. Fabricating a 4-layer SWS would be quite a challenge on its own. But fabricating a continuous shape like Klopfenstein is much more straightforward with laser ablation.

Once the type of index profile has been determined to be Klopfenstein, the next task is to find the best combination of the Klopfenstein parameter Γ_m and the height of SWS h_{ARC}. The goal is to minimize the h_{ARC} as much as possible, while having transmittance satisfying the requirements. To do this, I ran TMM calculations with different values of Γ_m and h_{ARC}. I found that $\Gamma_m = 0.10$ and $h_{ARC} = 600$ μm was a good solution, and the predicted transmittance performance is shown in the panel (a) of Figure 2.23. The predicted average transmittance over the entire band is 98.3%.

The translation from index profile to the physical SWS was done at $p/\lambda = 0.09$, which corresponds to 120 GHz given the pitch of 225 μm. The reason to choose 120 GHz was because the determinant factor of the ARC bandwidth for a continuous structure is where the transmittance drops below certain level at low frequencies; this can be seen from the panel (a) of Figure 2.23. At high frequencies, the transmittance will stay high even if the n_{eff} do not match exactly the original index profile. The panel (b) of Figure 2.23 shows the cross section of the resulting shape of the SWS after translation.

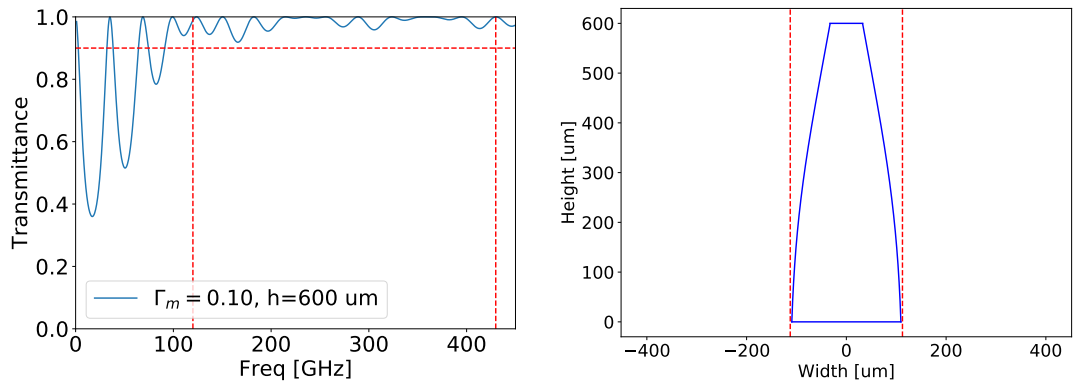

(a) (b)

Figure 2.23: Klopfenstein design of SWS ARC for TauS alumina filter. The thickness of the substrate was assumed to be 1 mm.

2.4.2 Broadband ARC for 90/150 GHz Band of Simons Observatory

Simons Observatory (SO) has three frequency band pairs, one of which is a mid-frequency (MF) that observes at 90/150 GHz [9]. The MF pair requires broadband optics roughly between 75 and 175 GHz. I was tasked to provide a SWS ARC design for the alumina filter in the MF optical system. We set a requirement on the average transmittance over the entire band to be larger than 99% assuming loss tangent of 0, and a requirement on the minimum in-band transmittance to be larger than 90%.

Assuming normal incidence and $n_{sub} = 3.1$, I calculated that the pitch had to be smaller than 552 μm based on the highest frequency 175 GHz using Eq. 2.6. Eventually I chose a $p = 500$ μm, which pushed the cut-off frequency to about 190 GHz, to provide more tolerance at the highest frequencies.

The fractional bandwidth of SO's MF is 80% relative to the central frequency 125 GHz, and I chose to use the Klopfenstein index profile. Compared to the SWS ARC designed for Tau Surveyor, because of a more stringent requirement on the average transmittance (99% v.s. 98%), I chose a smaller $\Gamma_m = 0.05$ for SO's MF band. By trying different structure height h_{ARC}, I ran TMM calculations and found that the requirements were satisfied when $h_{ARC} \geq 1.5$ mm. Figure 2.24 shows the calculation results assuming $h_{SWS} = 1.5$ mm and 1.8 mm respectively, assuming lossless material or loss tangent of 4×10^{-4}. It can be seen that a taller structure essentially pushes the T v.s. Freq curve to lower frequencies, generally speaking resulting in higher in-band transmittance. I chose the $h_{ARC} \geq 1.5$ mm as the nominal design.

The translation from the index profile to the physical shape was conducted at the central frequency 125 GHz, corresponding to a $p/\lambda = 0.21$ given the pitch of 500 μm. Unlike what I did for Tau Surveyor, in which case I chose the lowest in-band frequency to do the translation, I used the central frequency for SO's SWS because of the tighter requirement on the in-band transmittance; the design's

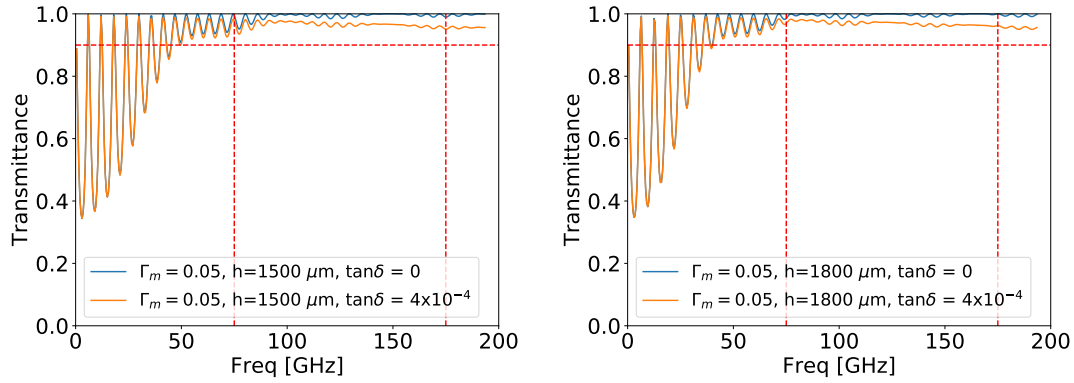

(a) (b)

Figure 2.24: TMM calculations using the Klopfenstein index profile with $\Gamma_m = 0.05$ and (a) $h_{SWS} = 1.5$ mm or (b) $h_{SWS} = 1.8$ mm. The total thickness of the alumina filter was assumed to be 10 mm before fabrication of SWS on two sides.

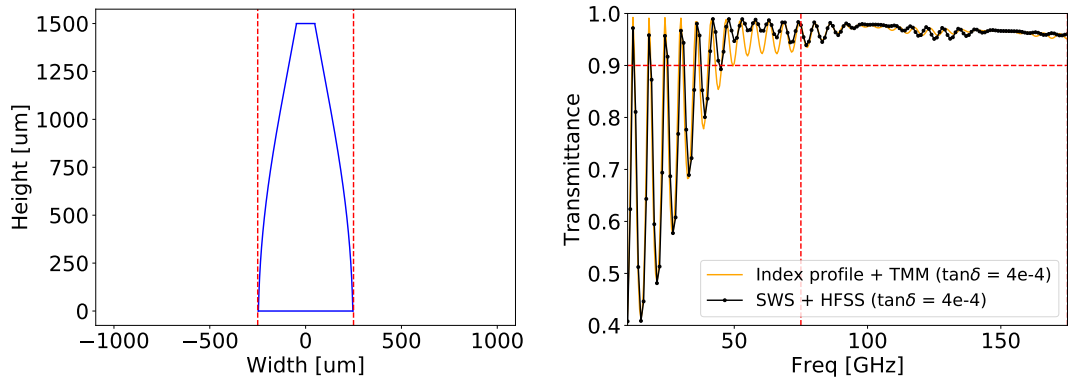

(a) (b)

Figure 2.25: (a) Designed SWS shape ($h_{SWS} = 1.5$ mm) that was translated from the index profile using Brauer and Bryngdahl's formula at 125 GHz given the pitch of 500 μm. (b) Comparison between the theoretical prediction and HFSS simulation using the designed shape.

accuracy was mostly demanded in-band. The physical shape corresponding to a $h_{SWS} = 1.5$ mm is shown in the panel (a) of Figure 2.25. I simulated this structure in HFSS with non-zero loss tangent, and the result is shown in the panel (b). From the comparison, we can see that the translation was a success because of the good agreement at the in-band frequencies, as planned. In fact, calculations showed that the average transmittance from the theory and HFSS agreed within $\pm 0.1\%$ in both 90 GHz sub-band and 150 GHz sub-band, as shown in the Table 2.2.

	90 GHz	150 GHz
$\tan\delta = 0$, TMM	99.0%	99.7%
$\tan\delta = 4 \times 10^{-4}$, TMM	97.0%	96.3%
$\tan\delta = 4 \times 10^{-4}$, HFSS	97.0%	96.4%

Table 2.2: The average transmittance calculated in the 90 (75 - 105 GHz) and 150 (127.5 - 172.5 GHz) sub-bands. The total thickness of the alumina filter was assumed to be 10 mm before fabrication of SWS on two sides.

2.4.3 Narrowband ARC for MUSTANG-2

MUSTANG-2 is a camera instrument currently observing on the Green Bank Telescope [54]. At the time of writing this thesis, we are collaborating with MUSTANG-2 team to provide a 30-cm alumina filter with SWS ARC in a band between 75 GHz and 105 GHz. This alumina filter will be the very first demonstration of the laser ablated SWS ARC on a real MSM experiment. I was tasked to provide a design for the ARC that can provide $\geq 99\%$ average transmittance when loss tangent is zero.

Considering a largest incident angle $\theta = 14.5^\circ$ and $n_{sub} = 3.1$, and also taking a 10 GHz tolerance above 105 GHz into consideration, the pitch was determined to be 770 μm.

For this narrow-band application, it turned out that a 2-layer "Max-flat" index profile was a better option than Klopfenstein. When I first tried to find a Klopfenstein design, I found out that the height of the SWS had to be around

1500 μm or higher, in order to satisfy the requirement on the average transmittance. But a design based on 2-layer "max-flat" index profile only had a total height of 976 μm.

With $n_{sub} = 3.1$, a standard two-layer "max flat" has coating indices $n_{ARC} = [1.33, 2.35]$. If converting these two indices into filling factors at the central frequency 90 GHz, the obtained SWS structure is the dashed stepped structure shown in the panel (a) of Figure 2.26. However, such structure with flank angle of 90 degrees cannot be fabricated with laser ablation, because the largest flank angle we have ever achieved with laser ablation was about 85 degrees. So I replaced the index of each layer with a continuous index profile around the original value and then converted the overall index profile into a physical shape at the central frequency; the shape is shown by the solid curves in the panel (a). TheTMMprediction shows that the average transmittance is 99.3%.

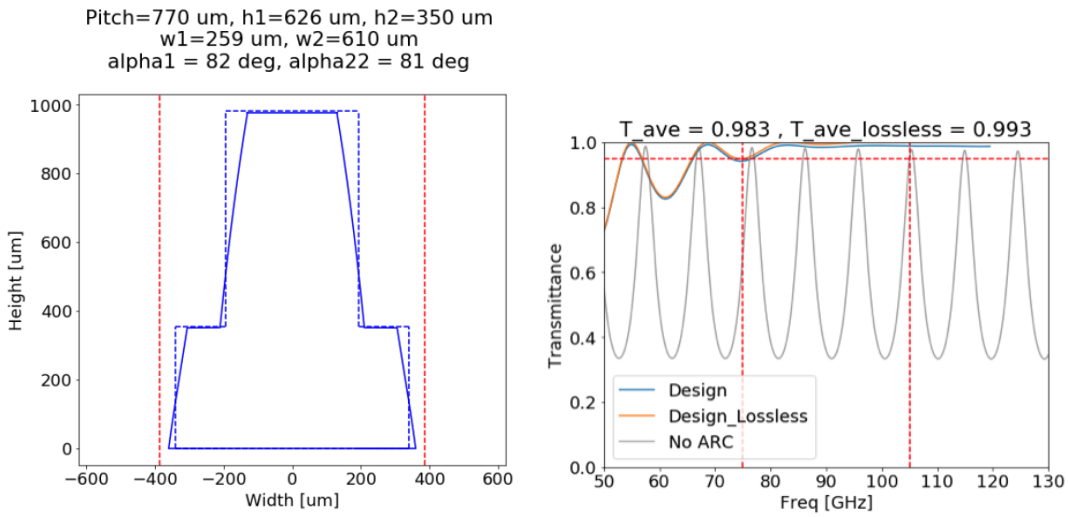

(a) (b)

Figure 2.26: MUSTANG2 ARC.

Chapter 3

SWS ARC: Laser Ablation

Alumina and sapphire have hardness 9 on the Mohs scale, making mechanical machining of SWS on them quite challenging [55, 56]. Alumina and sapphire are also chemically inert and therefore chemical etching is not efficient [57, 58].

Over the last few years, our collaboration team led by several physicists and laser experts from the US, Japan and Germany has demonstrated that laser ablation, particularly with ultrashort pulsed lasers, is a promising method to fabricate SWS ARC on alumina, sapphire, as well as silicon for MSM applications [44, 59–65].

This chapter briefly reviews the basics of ablation with ultrashort pulsed lasers, and introduces the laser ablated SWS ARC. The highlights in fabrication, measurement and optimization are summarized in this chapter and hopefully can give readers a short but comprehensive description of the development of this technology. Part of the materials were reproduced from our publications in Optics & Laser Technology [65], Applied Optics [59], Journal of Laser Micro Nanoengineering [60] and Journal of Applied Physics [64].

3.1 Ultrashort Pulsed Laser Ablation

Ultrashort pulsed laser is a laser that generates pulses of light whose duration is generally at the order of femtoseconds to a few picoseconds. With short pulse duration, the resultant high instantaneous power and high intensity of EM waves can induce non-linear absorption of photons by materials via multi-photon ionization (MPI) [66]. With MPI, exciting the materials with a band gap that exceeds the photon energy becomes possible. For example, sapphire has a wide band gap around 8.8 eV [67] and is transparent to light at 1030 nm (1.2 eV), but with a picosecond laser ($t_{pulse} = 7$ ps) at 1030 nm we can ablate sapphire. This excitation mechanism opens up a channel to transfer energy from laser pulses to materials, making ultrashort pulsed laser an effective tool for processing many different materials including alumina, sapphire and silicon.

Ultrashort pulsed laser also has advantage in fabrication precision, compared to continuous-wave laser or pulsed laser with long pulse duration. Because of the extreme short pulse duration, the heat diffusion is negligible and the interaction between ultrashort laser pulses and materials is mostly confined in a small finite volume that depends on the laser spot size. A typical spot size that we use during our development is in the order of several tens of μm.

Fluence and Ablation Threshold

"Fluence" is a term widely used in the laser community that quantifies the pulse energy density per unit area. For a Gaussian laser beam propagating along a coordinate z, the fluence as a function of beam radius and z is written as

$$\phi(r, z) = \phi_0 \left(\frac{w_0}{w(z)} \right)^2 e^{-2r^2/w^2(z)} \tag{3.1}$$

where ϕ_0 is the peak fluence, w_0 is the beam waist radius at the focal position, and $w(z)$ is the radius at which the fluence drops to $1/e^2$ of the central fluence in

the same z plane. If we define $z = 0$ at the focal position, then

$$w(z) = w_0\sqrt{1 + (z/z_R)^2}, \tag{3.2}$$

where z_R is the Rayleigh length, which will be discussed in the next subsection.

Typically without specification otherwise, a laser spot is defined as the $1/e^2$ spot at the focal position, and the laser spot size is equal to $2w_0$.

By definition, integrating the fluence over the entire area of a z-plane at any z should give a result that is equal to pulse energy E_p. In cylindrical coordinates (r, θ, z),

$$\int_0^{+\inf} \phi(r, z) r dr \int_0^{2\pi} d\theta = E_p. \tag{3.3}$$

Plugging Eq. 3.1 into Eq. 3.3, one can show that the peak fluence is

$$\phi_0 = \frac{2E_p}{\pi w_0^2}. \tag{3.4}$$

Another commonly used quantity is "average fluence", denoted here as Φ_0 to distinguish it from the peak fluence, and it is defined as the pulse energy divided by the area of the laser spot, i.e.

$$\Phi_0 = \frac{E_p}{\pi w_0^2}. \tag{3.5}$$

It can be seen that for a Gaussian laser beam, $\phi_0 = 2\Phi_0$. For example, with a typical spot size of 30 μm, a 100 μJ pulse provides an average fluence 14 J/cm^2 and a peak fluence 28 J/cm^2.

Fluence threshold of ablation, denoted as ϕ_{th}, is the minimum fluence that ablation can take place. When fluence is below ϕ_{th}, the intensity of the laser pulses is not strong enough to excite materials. In terms of the peak fluence, the following condition should be satisfied when ablation happens,

$$\phi_0 \geq \phi_{th}; \tag{3.6}$$

or equivalently in terms of the average fluence,

$$\Phi_0 \geq \frac{1}{2}\phi_{th} \equiv \Phi_{th}, \tag{3.7}$$

where Φ_{th} is the "average fluence threshold".

It is strongly recommended by the author that one should pay attention to the exact definition of "ablation threshold" in any publication in the literature of laser ablation. Throughout this thesis, I only use the fluence threshold ϕ_{th} in any relevant discussions to avoid confusion.

Fluence threshold depends on the ablated material and laser parameters, such as wavelength, pulse duration, and pulse repetition rate [68–71]. To measure the fluence threshold, a simple method proposed by Liu [72] has been widely used. According to Eq. 3.1, if one drills a hole on the surface of a material using laser ablation, the local fluence at the rim of the hole should be equal to the threshold, i.e.

$$\phi_{th} = \phi_0 \left(\frac{w_0}{w(z)}\right)^2 e^{-2r_{rim}^2/w^2(z)} \tag{3.8}$$

Note that the beam radius on the surface is $w(z)$; $w(z) = w_0$ if beam is focused on the material surface. One can solve for the radius of the rim as

$$r_{rim}^2 = \frac{w_0^2}{2} \ln \frac{\phi_0 \left(\frac{w_0}{w(z)}\right)^2}{\phi_{th}}. \tag{3.9}$$

If the pulse energy is known, then we can combine Eq. 3.4 and obtain

$$r_{rim}^2 = \frac{w^2(z)}{2} \ln \frac{\frac{2E_p}{\pi w^2(z)}}{\phi_{th}}. \tag{3.10}$$

Suppose that the laser beam profile $w(z)$ has been measured, then the fluence threshold ϕ_{th} can be solved by measuring the r_{rim}. If multiple pulse energy have been used for drilling, one can even infer both $w(z)$ at the material surface and ϕ_{th} by simply fitting r_{rim} v.s. E_p without the need to measure the beam profile.

Our collaborators at Lazer Zentrum Hannover (LZH) in Germany used the method described above, and with an independently characterized beam profile, measured $\phi_{th} = 1.36$ J/cm^2 for sapphire and $\phi_{th} = 1.16$ J/cm^2 for alumina while using a 7 ps, 515 nm laser at 400 kHz repetition rate [60]. Using a similar laser at 1030 nm, an indirect measurement, which is discussed in Chapter 4, showed that $\phi_{th} = 2.3$ J/cm^2 and $\phi_{th} = 2.0$ J/cm^2 for sapphire and alumina respectively. I have measured the fluence threshold for sapphire using a 80 fs, 800 nm, 1 kHz laser and the results were $\phi_{th} = 2.5$ J/cm^2 without an independently measured beam profile and $\phi_{th} = 2.1$ J/cm^2 with an independently measured beam profile; the discrepancy was attributed to the unprecise beam measurement.

Rayleigh Length and Defocusing

Rayleigh length provides a useful reference scale for how fast the fluence changes due to the Gaussian beam divergence along the direction of the laser beam z. According to Eq. 3.1 and Eq. 3.2, the Rayleigh length z_R is where the area of beam cross-section is doubled and the average fluence drops to 1/2 of that at the focal position. Rayleigh length is calculated by

$$z_R = \frac{\pi w_0^2}{\lambda}, \tag{3.11}$$

where λ is the wavelength of the laser. At the same wavelength, a smaller focus spot size $2w_0$ leads to a shorter Rayleigh length, and therefore larger beam divergence. Panel (a) in Figure 3.1 shows two ideal Gaussian laser beam profiles with same wavelength calculated with different spot sizes at the same focus position. For a fixed focus spot size, laser beam with shorter wavelength has longer Rayleigh length and therefore smaller divergence.

Assuming a normally incident laser beam, the laser focus position relative to the surface of the material is called "defocusing distance" [73–75], denoted as z_{def}. We define z_{def} such that a negative value means a focus position into the material. For example, $z_{def} = -750$ μm in the panel (a) of Figure 3.1. In all of our ablation

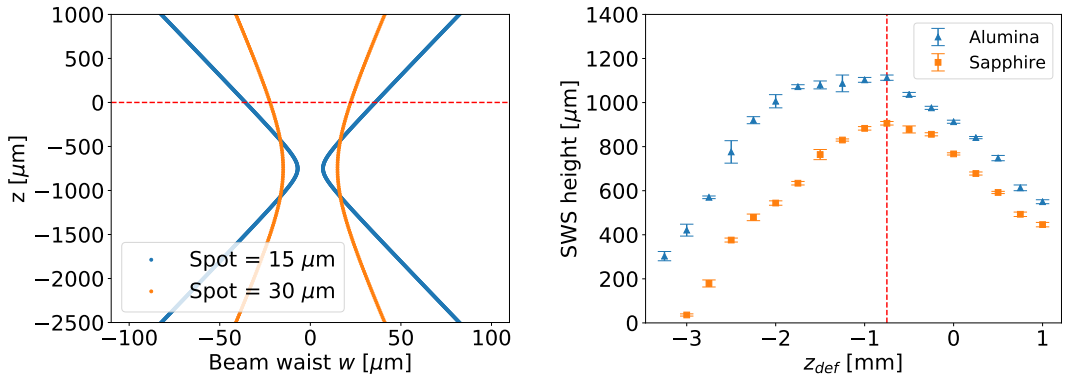

(a) (b)

Figure 3.1: Panel (a): predicted Gaussian beam profiles that have different spot diameters at the focus position 750 μm below the material surface (red horizontal dashed line), at the same wavelength 1030 nm. Panel (b): experimental result of the SWS height while only changing the defocusing distance; the maximum height was achieved at $z_{def} = -750$ μm for both materials, indicated by the vertical dashed line.

tests thus far, the defocusing distance was set at the beginning of fabrication and kept constant throughout.

We have demonstrated experimentally that when z_{def} was set and kept constant throughout an ablation process, a defocusing distance into the material over around 2 Rayleigh lengths produced the deepest structures [60, 65]. In a recent experiment [65], we repeated ablation of both alumina and sapphire while only varying the z_{def} between +1 and -3 mm, with all other parameters fixed. The Rayleigh length was measured to be 538 μm. The results, as shown in the panel (b) of Figure 3.1, indicate a relatively broad optimum for alumina, with values between $z_{def} = -0.50$ mm and $z_{def} = -2.00$ mm giving results that are within 10% of the maximum. For sapphire, the same range spans values between $z_{def} = -0.25$ mm and $z_{def} = -1.25$ mm. These results are reasonable because with negative focus more of the beam energy is confined below the surface.

3.2 Samples and Fabrications

We carried ablation tests on high-purity (about 99.5%) alumina, c-cut sapphire, and high-resistivity ($>$ 500 Ω·m) silicon flat discs, which were no larger than 100 mm in diameter. For actual SWS ARC applications, both sides of the materials need to be ablated, but for testing we have done both one-side and two-side ablation. Before fabrication, the transmittance was measured at room temperature in mm-wave bands. The optical properties such as refractive index and loss tangent were inferred from the transmittance or reflectance measurements by fitting the data using TMM; the results were consistent with what have been found in literature, as listed in the Table 2.1 in Chapter 2.

A laser setup consisted of a laser source and a galvo scanner system. Table 3.1 summarizes some but not all of the laser sources we have tested. The scanner was equipped with f-theta objective lenses with different focal lengths to achieve different spot sizes; see Table 3.1 for the spot sizes we have tested.

Laser	Trumpf TruMicro 5050	Trumpf TruMicro 5070	Pharos, PH1-15W	fs Laser
Institute / company	LZH	Trumpf GmbH & Co. KG	University of Tokyo	UMN
Location	Germany	Germany	Japan	USA
Pulse duration	7 ps	7 ps	290 fs	80 fs
Wavelength [nm]	1030	1030	1030	800
Max average power [W]	50	100	15	0.2
Repetition rate [kHz]	400	400, 600	75	1
Focal spot diameter [µm]	30 & 17	28	15.5	56

Table 3.1: Part of the laser sources that we have tested.

We used raster scan patterns to scan across the stationary surface of material to fabricate truncated pyramid-shape SWS, while the defocusing distance was fixed throughout the ablation. A scan pattern and a sketch of the side view of the SWS are shown in Figure 3.2. The SWS were formed by repeating a specific scan pattern of the laser beam N_L times across the sample; see Figure 3.3 for an example of ablation progressing on sapphire. We refer to each repeat as a 'layer' (or a 'pass' in our early publications) and thus a full fabrication consists of N_L layers (or N_p passes). Figure 3.4 shows other examples of the fabricated samples

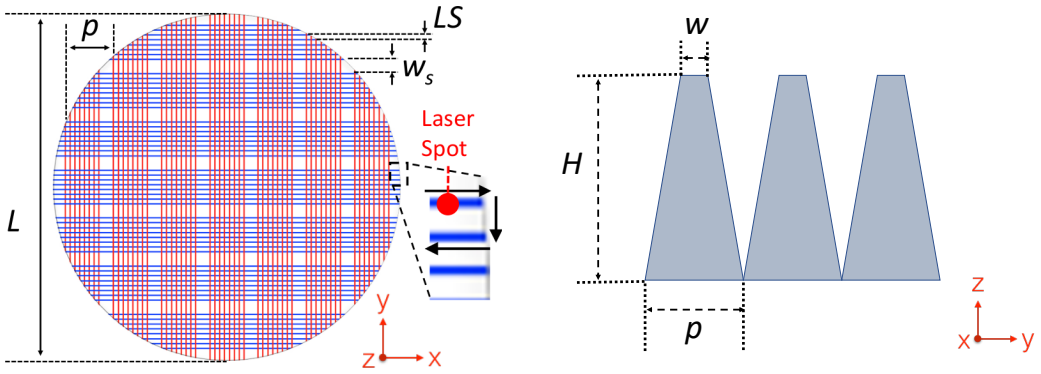

(a) (b)

Figure 3.2: **(a)** The scan pattern used to fabricate the SWS. Each line represents a scan of the laser beam. The beam scanned all parallel lines along one axis (e.g. y-axis in red) then the other; this is one layer. The laser transitions between lines by taking shortest path possible, thus adjacent line scans are opposite to each other; see enlargement. The SWS are formed by repeating this scan for N_L layers. Repeated ablation of lines spaced by LS creates grooves with pitch p over a circular or square area with side length L. **(b)** Side-view sketch of the generic design of the SWS. The structure head size w is designed to be smaller than w_s considering the spot size.

on alumina and silicon.

Scan patterns were designed based on the targeted shapes of SWS and also on the particular laser spot size being used. Recall that the pitch of SWS determines the cut-off frequency for higher-order diffractions, as described by Eq. 2.6. With refractive index above 3 for HIM, in order to have SWS ARC that work up to around 485 GHz or 175 GHz depending on specific applications, we have designed scan patterns that have pitch ranging between 180 μm and 540 μm. The groove gap w_s is designed to be about one laser spot size larger than the top head size of the desired structure. The line spacing LS follows a rule of thumb by being roughly equal to the spot size.

Height maps, as shown in the panel (a) and (b) of Figure 3.5, showed that the actual SWS had the deepest points at the locations where two perpendicular scans crossed, while the ridges at the boundaries between neighboring structures were taller than the deepest points because only one direction of scans had passed over

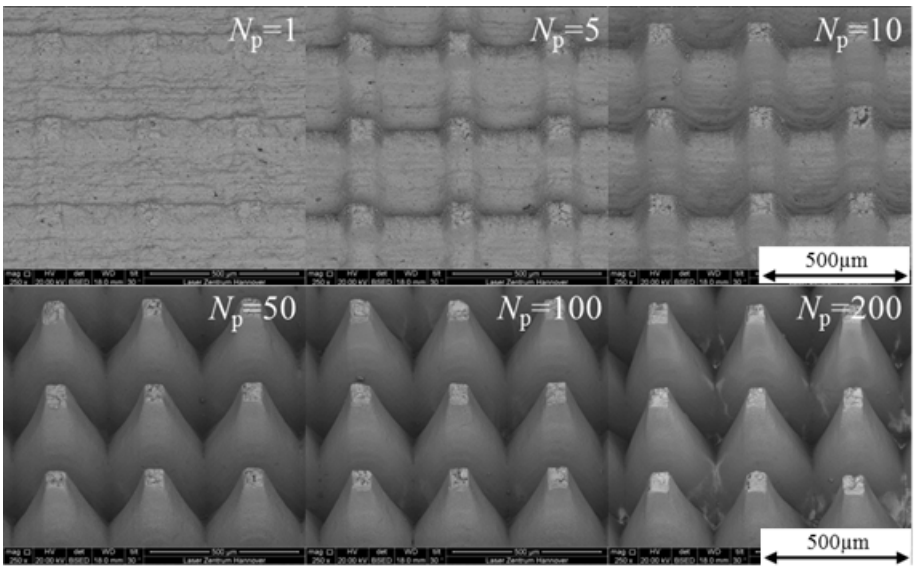

Figure 3.3: Scanning electron microscope images of pyramids on a test sapphire sample after N_L ablation scans. After $N_L = 50$ there was only minor evolution in structure shape for subsequent passes.

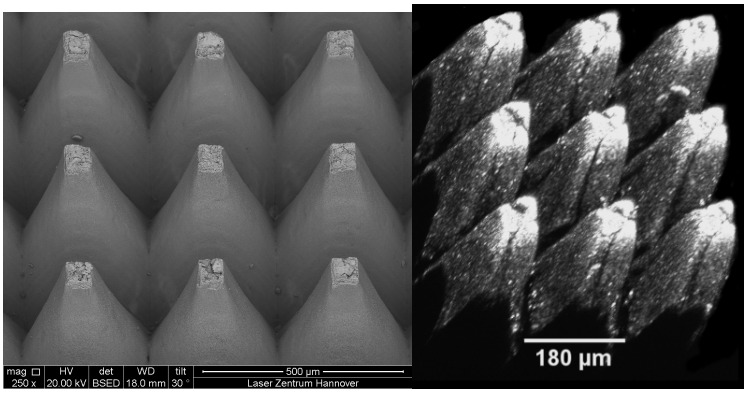

(a) Alumina (b) Silicon

Figure 3.4: Photos of laser ablated SWS on alumina and silicon. Photo (a) was taken by our collaborators in Germany using a scanning electron microscope; photo (b) was imaged by Karl Young using a Nikon A1RMP confocal microscope at the University of Minnesota Imaging Center [76].

the area. We define the structure height as the distance between the top heads and the deepest points. Aspect ratio, defined as $a \equiv$ height/pitch, is another metric that we use to characterize the fabricated structures. Table 3.2 summarizes the measured geometries, as defined in the panel (b) of Figure 3.2, as well as the aspect ratios of some samples we have fabricated and published so far.

Material	H [µm]	p [µm]	w [µm]	a	Reference
Alumina	790	313	66	2.52	[59]
Alumina	236 - 1080	400	80 - 59	2.70	[65]
Sapphire	715	325	57	2.20	[59]
Sapphire	2105	399	51	5.27	[62]
Sapphire	2040	540	120 (y),140 (x)	3.78	[44]
Silicon	720	182	-	3.96	[64]
Silicon	600 (side A), 560 (side B)	179	-	3.35	[64]

Table 3.2: Summary of some fabricated samples. The heads in fabricated silicon samples were not distinctive enough to find head size.

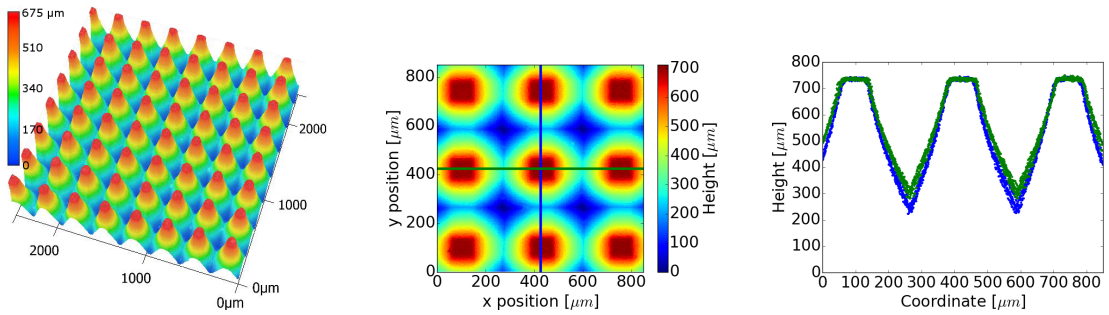

(a) (b) (c)

Figure 3.5: A sapphire sample: (a) partial 3d image; (b) top view of a small area; (c) manually aligned cross sections from six different locations cut through the horizontal (green) and vertical (blue) directions as shown in the panel (b).

We have experimentally demonstrated that the structure height depends on many parameters, including pulse energy, repetition rate, laser average power, scan speed and number of layers [60, 65]. Chapter 4 will discuss an analytical ablation model in which we successfully incorporated all these different parameters to predict the structure height.

In addition, slight asymmetries of the fabricated SWS were sometimes observed between two scan directions. To visualize the asymmetries, I had overlaid the cross sections of the fabricated structures along different scan directions, as shown in the panel (b), (c) of Figure 3.5. It can be seen that although the overall heights were similar, the green (along x) cuts had taller ridges than the blue (along y). We believe that the asymmetries were most likely related to the polarization of the laser beam. Future investigation on the sources of the structure asymmetry will be helpful.

3.3 T/R Measurements and Simulations

We measured the transmittance and/or reflectance of the fabricated samples at normal incidence. Measured transmittances were higher than 97% over a band between 43 and 161 GHz on a sapphire sample [44], and higher than 95% over a band between 210 and 490 GHz on a silicon sample [64].

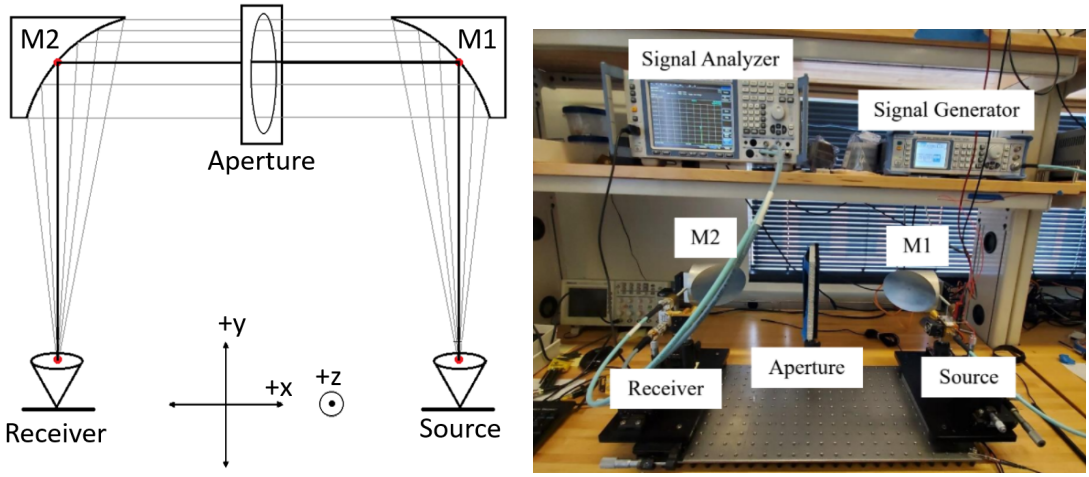

(a) (b)

Figure 3.6: Transmittance measurement setup in the Hanany's lab at the UMN; (a) top-view sketch and (b) a photo. Sample holder is on the aperture plate. Sketch and photo are credited to Cosmolabers Brandon Nguyen and Daniel Helgeson.

A transmittance measurement setup at UMN is shown in Figure 3.6, and

it measures transmittance between 75 and 110 GHz. A similar setup that our collaborators in Japan own measures transmittance between 43 and 161 GHz. A transmittance measurement is done by measuring and comparing the power received with and without the sample.

For broader-band (70 - 720 GHz) measurements of transmittance and reflectance, we did them at the Institute for Terahertz Science and Technology at the University of California, Santa Barbara. The reflectance setup was described in the study by Bailey et al [77]. The transmittance setup was similar, but the sample was placed just after the source, and a gold mirror replaced the reflectance sample. All measurements with samples were normalized using data runs without samples.

Figure 3.7 is an example of the measurement results for both transmittance and reflectance on a silicon sample, which was ablated on both sides. The height of the structures was about 600 μm and the pitch was 179 μm. This result demonstrated broadband SWS ARC achieved by laser ablation. The average reflectance between 202 and 490 GHz was 2.9%.

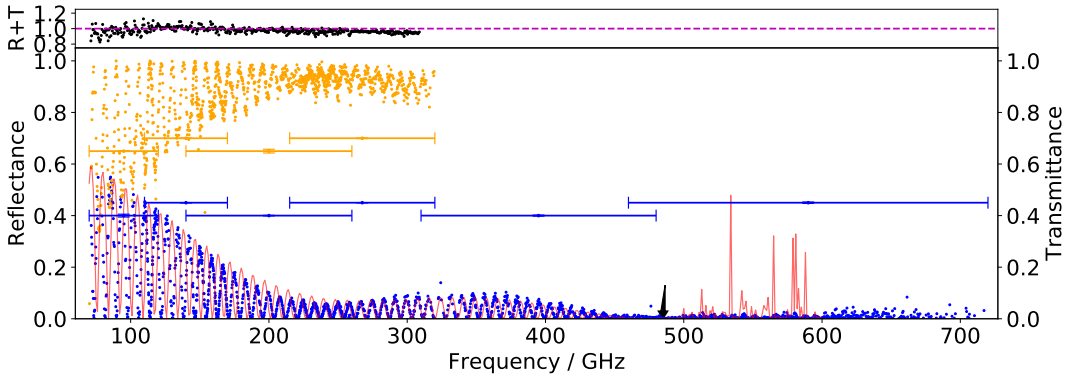

Figure 3.7: Measured reflectance (blue), transmittance (orange), and their sum (black) of a double-side ablated silicon sample as a function of frequency. FEA simulation (red) matches the overall reflectance envelope up to diffraction limit 490 GHz (black arrow), beyond which diffraction is shown to be significant as expected. For example, the error bars in the middle represent the measurement uncertainties in individual bands.

We modeled transmittance and reflectance of the fabricated samples using rigorous simulation tools such as HFSS and RCWA. Simulations helped us verify the measurements, and also enabled us to predict double-side ablated ARC performances for the structures that we only physically fabricated on one side. The red curve in Figure 3.7 was predicted reflectance from HFSS simulation using the measured shape, and the result matched the measurement very well with only slight deviations in phase.

The procedure of a simulation for fabricated structures includes building 3D model of a single structure based on the shape measurement and running electromagnetic calculations in HFSS or RCWA using periodic boundary conditions. To build a 3D model, the steps that I follow are: 1. export FITS file of a single structure from 3D image using image processing software such as ImageJ; 2. convert FITS file into acs point cloud file using python; 3. construct a 3D model in SolidWorks using the point cloud. A tip for working with point cloud in SolidWorks is using "Loft" feature when manual construction is needed.

In conclusion, we have demonstrated excellent ARC performances with laser ablated SWS from both measurements and simulations.

3.4 Volume Removal Rate

A key factor that determines the feasibility of laser-ablated SWS ARC for current and next generation MSM instruments is fabrication time. Given that commercial vendors charge around $200/hour for ultrashort pulsed laser ablation, it is desirable to have ablation work done per optical element as quickly as possible, e.g. within 100 hours, so that the cost for the process is not too expensive. Having graduate students work with in-house lasers with some help of automation is an option if the number of optical elements is just a few; but our vision is that there will be more than one hundred optical elements that can benefit from this technology, especially considering large projects like CMB S4.

Fabrication time depends on the size of an optical element and the volume

removal rate. More material needs to be removed for larger samples, and the volume removal rate quantifies how much volume of material is removed by laser ablation per unit time. Optical elements in several instruments have diameters near or larger than 500 mm [9, 13, 16, 18]. In our earliest publications, we reported volume removal rate of 1.0 mm^3/min on alumina and up to 2.2 mm^3/min on sapphire [44, 59]. With a volume removal rate of 2 mm^3/min, it would take more than 1,600 hours to ablate 1 mm-tall SWS ARC on both sides of a 500mm-diameter optical element, making this technology cost-prohibitive and schedule-unfriendly despite of all its advantages.

One of the primary goals of our research was to achieve SWS ARC volume removal rate at least near 20 mm^3/min, reducing the fabrication time of ARC on a 500 mm diameter optical element to within a week (24 hr/day).

This section discusses a few important concepts in the context of volume removal rate, and an experiment that we did to optimize the volume removal rate using a high-power (up to 100 W) picosecond laser. The experiment successfully demonstrated average ablation rates of up to 34 mm^3/min on alumina and up to 20 mm^3/min on sapphire for making structures that were about 700 - 900 μm tall [65].

3.4.1 Volume Removal Fraction

To quantify the volume removal rate achieved in any fabrication test, determining how much volume of material is removed is the first step. For given fabricated structures, it is straightforward to measure the removed volume using the shape measurements. For example, one can build a 3D model of the fabricated structure in SolidWorks based on the shape measurement, and SolidWorks provides the information about the volume of the modeled structure. The removed volume in one unit cell is simply the difference between the volume of a unit cell, i.e. $p^2 \times H$, and the volume of the modeled structure. The total removed volume of a sample is equal to the removed volume in one unit cell multiplied by the total number of

structures, which can be estimated given the scan pattern.

We define the "volume removal fraction" f_V as the removed volume per unit cell divided by the volume of a unit cell. Using the method described above with the help of SolidWorks, I measured $f_V = 51\%$, 45% and 55% for an alumina sample, a sapphire sample and a silicon sample respectively. It turned out that $f_V = 50\%$ is a good estimate for the shapes that we fabricate using 2D raster scan. It may be helpful to point out that $f_V = 66.7\%$ for a regular pyramid. Since the structures we fabricate with lasers are typically fattier than a regular pyramid with the same height, it is reasonable to expect the actual f_V to be less than 66.7%.

The volume removal fraction provides a convenient way to calculate the total removed volume. Suppose that the area of a sample is A_{sample} and the SWS have height H, then the total removed volume (on one side) is simply

$$\Delta V = f_V \times H \times A_{sample}. \tag{3.12}$$

Given that $f_V = 50\%$ is a good estimation for the volume removal fraction regardless of the exact structure shape, Eq. 3.12 is especially useful for quickly estimating the total volume that needs to be removed for future large samples. For example, assuming $f_V = 50\%$, fabricating SWS with $H = 1$ mm on both sides of a 50 cm lens requires removing 196,350 mm^3 material.

3.4.2 Average Ablation Rate and Process Rate

When quantifying the volume removal rate, a distinction between the 'average ablation rate' and the 'process rate' must be made. The distinction comes from the different definitions of the time for which we use to calculate the volume removal rate.

The 'process time' T_p is the time it takes to complete the ablation in a given fabrication process. The process time includes the "ablation time" T_a during which the laser ablates the material, and dead times during which the laser is off.

Dead time includes periods T_{trans} when the beam transitions between scan lines, as shown in Figure 3.2, and other delays T_{delay}:

$$T_p = T_a + T_{trans} + T_{delay}. \tag{3.13}$$

For a fixed SWS geometry, reducing T_p requires reducing T_a by optimizing material ablation parameters, and reducing non-ablation times T_{trans} and T_{delay} by improving process efficiency defined as $\epsilon \equiv T_a/T_p$. It is useful to make a distinction between T_a and T_p because improving T_a requires understanding and optimizing the physics of the ablation process. When increasing efficiency one concentrates on scan strategy and on removing parasitic non-ablation times.

We define the "average ablation rate" as $\overline{V_a} = \Delta V/T_a$, where ΔV is the volume of material removed during ablation time T_a. The term 'average' is important because for short time intervals, the instantaneous ablation removal rate v_{rr} and $\overline{V_a}$ are equal, but they have different values when considering the entire ablation process because v_{rr} varies as the height of the ablated structures increases. We define the 'process rate' as $\overline{V_p} = \Delta V/T_p$. Therefore,

$$\overline{V_p} = \epsilon \overline{V_a}. \tag{3.14}$$

For sufficiently high process efficiency it is possible to have $\overline{V_p} \simeq \overline{V_a}$.

The average ablation rate is intrinsic to the ablation, while process rate depends on the process efficiency. It turns out that the process efficiency depends on the overall size of the scan pattern, denoted as L in Figure 3.2; shorter scan size leads to lower process efficiency. A detailed mathematical proof is provided in the following subsection. As a result, the process rate for an ablation test done on a small area may be much smaller than the intrinsic average ablation rate due to low process efficiency. If one ignored the distinction and mistakenly extrapolated the process rate from a small-area test to an actual large-area application, one may significantly underestimate the achievable process rate for the application.

Process Efficiency vs Scan Size

The discussion in this section is based on the scan pattern shown in Figure 3.2 and the dimensions defined in there.

The ablation time T_a is equal to the ablation time per unit cell multiplied by the number of such unit cells. The effective number of unit cells is

$$N_c = \Omega L^2/p^2, \tag{3.15}$$

where Ω is a form factor with values $\Omega = \pi/4$ for a circular sample as shown in Figure 3.2, or $\Omega = 1$ for a square sample. The total ablation distance within a unit cell is $2n_{lines}p$, where n_{lines} is the number of scan lines per groove; a factor of two comes from the scans in both x and y directions. Recall that the number of layers is N_L. Therefore, the total ablation time is

$$T_a = N_L N_c(\frac{2n_{lines}p}{v_s}) = 2\Omega N_L(L/p)n_{lines}(L/v_s), \tag{3.16}$$

where v_s is the scan speed.

With the scan strategy described in the caption of Figure 3.2, the transitions between lines occur at the edge of the sample. The total transition distance per layer including both x and y directions is one half the edge perimeter for a square sample, and the entire circumference for a circular sample. The transition time is

$$T_{trans} = \begin{cases} N_L 2L/v_{trans}, & \text{square sample} \\ N_L \pi L/v_{trans}, & \text{circular sample} \end{cases} \tag{3.17}$$

$$= N_L \widetilde{\Omega} L/v_{trans}, \tag{3.18}$$

where v_{trans} is the transition speed, assumed to be constant, and another form factor $\widetilde{\Omega}$ accounts for the appropriate geometrical factor. We neglect the transitions when switching between x and y direction scans and between layers.

To calculate T_{delay} we define a delay time per line τ_{delay}, which includes motion

delays of the scanner, delays in computer-scanner communications, programmed shutter delays, and potentially other delays. Then

$$T_{delay} = 2N_L(L/p)n_{lines}\tau_{delay}. \tag{3.19}$$

With these relations the process efficiency is

$$\epsilon = \frac{T_a}{T_p} = \frac{T_a}{T_a + T_{trans} + T_{delay}} = \frac{L/v_s}{L/v_s + \tau}, \tag{3.20}$$

where τ is an average "parasitic" (= non-ablation) time per line that includes line transitions and other delays, but does not depend on the sample size L. The expressions for τ are

$$\tau(p, n_{lines}, v_{trans}, \tau_{delay}) = \begin{cases} \frac{p/v_{trans}}{n_{lines}} + \tau_{delay} & \text{, square sample} \\ \frac{2p/v_{trans}}{n_{lines}} + \frac{4}{\pi}\tau_{delay} & \text{, circular sample.} \end{cases} \tag{3.21}$$

The duration τ depends on scan parameters and hardware delay times but not on the sample size. For large samples, for which $L/v_s \gg \tau$, $\epsilon \approx 1$. Tests conducted on small samples, especially those with fast scan speed, have lower process efficiencies due to a relatively larger contribution from parasitic processes. Equation 3.18 is not valid for scan strategies in which line scans are in the same direction. In such a scan strategy τ does depend on sample size; increasing L does not necessarily increase process efficiency.

3.4.3 Optimization

Experimental Setup

Our collaborator at LZH fabricated SWS on one side of flat discs of alumina and sapphire using a Trumpf TruMicro 5070 picosecond laser (see Table 3.1 for laser parameters) at TRUMPF GmbH + Co. KG, Germany. A jet of compressed air removed ablation debris during processing, and the samples were cleaned in an

ultrasonic bath. A 100 mm focal-length lens was used to focus the laser beam, which had a beam diameter of 5.2 mm at the lens. The scan pattern again follows what is shown in Figure 3.2, and the parameters of scan patterns are given in Table 3.3.

Scan Pattern	p [µm]	LS [µm]	w_s [µm]	n_{lines}	L [mm]
#1	400	40	120	8	2.85
#2	330	30	150	7	2.46

Table 3.3: Scan patterns used to fabricate the SWS. They all followed the pattern shown in Figure 3.2.

Summary of Tests

We conducted ablation tests in which we varied the number of layers, the laser scan speed, the pulse repetition rate, and pulse energies as given in Table 3.4. We focused on varying pulse energy. For most pulse energies, as allowed by constraints of total power, we tested four configurations of N_L, repetition rate, and scan speed, adjusting the last two such that the total energy delivered per layer only depended on pulse energy.

The total process time was recorded for each trial, and post-fabrication the samples were imaged with an optical microscope to measure the geometry of the SWS. For each sample four pyramids were measured.

	Trial	Scan Pattern	Number of layers N_L	Scan speed v_s (m/s)	Repetition rate (kHz)	Pulse energy (µJ)	Average power P (W)
Alumina	1	#1	15	0.50	400	75, 100 ..., 225, 250[a]	30, 40, ..., 90, 100
	2	#1	30	0.50	400	75, 100, ..., 225, 250[a]	30, 40, ..., 90, 100
	3	#1	15	0.75	600	75, 100, 125, 150, 166	45, 60, 75, 90, 100
	4	#1	30	0.75	600	75, 100, 125, 150, 166	45, 60, 75, 90, 100
Sapphire	5	#2	40	1.00	400	75, 100 ..., 225, 250[a]	30, 40, ..., 90, 100
	6	#2	80	1.00	400	75, 100 ..., 225, 250[a]	30, 40, ..., 90, 100
	7	#2	40	1.50	600	75, 100, 125, 150, 166	45, 60, 75, 90, 100
	8	#2	80	1.50	600	75, 100, 125, 150, 166	45, 60, 75, 90, 100

[a] Pulse energy ranged between 75 and 250 µJ with 25 µJ increment.

Table 3.4: Ablation trials. For each trial we fabricated a number of samples each with the pulse energy listed. Trial 1, for example, produced eight samples.

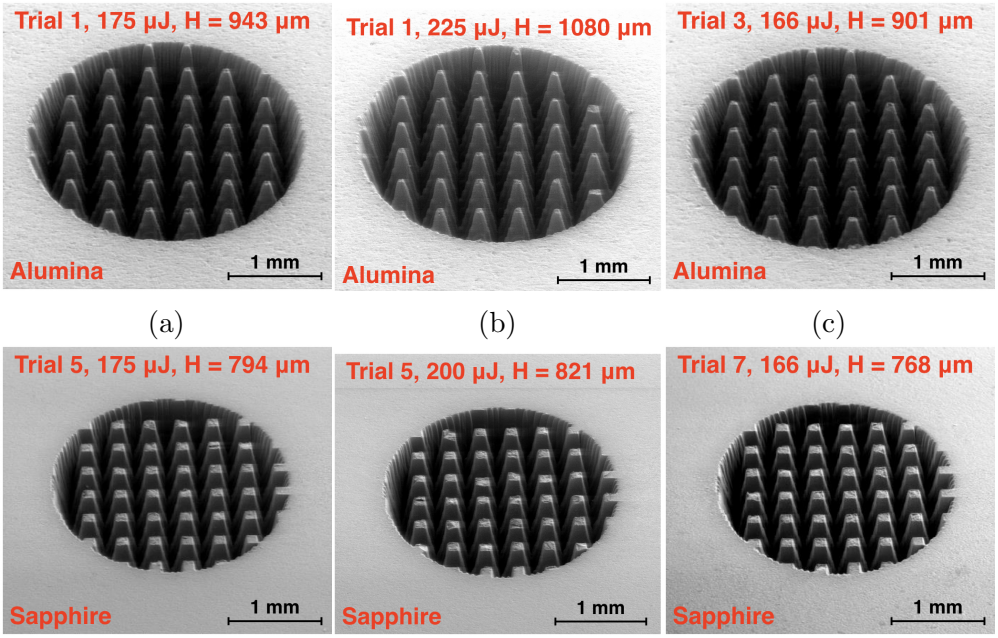

Figure 3.8: Photographs of a subset of the fabricated SWS samples. Alumina samples are shown in the top panels, and sapphire samples are shown in the lower panels.

The scan pattern produces SWS, which in the majority of cases are intact pyramid-like shapes over the entire fabrication area; see Figure 3.8. The measured pitch agrees with the design values given in Table 3.3. We find that the final height of the structures is a function of the pulse energy and the number of scan layers; see Figure 3.9. We assign a height uncertainty of 17 µm and 10 µm for alumina and sapphire, respectively, based on the average values of the measured standard deviations shown in the right panel of Figure 3.1; the measurements were done by the same person with the same tool on similar structures. In a small minority of cases, specifically for some of the highest energies and tallest structures, we find varying degree of damage to the pyramids, including breakage or cracking of tips. The data give anecdotal evidence for occasional SWS damage at structure

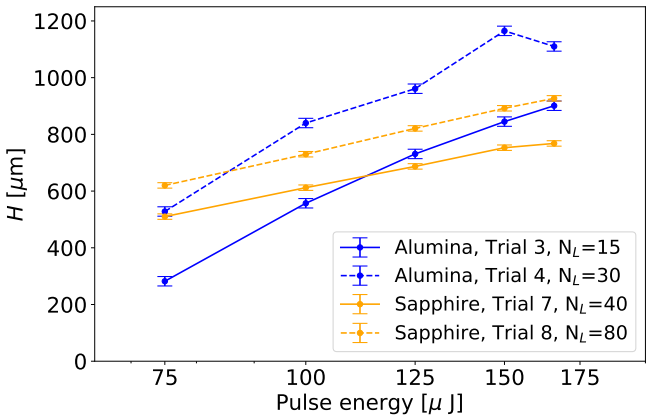

Figure 3.9: Examples of SWS height as a function of pulse energy and the number of layers N_L. Higher pulse energy and higher N_L both lead to taller structures. Lines are for visualization purpose; they connect points belonging to the same dataset

heights exceeding ∼1 mm and with pulse energies exceeding 200 μJ/pulse. A more systematic study is required to characterize and quantify this effect. The results we report conservatively exclude all trials for which alumina (sapphire) SWS height is larger than 1100 (850) µm and two sapphire samples that would have been excluded by this criterion but had significant number of broken tips and thus gave an average height below 850 µm. For the structures we report here, no pyramids are missing and the vast majority of pyramids are completely intact; Figure 3.8 is representative. With these heights and the measured pitch the maximum aspect ratios are $a = 2.75$ and 2.6 for alumina and sapphire, respectively. The measured head size w is correlated with structure height such that w is somewhat smaller for taller structures. Even with this correlation the standard deviation for w is only 10%. The average and standard deviation for all pyramids and all samples are $w = 70 \pm 7$ µm on alumina and 82 ± 8 µm on sapphire.

In Table 3.5, we give the process and ablation times, the calculated process efficiency, and the inferred duration τ for each of the trials. The ablation time T_a was calculated based on Equation 3.16 and the known laser scan parameters.

	Trial	T_p [s]	T_a [s]	ϵ [%]	τ [ms]
Alumina	1	9.9 ± 0.1	7.7 ± 0.2	77 ± 2	1.7 ± 0.2
	2	19.6 ± 0.1	15.3 ± 0.5	78 ± 2	1.6 ± 0.2
	3	7.1 ± 0.1	5.1 ± 0.2	72 ± 2	1.5 ± 0.2
	4	14.4 ± 0.6	10.2 ± 0.3	71 ± 4	1.6 ± 0.3
Sapphire	5	13.7 ± 0.2	8.1 ± 0.2	59 ± 2	1.7 ± 0.1
	6	27.3 ± 0.2	16.1 ± 0.5	59 ± 2	1.7 ± 0.1
	7	10.5 ± 0.1	5.4 ± 0.2	51 ± 2	1.6 ± 0.1
	8	21.1 ± 0.3	10.8 ± 0.3	51 ± 2	1.6 ± 0.1

Table 3.5: Summary of the experimental process and ablation times, process efficiencies, and derived parasitic times. We show the average of recorded T_p with the standard deviation, since the same scanning was repeated over different pulse energies. The errors for T_a, ϵ and τ are the standard deviations after uncertainty propagation.

Figure 3.10 gives average ablation rate as a function of laser power. The volume removal fraction f_V is assumed to be 50% ± 5%. The total removed volume is calculated using Eq. 3.12, with H equaling to the measured height of the fabricated structures and $A_{sample} = \pi L^2/4$. The data show that an increase in laser power leads to higher average ablation rate, however the increase is not linear and depends on specific laser and scan parameters. The highest average ablation rate measured was 34 and 20 mm^3/min on alumina and sapphire; this rate was measured with SWS height $H \approx 900$ µm and $H \approx 750$ µm, respectively.

Discussion and Conclusion

Equation 3.20 quantifies the dependence of process efficiency on scan parameters. It shows that ϵ increases as sample size L increases. Figure 3.11 shows projections of process efficiencies as a function of L for different scan settings, as well as two of our data points; one with the lowest efficiency and one with the highest. Curves for other data presented in this experiment would be located between the two shown curves. When fabricating a sample with diameter larger than ∼20 mm using laser scan parameters similar to the ones we used for this work, minimizing

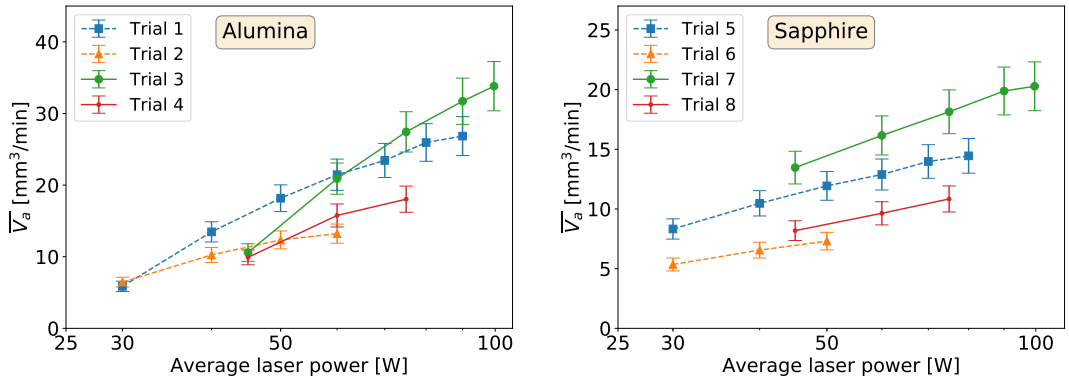

(a) (b)

Figure 3.10: Measured average ablation rate vs. laser power for **(a)** alumina and **(b)** sapphire. Error bars include uncertainty in the height measurements and the ±5% uncertainty in estimating the volume removed. Lines between the points are only for visual guidance.

τ should be a lower priority, as the process efficiency is near 90%. In all cases, efficiencies are larger than 95% for sample sizes larger than 60 mm.

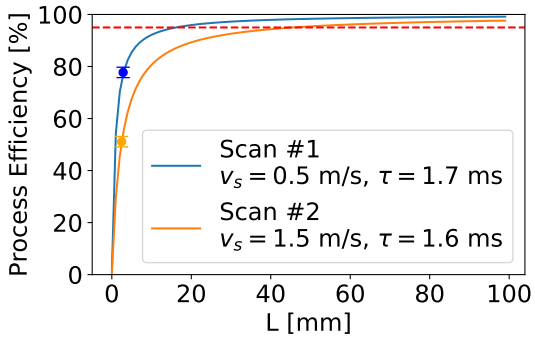

Figure 3.11: Process efficiency as a function of sample size L for two scan settings based on Eq. 3.20 and measured τ. The dots are measured data and the red horizontal line is at 95%.

The data gave a measured average ablation rate $\overline{V_a}$ up to 34 and 20 mm^3/min on alumina and sapphire with SWS height $H \approx 900$ µm and $H \approx 750$ µm,

respectively. The highest average rates were both obtained with laser power $P =$ 100 W. These rates are a factor of 34 and 9 higher than reported previously on similar structures [59]. The improvement was a result of both higher laser power and better optimized scan parameters.

Another useful figure of merit is the specific average ablation rate $\overline{V_s}$ defined as the average ablation rate per unit laser power, i.e. $\overline{V_s} = \overline{V_a}/P$, where P is the average incident laser power. We find values of $\overline{V_s}$ reaching 0.37 mm^3/min/W on alumina and 0.30 mm^3/min/W on sapphire; the highest values were obtained with 75 W and 45 W average laser power for alumina and sapphire, respectively. Schille et al. [78] reported an ablation rate of 129 mm^3/min on alumina using a 187 W ps-laser, giving $\overline{V_s} = 0.69$ mm^3/min/W; Engelhardt et al. [79] reported 205 µm^3/pulse with 25 µJ/pulse and 200 kHz repetition rate, giving $\overline{V_s} = 0.49$ mm^3/min/W. In those experiments the structures ablated were cavities with flat bottom surfaces and the highest rates were obtained near optimum peak fluence (see Chapter 4). Flat surface cavities are conducive to higher ablation rates relative to pyramid-shape SWS because with pyramid shapes (1) the projected fluence is continuously decreasing during ablation, (2) reflection losses are higher due to oblique incidence angles, and (3) it is more difficult to remove ablation debris which scatters some of the incident beam.

In conclusion, we tested a range of ablation parameters for fabricating millimeter-wave SWS structures on alumina and sapphire. We used a 1030 nm picosecond laser that had up to 100 W average power and achieved average ablation rates of 34 and 20 mm^3/min with alumina and sapphire SWS heights of 900 and 750 µm, respectively; the aspect ratios of these structures are 2.75, and 2.6, respectively. The highest specific rates achieved were 0.37 and 0.3 mm^3/min/W, and they were obtained with laser power of 75 and 45 W, respectively. We demonstrated improvements in average ablation rate of up to a factor of 34 with alumina and 9 with sapphire compared to previously reported rates for making similar structures. With the higher rates, laser-ablating 1 mm tall SWS ARC on a 500 mm diameter optical element finishes within a weeks, instead of a few months. The significant

reduction of processing time makes this technology competitive for broad-band, cryogenically robust, anti-reflection coatings in the MSM astronomy community.

Chapter 4

SWS ARC: An Ablation Model

The dispersion in volume removal rates described in the last chapter highlights the importance of modeling the ablation process and of establishing relations between laser parameters, fabricated shapes, and ablation rates.

When modeling the interaction between ultrashort pulses and dielectric materials, single- or multiple-rate-equation models are useful for describing the temporal evolution of free electrons in the material; see Balling and Schou [80] and Rethfeld et al. [81], and references therein. Hydrodynamic and molecular dynamic simulations provide insights into the mechanism of laser induced material changes (Ibid.). Limited computational resources make the implementation of these models prohibitive for simulating the end-to-end production of SWS ARC.

A more suitable approach is to use a model appropriate for an industry-scale high-throughput ablation [82–85]. Such a model necessarily includes simplifying assumptions, but has been shown to produce results that fit well with experimental data for both metals and dielectrics. However, previous studies did not consider a complex and continuously evolving structure being ablated, which is what we are dealing with for the laser ablated SWS. During the ablation of SWS, the incident angle between the laser beam and ablation surface changes because of the changing structure shape, and this adds complexity into any attempt of constructing a model that can describe the ablation process.

This chapter partially reproduces Wen et al. [65], in which we reported an ablation model that was extended from previous studies mentioned above. Based on various assumptions, this model provides an analytical relation between the height of the SWS and the cumulative fluence required to achieve that height. Compared to the published paper, this chapter provides more details about the model derivation especially for the assumptions involved, as well as other aspects including data analysis and guidance for future works.

4.1 Model Derivation

4.1.1 Instantaneous Volume Removal Rate

A model for ultrashort-pulse ablation was first proposed by Furmanski et al. [82] and then developed by others [83–89]. The model predicts the instantaneous volume removal rate for a normally-incident laser beam with a Rayleigh length that is long compared to the ablation depth.

The model uses the laser fluence as a key parameter. In the Section 3.1, the basics of laser fluence have already been discussed. Recall that for a Gaussian laser beam propagating along a coordinate z, the fluence as a function of beam radius and z is

$$\phi(r,z) = \phi_0 \left(\frac{w_0}{w(z)}\right)^2 e^{-2r^2/w^2(z)}. \tag{3.1}$$

If we assume that the laser beam is focused on the ablation surface or more generally that the Rayleigh length is much longer than the defocusing distance, and that the laser beam is normally incident on the material surface, the fluence on the material surface is then

$$\phi(r) = \phi_0 e^{-2r^2/w_0^2}. \tag{4.1}$$

For ablation to happen, the basic condition is that the peak fluence ϕ_0 is larger

than the ablation threshold ϕ_{th}. Since the local fluence drops from the peak fluence at the center going out radially, there exists a circular boundary r_{abl} where the local fluence is equal to the ablation threshold. Ablation terminates outside this circular boundary. By definition,

$$\phi_{th} = \phi_0 e^{-2r_{abl}^2/w_0^2} \rightarrow r_{abl} = \sqrt{\frac{w_0^2}{2} \ln \frac{\phi_0}{\phi_{th}}}. \tag{4.2}$$

To model the volume removed by laser ablation, the dimension of the ablated depth needs to be investigated as well. In the model, the energy absorption in the direction perpendicular to the ablation surface, is assumed to follow the Beer-Lambert law. Mathematically, the ablated depth z_{abl} depends on the fluence in the following way,

$$z_{abl}(r) = \delta \ln \frac{\phi(r)}{\phi_{th}}, \tag{4.3}$$

where δ is the absorption length and is assumed to be much smaller than the Rayleigh length of the laser beam. This relationship between the ablated depth and fluence has been experimentally observed in ablating metal, composite material, semi-conductor, glass [90–94]. The ablation depth is deepest at the center where $\phi(r) = \phi_0$, and becomes shallower toward the outer edge; the shape is essentially a crater. Figure 4.1 shows a predicted crater ablated by a single pulse; note that the depth and radius are not in the same scale and the crater is actually quite shallow. The edge of this crater on the top surface is exactly the circular boundary mentioned before, at which $\phi(r) = \phi_{th}$.

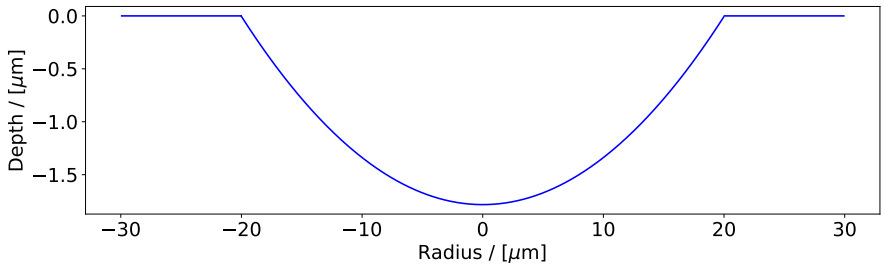

Figure 4.1: Calculated shape of a crater ablated by a single laser pulse. The assumed parameters: average laser power = 100 W, repetition rate = 200 kHz, $1/e^2$ spot diameter = 30 μm, $\phi_{th} = 2.0$ J/cm^2 and $\delta = 500$ nm.

The model assumes that the pulses are sufficiently short so that the heat diffusion during a pulse is much smaller than the absorption length. This means that the ablated volume is entirely confined by the crater. Combining Eq. 4.1, 4.2, and 4.3, the volume of a crater ablated by a single pulse can be calculated. Given the ablation depth as a function of the radius, the volume is simply an integration of the depth over surface area, as shown below.

$$
\begin{aligned}
V_{crater} &= \int z_{abl}(r) dS \\
&= \int_0^{2\pi} d\theta \int_0^{r_{abl}} z_{abl}(r) r dr \\
&= 2\pi \int_0^{r_{abl}} \delta ln\left(\frac{\phi_0 e^{-2r^2/w_0^2}}{\phi_{th}}\right) r dr \\
&= 2\pi\delta \left[\int_0^{r_{abl}} ln\left(\frac{\phi_0}{\phi_{th}}\right) r dr - \int_0^{r_{abl}} \frac{2r^2}{w_0^2} r dr\right] \\
&= 2\pi\delta \left[ln\left(\frac{\phi_0}{\phi_{th}}\right)\frac{1}{2}r^2\Big|_0^{r_{abl}} - \frac{r^4}{2w_0^2}\Big|_0^{r_{abl}}\right] \\
&= 2\pi\delta \left[ln\left(\frac{\phi_0}{\phi_{th}}\right)\frac{1}{2}\frac{w_0^2}{2} ln\left(\frac{\phi_0}{\phi_{th}}\right) - \frac{\frac{w_0^4}{4} ln^2\left(\frac{\phi_0}{\phi_{th}}\right)}{2w_0^2}\right] \\
&= \frac{1}{4}\pi\delta w_0^2 ln^2\left(\frac{\phi_0}{\phi_{th}}\right). \qquad (4.4)
\end{aligned}
$$

The model assumes that the interaction between each pulse and the material is independent of the previous pulse. Therefore, for a laser beam with repetition rate f, the total volume ablated per second, i.e. instantaneous volume removal rate v_{rr} is therefore

$$v_{rr} = \frac{1}{4} f \pi \delta w_0^2 ln^2 \left(\frac{\phi_0}{\phi_{th}} \right). \tag{4.5}$$

Since the average laser power P is equal to the pulse energy E_p multiplied by the repetition rate, the instantaneous volume removal rate can also be written in terms of the average laser power as following.

$$\begin{aligned} v_{rr} &= \frac{1}{4} f \pi \delta w_0^2 ln^2 \left(\frac{\phi_0}{\phi_{th}} \right) \\ &= \frac{1}{4} \frac{P}{E_p} \pi \delta w_0^2 ln^2 \left(\frac{\phi_0}{\phi_{th}} \right) \\ &= \frac{\delta P}{2\phi_0} \ln^2 \left(\frac{\phi_0}{\phi_{th}} \right). \end{aligned} \tag{4.6}$$

In the last step above, Eq. 3.4 $\phi_0 = \frac{2E_p}{\pi w_0^2}$ is used.

Interestingly, Eq. 4.6 indicates that at a fixed average laser power, an increasing peak fluence ϕ_0 does not necessarily improve the instantaneous volume removal rate. In fact, by taking the derivative of Eq. 4.6, one can show that there is an optimum peak fluence $\phi_0 = e^2 \phi_{th}$ at which v_{rr} per laser power is at maximum [84],

$$\left(\frac{v_{rr}}{P} \right)_{optimum} = \frac{\delta}{2e^2 \phi_{th}}. \tag{4.7}$$

4.1.2 Model Extension to SWS

In the ablation of SWS, we set the laser beam to be normally incident on the sample disk. At the very beginning of the ablation, the laser beam is normally incident on the local ablated area. However, as the ablation progresses and structures emerge, the incident angle between the laser beam and the local material is no longer zero and in fact it increases as the structures become taller. In the

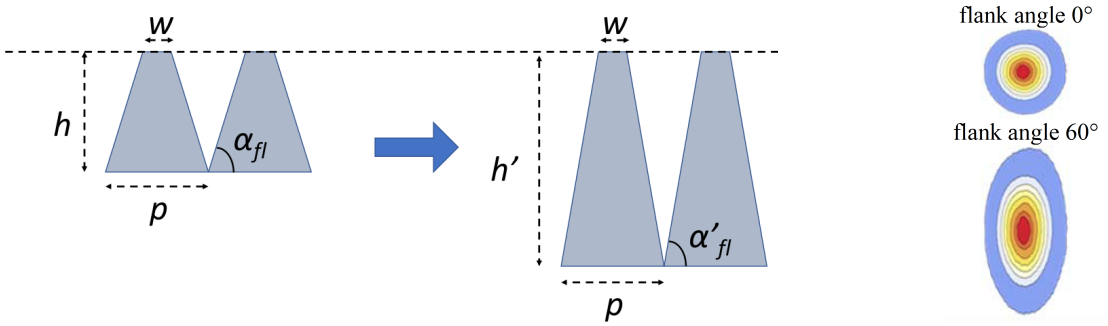

(a) (b)

Figure 4.2: (a) In the ablation model we assume that ablation height h increases to h' while the pitch p and the tip width w are constant. The flank angle α_{fl} evolves to α'_{fl}. (b) different projected fluences due to the flank angle [60].

Panel (a) of Figure 4.2, the laser beam is assumed to illuminate the sample from above in the vertical direction and the incident angle relative to the material is equal to the flank angle of the structure. One direct consequence of an oblique incident angle is that the projected laser spot on the material is stretched from $2w_0$ to $2w_0\cos(\alpha_{fl})$ in one direction and therefore the projected fluence follows asymmetrical Gaussian distribution, as shown in the Panel (b) of Figure 4.2.

With an arbitrary incident angle α_{fl}, Boerner et al. [85] have shown by integrating the ablation depth in elliptic cylindrical coordinates that the instantaneous volume removal rate modeled by Eq. 4.5 and Eq. 4.6 needs to be modified as following

$$v_{rr} = \frac{1}{4\cos(\alpha_{fl})} f\pi w_0^2 \delta \ln^2\left(\frac{\phi_0\cos(\alpha_{fl})}{\phi_{th}}\right) = \frac{\delta P}{2\phi_0\cos(\alpha_{fl})} \ln^2\left(\frac{\phi_0\cos(\alpha_{fl})}{\phi_{th}}\right). \tag{4.8}$$

Eq. 4.8 can also be intuitively obtained by replacing the peak fluence ϕ_0 in Eq. 4.6 with a "projected peak fluence" $\phi_{0,proj} = \phi_0\cos(\alpha_{fl})$ due to oblique incidence. Refraction is assumed to be normal to the surface regardless of the incidence angle. This behavior is expected for metals with high electrical conductivity σ for which the angle of refraction α_r satisfies $\tan\alpha_r = \sqrt{\frac{2\omega\epsilon_0}{\sigma}}\sin\alpha_i$, where ω is

the angular frequency of the incident light [95]. For metals, α_r is very small because $\sqrt{\frac{2\omega\epsilon_0}{\sigma}}$ is very small; for example, for zinc ($\sigma = 1.7 \times 10^7$ S/m) at 1030 nm, $\sqrt{\frac{2\omega\epsilon_0}{\sigma}} = 0.044$. The metallic behavior is justified even for wide-bandgap materials because of the high power, short-pulse ablation [85].

There is energy loss due to reflections during ablation. According to the Fresnel equations [34], the reflection increases to 100% as the incident angle approaches to 90 degrees. Since the SWS that we fabricate have flank angles as high as about 85 degrees, the loss due to reflection should be considered in the modeling. Although the interaction between an ultrashort pulsed laser beam and wide-bandgap materials is complicated as discussed in Section 3.1, we assume that the reflection is governed by linear optics and we use the Fresnel equations to calculate the reflection.

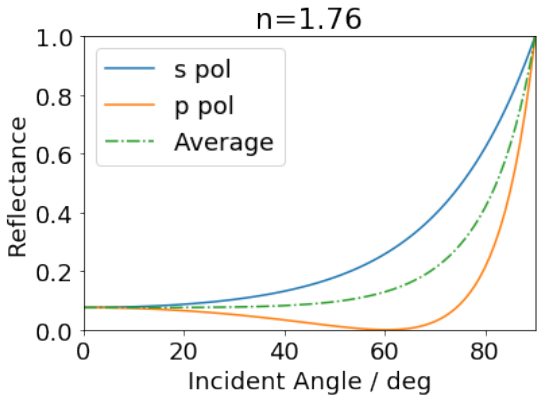

Figure 4.3: Fresnel reflectance off alumina/sapphire surface as a function of incident angle, for both s (blue, perpendicular to the plane of incidence) and p (orange, parallel to the plane of incidence) polarization states and the average of the two (green). An s state is parallel to the V-grooves in Figure 4.2, while p state is perpendicular to the V-grooves.

Figure 4.3 shows calculated Fresnel reflectance vs incident angle for alumina or sapphire at 1030 nm and at different polarization states, given the refractive index $n = 1.76$ at the wavelength [96]. Based on the panel (a) of Figure 4.2, the plane of incidence is parallel to the plane of the page and perpendicular to the V-grooves.

Thus, a polarization of laser beam that is parallel to the V-grooves is the "s state", while the one that is perpendicular to the V-grooves is the "p state". Since an "s state" is expected to experience larger reflection than a "p state" according to Figure 4.3, one may expect a larger reflection loss and therefore less ablation if the laser beam is in the "s state" rather than the "p state". This might explain the slight asymmetries of the structure shape between x and y scan directions, which we mentioned in Chapter 3. More investigation on how the polarization of laser beam affects ablation can help.

We include energy loss due to reflections into the modeling. Since both the delivered laser power and fluence on the material is affected by reflection, Eq. 4.8 becomes

$$\begin{aligned} v_{rr} &= \frac{\delta\, P\,[1-R(\alpha_{fl})]}{2\phi_0\,\cos(\alpha_{fl})\,[1-R(\alpha_{fl})]}\ln^2\left\{\frac{\phi_0\,\cos(\alpha_{fl})\,[1-R(\alpha_{fl})]}{\phi_{th}}\right\} \\ &= \frac{\delta\, P}{2\phi_0\,\cos(\alpha_{fl})}\ln^2\left\{\frac{\phi_0\,\cos(\alpha_{fl})\,[1-R(\alpha_{fl})]}{\phi_{th}}\right\}, \end{aligned} \tag{4.9}$$

where $R(\alpha_{fl})$ is the Fresnel reflectance as a function of flank angle; without specification, we use the average values of the s and p states.

We extend the model to include the entire ablation process of making the SWS. We assume that the remaining material after ablation emerges as a 3D symmetrical trapezoid and the ablation proceeds along the triangular geometry vertically shown in a sideview Figure 4.2, with w and p constant. With this geometry, the flank angle and the reflectance R are a function of the varying structure height h. Specifically for the flank angle

$$\cos(\alpha_{fl}) = \frac{1}{\sqrt{1+4x^2}} \equiv g(h); \quad x = \frac{h}{p-w} = \frac{a}{1-w/p}\ . \tag{4.10}$$

With the assumption of the trapezoid shape, we re-write Eq. 4.9 as

$$v_{rr}(h) = \frac{\delta\, P}{2\phi_0\, g(h)}\ln^2\left\{\frac{\phi_0\, g(h)\,[1-R(h)]}{\phi_{th}}\right\}, \tag{4.11}$$

Since the volume of a 3D symmetrical trapezoid in a unit cell with area p^2 and height h can be calculated by

$$V_{trapezoid} = \frac{1}{3}hp^2(1 + \frac{w}{p} + \frac{w^2}{p^2}), \tag{4.12}$$

the volume of material removed in a unit cell is

$$V_{removed-cell} = hp^2 - V_{trapezoid} = \frac{1}{3}hp^2(2 - \frac{w}{p} - \frac{w^2}{p^2}). \tag{4.13}$$

Over the entire sample area A_{sample}, the total volume of material removed is therefore

$$V_{removed} = \frac{1}{3}hA_{sample}(2 - \frac{w}{p} - \frac{w^2}{p^2}), \tag{4.14}$$

When modeling the laser ablation, it is reasonable to include only the regions where the laser beam interacts with the material, not the entire sample area A_{sample} on which SWS have been fabricated; see Figure 3.2. Considering the fact that the top heads of SWS are where no ablation happened, we define the "ablated area" A_a as

$$A_a = A_{sample}(1 - w^2/p^2), \tag{4.15}$$

where the quantities w, p have been defined in Figure 3.2. We have ignored the edge effects around the sample where partial unit cells are located. For several samples we discussed in Section 3.4, I compared the actual measured ablated area to the values obtained using Equation 4.15 and found that they agree within 3%, and we therefore use the analytical estimation for subsequent derivations. Now we can rewrite the total volume of material removed in terms of the ablated area as

$$V_{removed} = khA_a, \quad k = \frac{\frac{1}{3}(2 - \frac{w}{p} - \frac{w^2}{p^2})}{1 - (\frac{w}{p})^2}. \tag{4.16}$$

We define an important quantity in our ablation model "cumulative fluence" F_{cum}, which is the ratio of the total energy carried by the laser beam E to the ablated area, as

$$F_{cum} \equiv E/A_a = PT_a/A_a, \tag{4.17}$$

where again P is the average laser power and T_a is the total ablation time.

Suppose during a short time interval Δt, ablation makes the height of all structures over the entire sample evolve from h to h' as shown in Figure 4.2 and $\Delta h = h' - h$. According to Eq. 4.16, the volume ablated is $kA_a\,\Delta h$. The definition of 'short' is relative to the total ablation time T_a. For example, the time for finishing one layer of scan can be seen as a short time if the entire ablation has many layers. On the other hand, assuming that the instantaneous volume removal rate v_{rr}, as defined in Eq. 4.11, is a constant during this short time interval, the total volume removed should be equal to $v_{rr}\Delta t$. The assumption of a constant v_{rr} is equivalent to assuming $h \approx h'$. Therefore,

$$kA_a\,\Delta h = v_{rr}\,\Delta t = \frac{\delta}{2}\frac{P}{\phi_0\,g(h)}\ln^2\left\{\left(\frac{\phi_0}{\phi_{th}}\right)[1-R(h)]\,g(h)\right\}\Delta t. \tag{4.18}$$

We have assumed that the peak fluence ϕ_0 is constant in the z direction, so that v_{rr} is constant at a given structure height h. This assumption is equivalent to assuming an infinitely long Rayleigh length; we discuss this assumption in Section 4.4. Collecting the geometrical factors of structures on one side and time variables on the other, assuming that Δh is much smaller than H, and integrating, we obtain an expression relating the height of fabricated structures to the cumulative fluence

$$\int_0^H \frac{2k\phi_0\,g(h)\,dh}{\delta\ln^2\left\{\left(\frac{\phi_0}{\phi_{th}}\right)[1-R(h)]\,g(h)\right\}} = \int_0^{T_a}\frac{P\,dt}{A_a} = \frac{P\,T_a}{A_a} = F_{cum}. \tag{4.19}$$

The integrand consists of two known functions g and R which depend on the

geometry of the structure, two unknown parameters δ and ϕ_{th} which can be measured independently, and the peak pulse fluence ϕ_0 which is a known parameter depending on pulse energy and spot size.

Conceptually, Eq. 4.19 may be understood from two perspectives. The first one is from a prediction point of view that with a certain cumulative fluence provided, one can predict what height of structures H will be achieved so that the integration on the left hand side is equal to the provided cumulative fluence. The other perspective is from experimental design that with a targeted structure height H, the cumulative fluence needed is simply a function of the target height $F_{cum}(H)$; higher the target H is, larger the F_{cum} needs to be.

Alumina and sapphire are polycrystalline and single-crystalline α-Al_2O_3, respectively, with a bandgap of 8.8 eV [67]. The photon energy is only 1.2 eV at 1030 nm, and the bandgap is significantly larger. Therefore, the initial excitations are dominated by 7- or 8-photon MPI. Theoretical considerations and experimental evidence indicate that in this situation, the absorption length δ is a function of the incident intensity [68, 80, 97–99]. Assuming a linear dependence of the effective absorption coefficient α_{eff} on intensity – thus deviating from linear theory in which α is constant – we write

$$\alpha_{eff} = \alpha(1 + \gamma I) \equiv \frac{1}{\delta}. \tag{4.20}$$

Since peak fluence is proportional to intensity, the absorption length δ is a function of two parameters α and $\hat{\gamma}$ that can be determined by experiment

$$\delta = \frac{1}{\alpha(1 + \hat{\gamma}\phi_0)}. \tag{4.21}$$

4.1.3 Predicting Average Ablation Rate

The model can be used to provide prediction of average ablation rate for any desired structure height in the following way:

$$\overline{V_a}(H) = \frac{\Delta V(H)}{T_a(H)} = \frac{f_V A_{sample} H}{A_a F_{cum}(H)/P} = \frac{1}{(1 - w^2/p^2)} \frac{f_V H P}{F_{cum}(H)}, \tag{4.22}$$

where for $\Delta V(H)$ we assume a volume removal fraction f_V, and we expressed T_a in terms of cumulative fluence, average laser power and ablation area. For a given target height H, the cumulative fluence can be calculated using Equation 4.19. The fraction f_V and the model predicted cumulative fluence $F_{cum}(H)$ depend on the geometry being ablated and parameters of laser and scan.

Eq. 4.22 provides a very useful guidance for how to systematically optimize the average ablation rate. For a targeted array of SWS, whose w, p, H and f_V are all fixed, optimizing $\overline{V_a}(H)$ means improving the ratio between average laser power and cumulative fluence needed, i.e.

$$\overline{V_a}(H) \propto \frac{P}{F_{cum}(H)}. \tag{4.23}$$

This suggests that minimizing the $F_{cum}(H)$ and maximizing the average laser power are both effective ways to improve $\overline{V_a}(H)$. A theoretical minimum $F_{cum}(H)$ may be found by varying the peak fluence ϕ_0 when doing the integration in Eq. 4.19, and the corresponding optimal ϕ_0 may be used to guide ablation experiments.

4.2 Model Verification

We examined the ablation model by applying it on the samples that we already fabricated and discussed in Section 3.4.

For each sample I calculated the cumulative fluence using Eq. 4.17 based on the data shown in in Section 3.4.3. I plotted the measured structure height H

vs cumulative fluence F_{cum} in Figure 4.4 for all trials, which were summarized in Table 3.4. Figure 4.4 shows that within a given trial, the height of the SWS is by-and-large a monotonically increasing function of F_{cum}. Within each trial, the F_{cum} increased because the pulse energy increased, so did the peak fluence ϕ_0. The trial pairs (1,3), (2,4), (5,7), and (6,8), where the curves overlap, share the same N_l; the repetition rate and scan speed were adjusted to maintain the same F_{cum}.

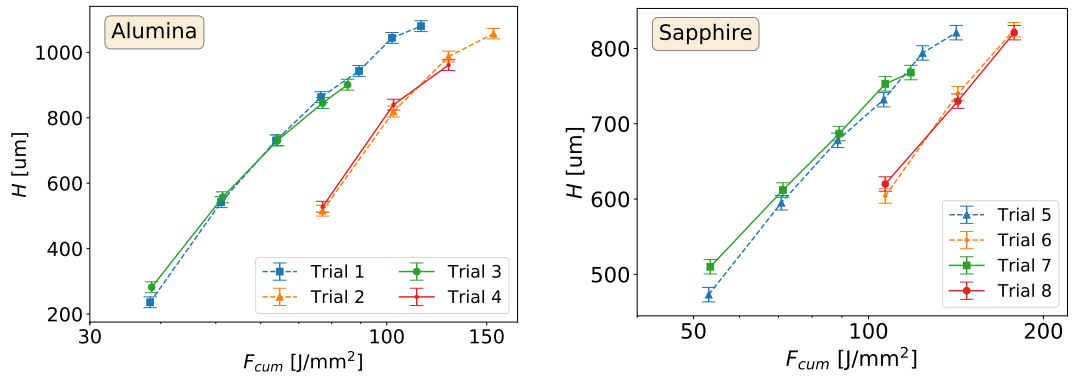

(a) (b)

Figure 4.4: SWS height H as a function of cumulative fluence F_{cum} for the **(a)** alumina and **(b)** sapphire samples.

Since we did not measure the ablation threshold ϕ_{th} or absorption length δ independently for this experiment, we chose to fit the data of structure height vs cumulative fluence using the ablation model and to find the inferred ϕ_{th} and δ. The model would be verified if (1) the fitting produced quantitatively close results compared to the data shown in Figure 4.4 and (2) the inferred ϕ_{th} and δ were reasonable compared to their values found in literature.

4.2.1 Model Fitting to Experimental Data

For every data point in Figure 4.4, we had the values of all parameters except for ϕ_{th} and δ, which is quantified by α and γ according to Eq. 4.21, to carry out

the integration on the left hand side of Eq. 4.19. For example, the peak fluence ϕ_0 was calculated based on the known pulse energy and fixed spot size. For each material, to find the best fit ϕ_{th}, α, and γ, I used a least-square method using all the measured SWS height and F_{cum}. The results are given in Table 4.1 together with uncertainties based on 68% $\Delta\chi^2$ intervals.

Material	ϕ_{th} [J/cm^2]	α [μm^{-1}]	$\hat{\gamma}$ [μm^{-1}/(J/cm^2)]
Alumina	$2.0^{+0.5}_{-0.5}$	$2.1^{+1.3}_{-0.9}$	$-0.005^{+0.003}_{-0.002}$
Sapphire	$2.3^{+0.1}_{-0.1}$	$0.70^{+0.48}_{-0.18}$	$0.026^{+0.012}_{-0.016}$

Table 4.1: Model parameters and 68% confidence intervals obtained from fitting the data.

Some details of the least-square fitting are given here for interested readers. For each material, I swept over a range of ϕ_{th}, α, and γ and calculated the integral in Eq. 4.19 using the height H and other parameters for all data points. The integration result was model predicted cumulative fluence F^m_{cum} and was compared to the actual fluence F_{cum}. At each combination of ϕ_{th}, α, and γ, I summed the squared deviations between F^m_{cum} and F_{cum} over all samples. The combination that produced the minimum sum gave the best fit ϕ_{th}, α, and γ.

The uncertainties were obtained by comparing the chi-square values at the best fit and the chi-square values with varying ϕ_{th}, α, and γ. The degree of freedom was $\nu = 3$ because of three free parameters. With $\nu = 3$, $\Delta\chi^2$ is expected to be less or equal to 3.53 at a 68% confidence-level [100]. So I quantified the uncertainties such that the combinations of ϕ_{th}, α, and γ gave chi-squares within the chi-squares at the best fit plus 3.53.

With the derived central values for ϕ_{th}, α, and γ as inputs, the ablation model of Equation 4.19 was used to predict cumulative fluence for each of the measured final structure heights. A comparison between the experimentally determined and model-predicted heights as a function of F_{cum} is given in the left and middle panels of Figure 4.5, each for a different material. The RMS differences between the data and the model are 12 and 9 J/mm^2 for alumina and sapphire, respectively, which

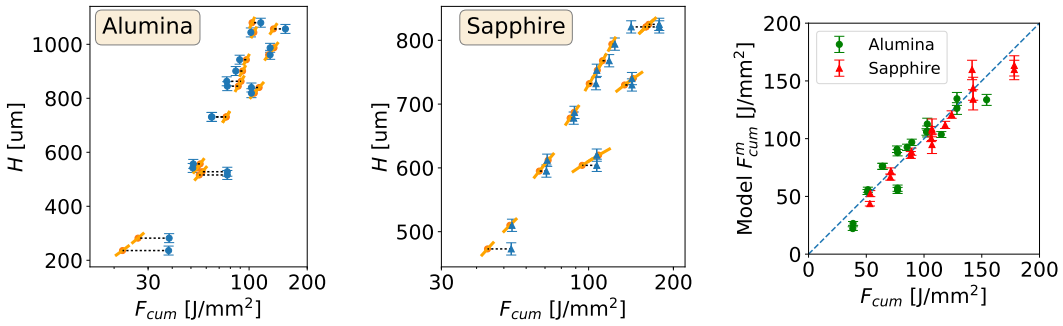

(a) (b) (c)

Figure 4.5: Model data points relating cumulative fluence and height (orange) and comparison to measured data (blue) for **(a)** alumina and **(b)** sapphire. Dotted lines connect pairs of experimental and model points that have the same height and peak fluence. Data error bars encode height uncertainties (see Section 3.4). The uncertainty in the calculated cumulative fluence is negligible. Model bars about the model central values indicate F_{cum} values needed to fabricate structures that correspond to the measured $H \pm 1\sigma$ values. The model gives a one-to-one relation between structure height and cumulative fluence, thus in **(c)** we plot the model-inferred cumulative fluence as a function of measured cumulative fluence for structures made on both materials. Data errors bars (horizontal axis) are negligible. Model error bars (vertical axis) are projections on the F_{cum} axis from the two left panels. The data fall near the expected slope of 1 (blue dash).

represent less than 10% variance over the 140 J/mm^2 fluence range of the data. An alternative display of the comparison between data and model is given in the right panel where we plot the model-predicted cumulative fluence F^m_{cum} for the measured height as a function of the experimental value.

4.2.2 Ablation Threshold and Absorption Length

Fitting the model for the ablation with the data, we find threshold fluence values near 2.0 J/cm^2 for both alumina and sapphire. Threshold fluence values for these materials reported elsewhere vary between 0.69 and 13 J/cm^2, and correspond to measurements over a range of wavelengths, pulse durations, repetition rates, and other parameters[1] [60, 79, 82, 85, 101–103]. Thresholds obtained with laser parameters that are similar to our work [60, 79, 85] give values between 0.97 J/cm^2 and 1.4 J/cm^2, which are within a factor of two of our results.

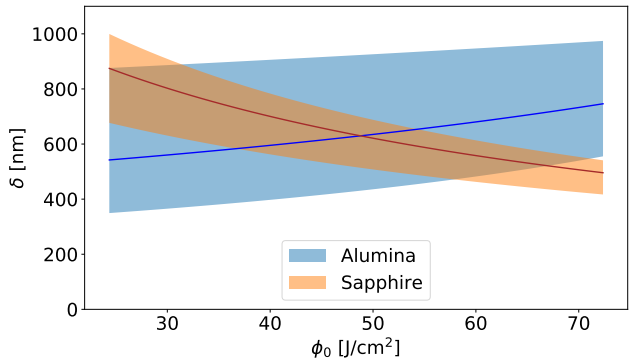

Figure 4.6: Absorption length as a function of incident peak fluence within the experimental range. The solid curves are calculated based on the best fits given in Table 4.1, while the shaded areas reflect the range of functions allowed given the quoted uncertainties.

[1]Threshold values were converted to peak fluence if the original results were reported in average fluence. In case of [101] it is not clear whether the fluence reported is peak or average.

The inferred absorption length δ as a function of fluence is shown in Figure 4.6. The uncertainty intervals encompass $\delta(\phi_0)$ functions that were determined using pairs of values α and γ within their common 68% uncertainty area; see Table 4.1. Within uncertainties the data for alumina is consistent with a constant $\delta \simeq 650$ nm, as well as with δ that mildly increases with fluence. Furmanski et al. [82] reported a constant value of 310 nm on alumina with fluence between 3 J/cm^2 and 37 J/cm^2. The data for sapphire are consistent with a decrease of δ with fluence. Boerner et al. [85] reported a constant $\delta = 118$ nm for sapphire with fluence between 4 J/cm^2 and 18 J/cm^2. When we fit our data to a constant absorption length $\delta = 1/\alpha$, the RMS difference in cumulative fluence between data and model increases by a factor of 1.1 and 1.3 to 13 J/mm^2 and 12 J/mm^2 for alumina and sapphire, respectively; the values for δ obtained are 770 and 500 µm for alumina and sapphire, respectively.

According to Stuart et al. [68], during avalanche ionization the absorption coefficient is proportional to the density of conduction-band electrons excited by the laser beam. Thus a decrease in absorption length with fluence may indicate an increase in production of conduction-band electrons. Alternatively, the observed decrease could be due to other effects not included in the model for the ablation rate such as plasma shielding [104] or debris formation [105], both of which can be important especially at high fluence and high repetition rate [104–106].

4.3 Average Ablation Rate

In Figure 4.7 we plot $\overline{V_a}(H)$ for different average laser powers P assuming the laser and scan parameters used for trials 1–8, $f_V = 1/2$, and w=70 and 82 µm for alumina and sapphire, respectively. For a given power $\overline{V_a}(H)$ increases to an optimal rate and then decreases as structure height H increases. This is because at the beginning of the ablation the projected peak fluence $\phi_{0,proj} = \phi_0 \cos(\alpha_{fl})$ is typically higher than the optimum peak fluence $e^2\phi_{th}$. The maximal instantaneous removal rate v_{rr} per unit power is only reached after the absorbed projected peak

fluence drops to the optimal value as structure height H increases. Material ablation terminates when the absorbed projected peak fluence drops below the threshold fluence. At given power, higher aspect-ratio structures, i.e. with higher H or smaller p, have lower $\overline{V_a}(H)$ due to smaller projected fluence and larger reflection. Higher laser power increases $\overline{V_a}(H)$ for alumina because the absorption length monotonically increases (see Figure 4.6), but higher power may decrease $\overline{V_a}(H)$ for sapphire, at least for a subset of H values, because absorption length decreases.

4.4 Discussion and Conclusion

The model presented and quantified through Equation 4.19 simplifies many complex details of the ablation process. Simplifications include ignoring heat diffusion and treating the interaction of each pulse with the material independently from the previous pulse; ignoring the interaction of the incident beam with the ablation plume; and ignoring the redeposition of debris. Even within the framework of the model, it is an approximation. When ablation in the grooves begins, the removed part resembles a trapezoid, not triangles; the possibly complex surface morphological changes are simplified to the progression of a simple geometrical structure; and we assumed an essentially infinite Rayleigh length. This last assumption is justified because the majority of the ablated material was within one Rayleigh length from the focus position, i.e. -0.75 mm $\pm$ 0.54 mm.

Yet, despite its relative simplicity, the model relates total height H to cumulative fluence with RMS of $\sim$10 J/mm^2 over a range near 150 J/mm^2 suggesting that it can provide reasonable guidance for future implementations. To compare, when we fit the data assuming vertical-cavity geometry, in which the flank angle $\alpha_{fl} = 90^\circ$ during the entire ablation process and the prefactor on the left hand side in Eq. 4.18 is 1, the RMS difference between data and model increases by a factor of 1.3 and 2.7 to 15 J/mm^2 and 24 J/mm^2, for alumina and sapphire, respectively.

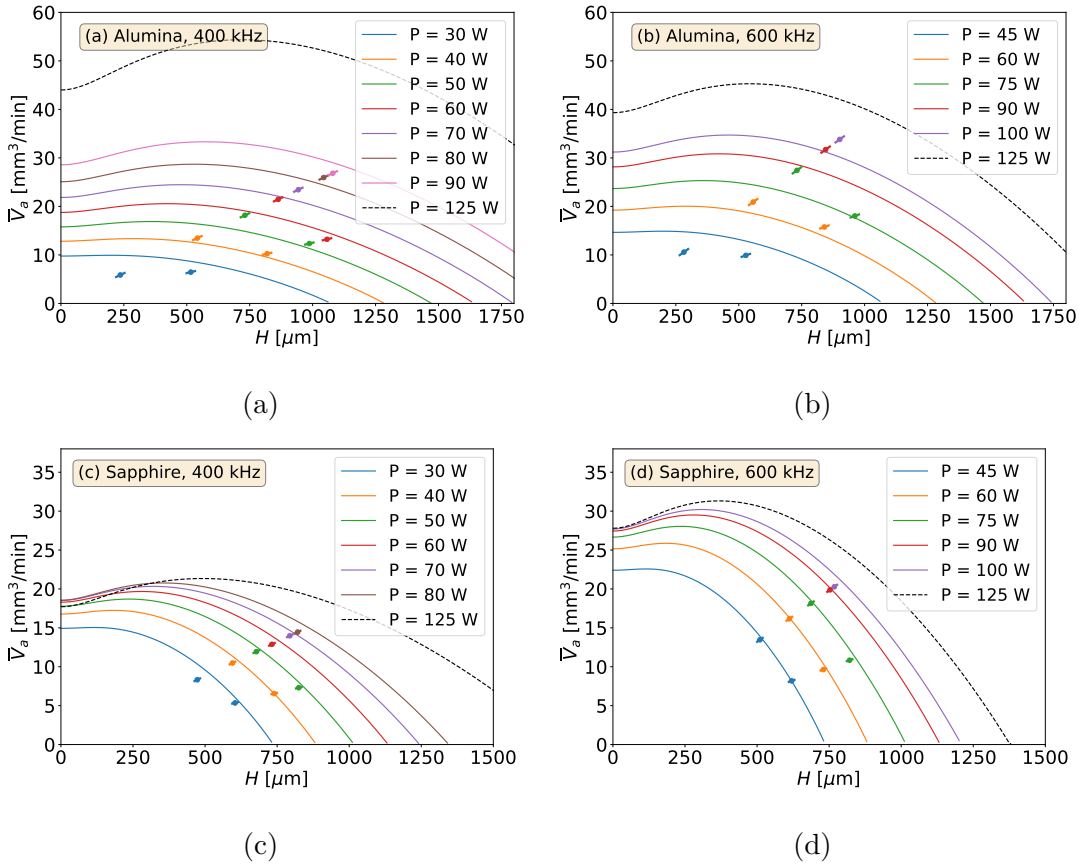

Figure 4.7: Average ablation rates as a function of the final structure height (lines) predicted based on Eq. 4.19 for different laser powers, and data (points) from trials 1–8. Bars near data points indicate the ranges of $\overline{V_a}$ predicted given the uncertainty in H. We include a line for $P = 125$ W (dash) to indicate the trend with further increase of power.

Further improvement in ablation rates for the purpose of making SWS ARC for large optical elements in the millimeter and sub-millimeter wave band require direct measurements of the absorption length δ and the values of ϕ_{th} for the relevant materials, and verification of the ablation model using a range of fluence values, power levels, and geometries. With constant laser power, further increases in volume removal rate may also be achievable by varying the z position of the beam focus as ablation progresses and by better optimizing the scan.

In conclusion, we extended a model for the ablation and compared it with the measured data in Section 3.4. We found that despite significant simplifications, the model provides reasonable guidance for the relation between structure height and required cumulative fluence. Over a range of 140 J/mm^2 in cumulative fluence the RMS differences between the data and the model are 12 and 9 J/mm^2 for alumina and sapphire, respectively. The best fit values (Table 4.1) for the absorption length δ, which are in the range of few hundreds of nm, and for threshold fluence ϕ_{th} are comparable with values reported in other publications.

The model indicates that a primary reason for the higher ablation rates is the increase in laser power. Further optimizations of the ablation process are feasible and thus achieving ablation rates of tens of mm^3/min is possible when fabricating structures with heights of $\sim$1 mm.

Chapter 5

Probe of Inflation and Cosmic Origins (PICO)

The Probe of Inflation and Cosmic Origins (PICO) [107] is a proposed probe-scale space mission consisting of an imaging polarimeter that will orbit around the Earth-Sun L2 Lagrange point, and will scan the sky for 5 years in 21 frequency bands from 21 to 799 GHz. It will produce full-sky surveys of intensity and polarization with a final combined map noise level equivalent to 3300 Planck missions [108] for the baseline required specifications, and according to the current best-estimate would perform as 6400 Planck missions.

PICO was selected by NASA to conduct a probe mission study that was open to the entire mm/sub-mm community, as part of the preparations for Astro2020 Decadal Survey [109]. The study was initiated in the summer of 2017, and the final report [107] was submitted by the study team to NASA in the beginning of 2019. There were seven working groups within the study team, and during the entire study period the author was serving in the Imager Options group, which was tasked to set specifications for the imager including optical system, frequency bands, and focal plane architecture.

This chapter discusses two PICO study projects in which the author made major contributions: 1. cross-Dragone as a candidate optical design; 2. mechanical

design and mass estimation of the PICO focal plane.

5.1 Cross-Dragone Optical System for PICO

The telescope design is driven by a combination of science requirements and the physical limits. For PICO, the science requirements include a large diffraction-limited field of view (DLFOV) that is large enough to house around 10 K detectors. We define DLFOV as an area where Strehl ratio is larger than 0.8 so that optical quality is not a limit but diffraction is. PICO also requires arcminute resolution at 800 GHz, low instrumental polarization, and low sidelobe response. These requirements are challenging for a space mission, whose physical size is limited because of various constraints that are discussed in Section 5.1.1.

We concentrated our investigation on reflective Dragone optical systems, which satisfy several conditions proposed and analyzed by Dragone [110–112]. A Dragone system has no cross-polarization at the center of the field of view, and has astigmatism, or astigmatism and coma canceled to first order. We compared two categories of Dragone systems, namely "open-Dragone" and "cross-Dragone", in terms of DLFOV, compactness, and rejection of sidelobes. Figure 5.1 shows one representative example for each category: an open-Dragone design that was eventually chosen as the PICO optical system, and a cross-Dragone design that reproduced the optical system of EPIC-IM [113, 114], a NASA mission concept proposed around year 2009 for probing inflation. A major visual difference that separates a cross-Dragone system and an open-Dragone system is whether the optical rays between the secondary mirror and the focal plane cross over the rays coming from the sky to the primary mirror. Note that F-number is the ratio of the system's focal length to the diameter of the aperture stop D.

A cross-Dragone system has roughly $\times 3$ the DLFOV of a open-Dragone with the same F-number. We calculated and compared the DLFOV of the cross-Dragone system shown in Figure 5.1 and the DLFOV of an open-Dragone system that was an earlier version of the one shown in Figure 5.1 at several different

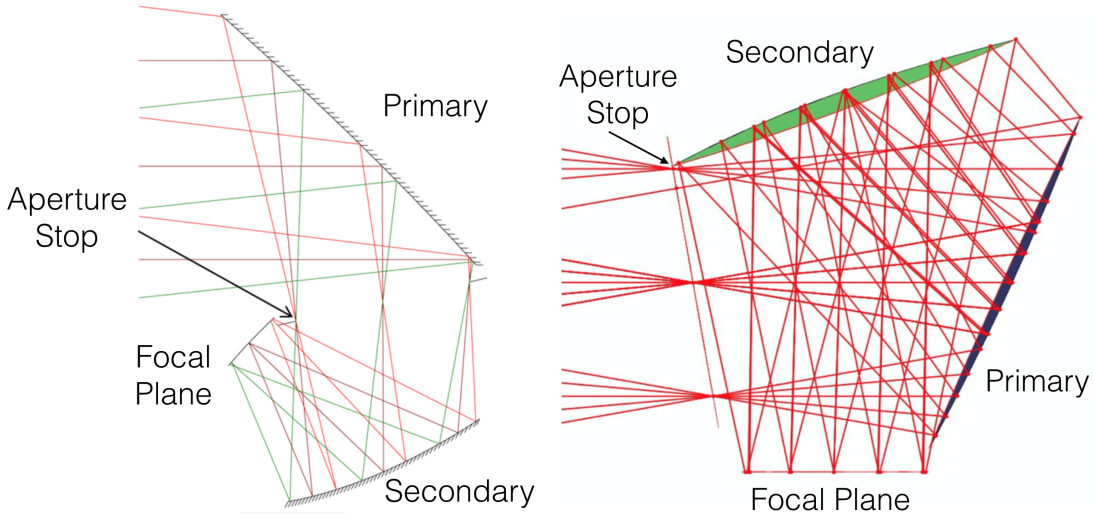

(a) (b)

Figure 5.1: (a) PICO open-Dragone system [115], F-number= 1.42, $D = 1.4$ m ; a cross-Dragone system that reproduced the EPIC-IM design, F-number= 2.14, $D = 1.4$ m.

frequencies. The results are shown in Table 5.1 in the unit of $F\lambda$, where F is the F-number and λ is the wavelength. $F\lambda$ is a proper unit to quantify DLFOV because the detector sizes are optimized such that they are proportional to the $F\lambda$; larger F-number requires larger detectors. Therefore, we concluded that a cross-Dragone provided roughly $\times 3$ the DLFOV of an open-Dragone in terms of the overall area. In addition, I made another similar comparison between a cross-Dragone and an open Dragone that had both $F = 3$; the results are shown in Table 5.2 in the unit of centimeter since F-number is same; the same conclusion was supported.

Despite of having larger DLFOV than open-Dragone system, cross-Dragone system was found to be more difficult to pack inside the spacecraft volume defined in Section 5.1.1 while avoiding the known sidelobes discussed in Section 5.1.2. A design solution of cross-Dragone system that I developed successfully avoided the known sidelobe issues, and could be packed into the allowed space while having

	Cross-Dragone		Open-Dragone		
Freq [GHz]	DLFOV X	DLFOV Y	DLFOV X	DLFOV Y	Area ratio
70	106.7	85.8	62.8	56.5	2.58
100	120.3	115.4	68.7	62.9	3.21
150	134.1	124.6	73.3	69.2	3.29
220	145.1	132.0	76.4	74.3	3.37
350	153.0	135.7	78.3	78.3	3.39
500	152.8	132.5	78.7	79.9	3.22

Table 5.1: Comparisons of the DLFOV sizes in the unit of $[F\lambda]$ between the reproduced EPIC-IM cross-Dragone system shown in Figure 5.1 and an earlier version (unoptimized) of PICO open-Dragone system; both systems had aperture $D = 1.4$ m. In Figure 5.1, X is the direction into and out of the page and Y is the direction parallel to the focal plane. The area ratio was calculated assuming the DLFOV contours were elliptical.

	Cross-Dragone		Open-Dragone		
Freq [GHz]	DLFOV X	DLFOV Y	DLFOV X	DLFOV Y	Area ratio
70	177	162	107	83	3.23
150	108	107	72	57	2.82
350	65	64	44	36	2.63

Table 5.2: Comparisons of the DLFOV sizes in the unit of [cm] between a cross-Dragone system and an open-Dragone system with the same $F = 3$ and $D = 1.4$ m.

a 1.2 m aperture to provide required angular resolutions. However, compared to the baseline open-Dragone system that had a 1.4 m aperture and a F-number of 1.4, this cross-Dragone design supported smaller number of detectors because of a larger F-number of 2.5 and as a result provided worse sensitivity performance. This cross-Dragone design is discussed in Section 5.1.3.

All the optical systems discussed in this section were built in CodeV, a ray-tracing software [116].

5.1.1 Physical Limits for A Space Mission

For any space telescope, the design should consider the physical limits coming from its launching vehicle and the Sun illumination. PICO is assumed to be launched by SpaceX's Falcon 9 [117], which allows a maximum diameter of the PICO spacecraft to be 4.6 m; see panel (a) of Figure 5.2 for Falcon 9's payload constraints. Deployable shields are opted to be not used for PICO as they present added cost and risk which outweighs the benefits. This diameter of 4.6 m limits the sun shields' size, which, along with the angle α determined by scan strategy, defines the 'shadow cone' shown in panel (b) of Figure 5.2. The shadow cone is the volume protected from solar illumination, and all optical components are contained within it.

The α is the angle between the spacecraft spin axis and anti-solar direction, while the β is the angle between the spacecraft spin axis and telescope's boresight. The β sets an additional constraint on how we fit a telescope design into the shadow cone. The choices of α and β are determined by scan strategy.

PICO uses a type of full-sky scan strategy that has been adopted by other missions such as Planck [108] and CORE [118]. Panel (c) of Figure 5.2 provides a nice illustration of this scan strategy. Spacecraft spins around its spin axis while the spin axis precesses around the L2 point about the anti-solar direction with an angle of α. The spin enables the telescope's boresight to form a ring on the sky and the precession enlarges the width of the ring. Combining with the rotation of the

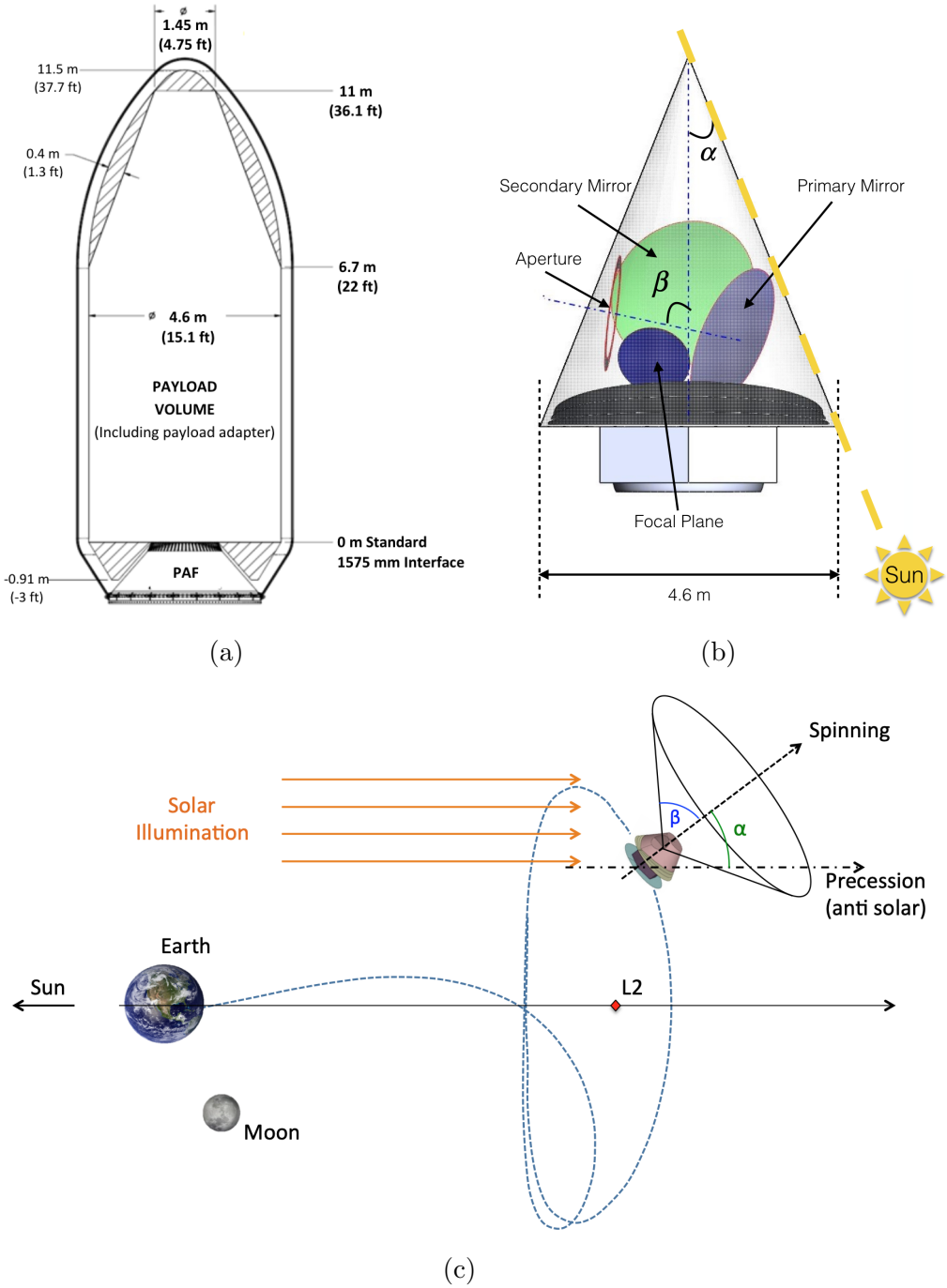

Figure 5.2: (a) SpaceX's Falcon9 fairing and payload dynamic envelope; units in meters (feet) [117]. (b) Illustration of fitting a cross-Dragone system into the shadow cone. (c) Illustration of a space telescope that scans full sky by precessing around L2 and spinning; picture credited to CORE mission design paper [118].

Earth around the Sun, this scan strategy enables full-sky coverage if $\alpha + \beta > 90$ deg. If $\alpha + \beta < 90$ deg, the scan leaves two empty holes around the Ecliptic poles. Without precession, the only way in theory to achieve full-sky coverage without active attitude control would be letting $\alpha = 0$ deg and $\beta = 90$ deg, which would result in a terrible non-uniform scan coverage; any points on the sky other than the Ecliptic poles get scanned only twice a year.

During the PICO study phase, we initially assumed α to be 22 degrees and conducted all the studies discussed in this chapter based on this assumption. To clarify, the final PICO design has $\alpha = 26$ deg after further optimization. For reference, Planck had an α of 7.5 degrees, but PICO chooses to have substantially larger α to mitigate systematic effects by scanning across each sky pixel with a greater diversity of orientations. The β was assumed to be such that $\beta = 95^\circ - \alpha$.

5.1.2 Sidelobes for Cross-Dragone System

Cross-Dragone systems are known to have two major sources of sidelobes: direct view to sky and multiple reflection. In Figure 5.3, the blue arrow indicates a direct coupling path between light sources on the sky and detectors on the focal plane, while following the multi-reflection path illustrated by the green arrows we find another coupling path. Each detector on a focal plane is designed to detect photons emitting from one particular angular direction on sky. For example, the detector at the center of the focal plane observe at the boresight direction. The light coming from bright astronomical sources into the detectors along these sidelobe paths confuse detectors.

Increasing F-number and/or adding baffles help mitigate the sidelobes for cross-Dragone systems; see for example LiteBIRD's case [119]. However, both of these methods would increase the overall size of the optical system. Figure 5.4 demonstrates how the size of cross-Dragone system changes with increasing F-number while keeping the aperture size fixed at $D = 1.4$ m. Given the fact that fitting a $F = 2.14$, $D = 1.4$ m cross-Dragone was already very hard, as shown in

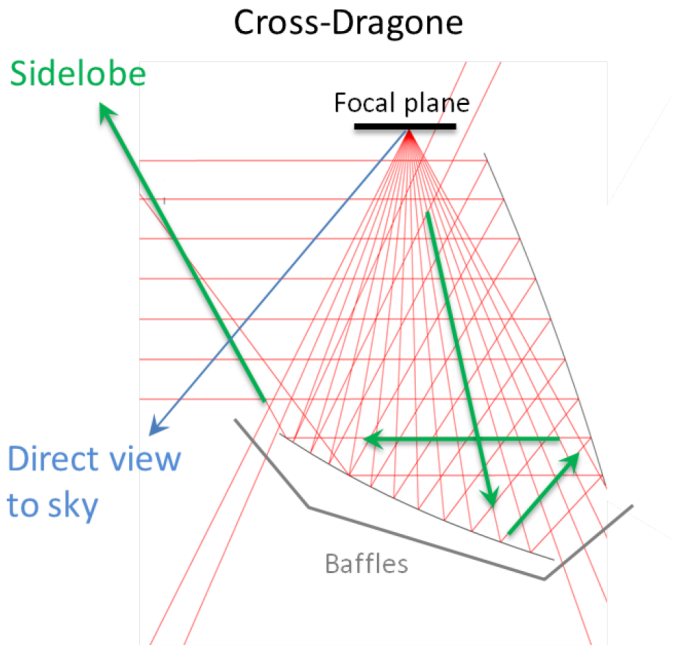

Figure 5.3: Sidelobe analysis for cross-Dragone system. Rays were traced from the center of the focal plane toward the sky. The designed correct path is focal plane (top), secondary mirror (bottom), primary mirror (right) and sky (left).

the panel (b) of Figure 5.2, it was clear that there was not much room to increase F-number while maintaining the same aperture size.

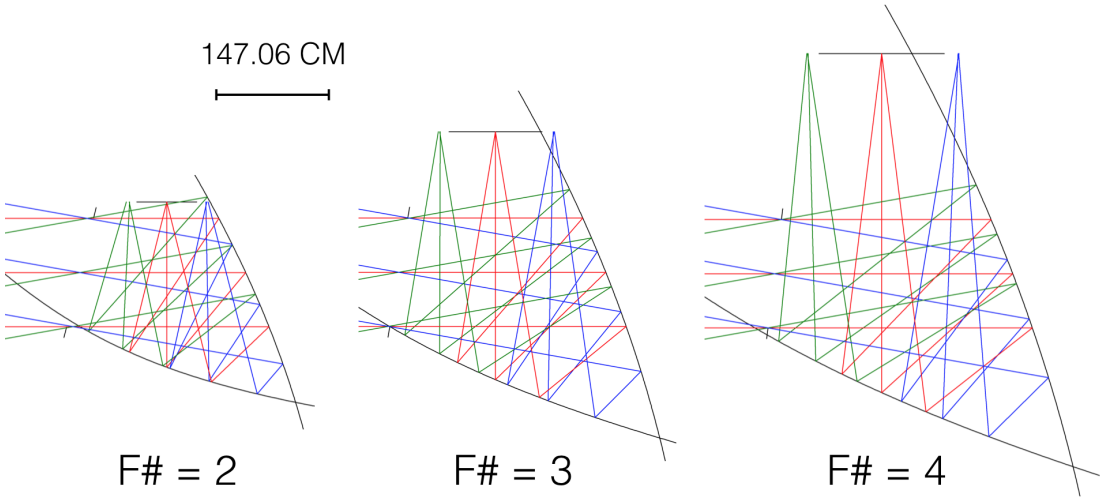

Figure 5.4: Cross-dragone designs with the same aperture stop diameter $D = 140$ cm but with different F-numbers.

We tried to add a third folding mirror to reposition the focal plane in order to provide more compactness, which was a proposed solution for CORE mission [118]. Figure 5.5 shows such a design with $F = 3$, $D = 1.4$ m that I made with necessary baffles added; it avoided the sidelobes discussed above and it was able to fit within the shadow cone. However, there was concern about the possible existence of other multi-reflection paths that could result in other sidelobes.

The standard method to investigate such an issue is running nonsequential stray-light analysis; see example of a study for Simons Observatory [120]. Due to the time limit, I came up with an alternative method that successfully provided an answer in a very short time. I imported the optical system from CodeV into SolidWorks, and I rendered the 3D model such that the mirrors are reflective, as shown in Figure 5.6. It turned out that the concern was valid and in fact there was a direct coupling path along the focal plane, the folding mirror and sky.

We concluded that having a third folding mirror was risky and decided to

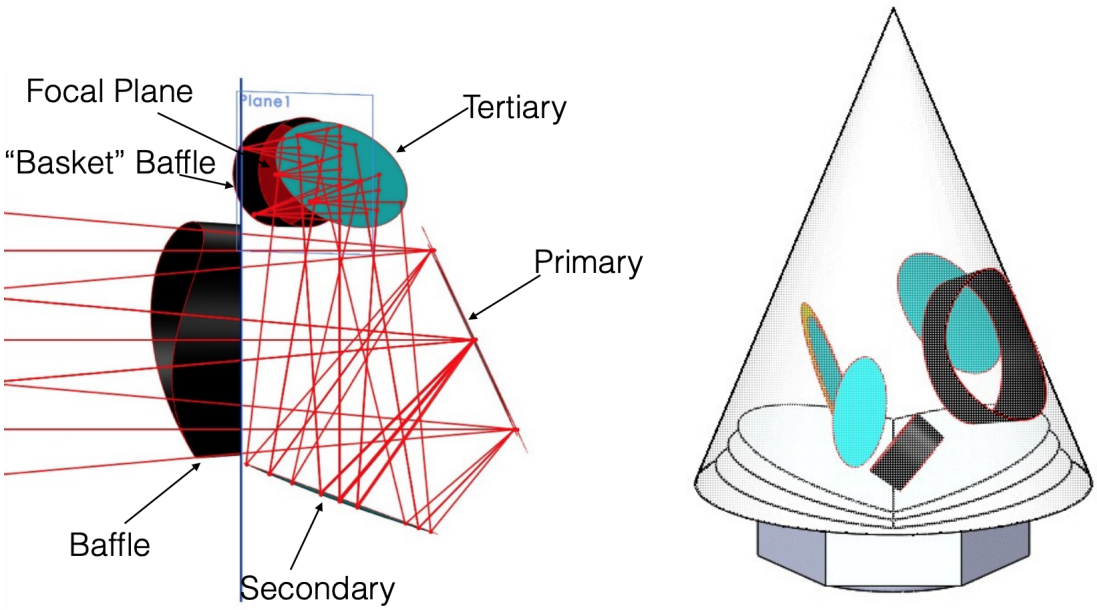

(a) (b)

Figure 5.5: (a) A folded cross-Dragone system. The cyan "Tertiary" mirror is the added folding mirror and it redirects the light to the focal plane, which is in red and surrounded by a "Basket" baffle. (b) Shadow cone fitting.

continue looking for solutions based on 2-mirror cross-Dragone system, while considering reducing the requirement on the aperture size from 1.4 m to smaller values.

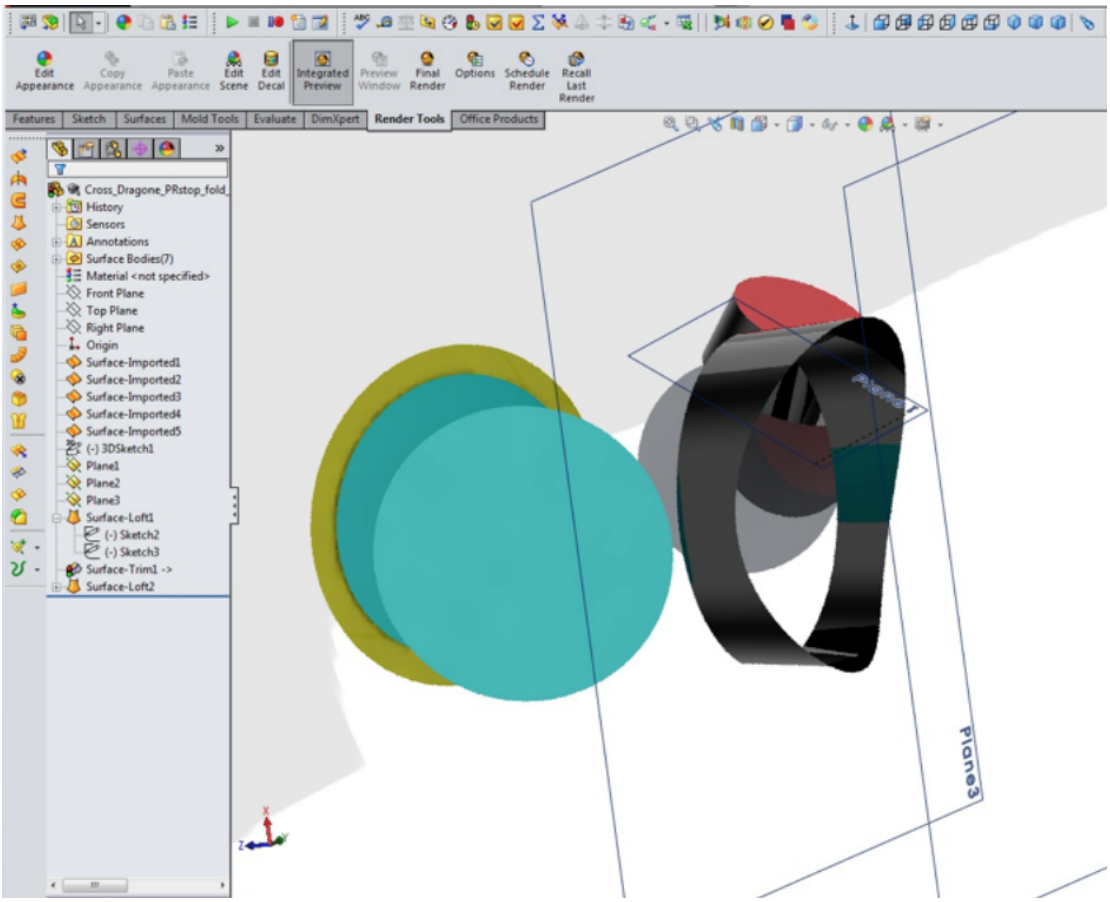

Figure 5.6: SolidWorks reflective rendering of the folded cross-Dragone system shown in Figure 5.5. The aperture stop is on the "Plane3" and the black material on the front right is the baffle around the aperture stop. Seeing though the aperture stop, the gray mirror shows the reflection of the "insdie" of the red focal plane.

5.1.3 A Candidate Design

After several rounds of trial-and-error attempts, I obtained a design of cross-Dragone system with $F = 2.5$ and $D = 1.2$ m that satisfied the requirements; the design is shown in Figure 5.7. A sidelobe analysis similar to the one shown in Figure 5.3 had been conducted and no sidelobe was found.

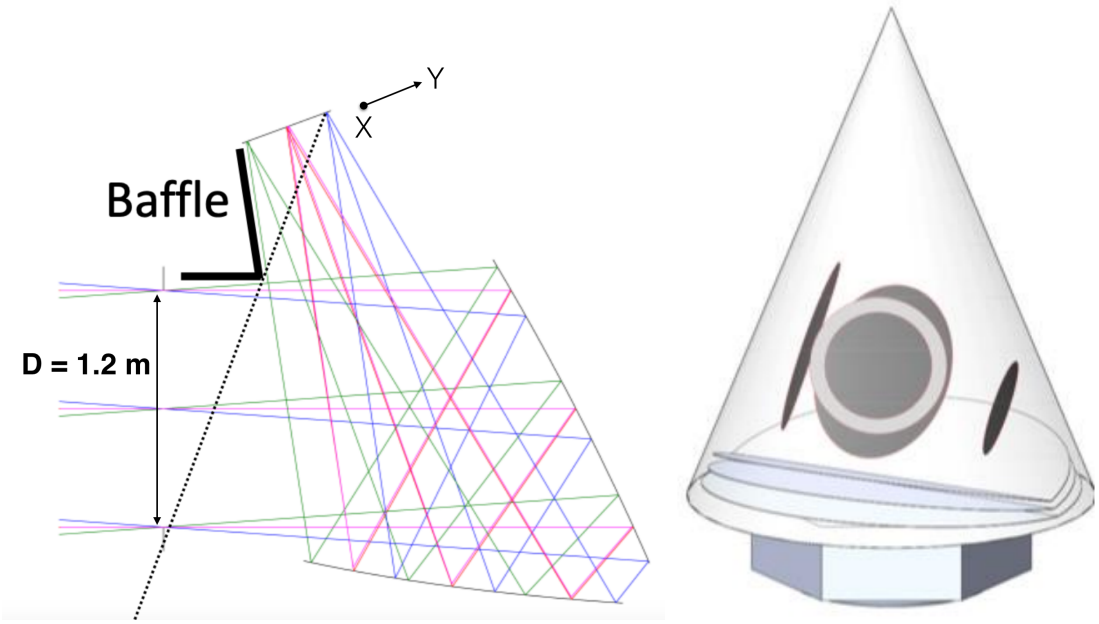

(a) (b)

Figure 5.7: Final design of the cross-Dragone system for PICO, F-number is 2.5, aperture is 1.2 m, FOV= ±4 deg in Y and FOV= ±10 deg in X. Direct view is blocked by the baffle shown in the figure. It fits well within the shadow cone.

We compared the physical sizes between this cross-Dragone system and the baseline open-Dragone system; the results are summarized in Table 5.3. One advantage of this cross-Dragone design is that it requires smaller primary mirror than the baseline design, which positively affected the weight control. The physical size of the focal plane is roughly 50% larger than that of the baseline open-Dragone.

Despite of having a larger focal plane, this candidate cross-Dragone design

	Baseline Open-Dragone [cm]		1.2 m Cross-Dragone [cm]	
Aperture	Y	140	Y	120
	X	140	X	120
Primary Mirror	Y	270	Y	167
	X	190	X	180
Secondary Mirror	Y	140	Y	160
	X	140	X	176
Focal Plane	Y	50	Y	45
	X	55	X	90

Table 5.3: Comparisons of the physical sizes between the cross-Dragone candidate design and the baseline open-Dragone design. The X direction is in-and-out of the page in Figure 5.7, while Y direction has a non-fixed definition depending on the optical element and is roughly aligned parallel to each element.

turned out to support less detectors than the baseline open-Dragone design. We estimated that this cross-Dragone could support around 3,500 detectors and mostly likely more if further optimized, while the baseline design supports 13 K detectors. The main reason is that the detector pixel sizes are proportional to the F-number, and the occupation area of each detector pixel is therefore proportional to F-number squared. The larger F-number of the cross-Dragone, i.e. $F = 2.5$ vs $F = 1.4$ of the baseline open-Dragone, results in larger pixels and eventually less detector counts.

We concluded that the baseline open-Dragone system was a better choice than the cross-Dragone design. Compared to the cross-Dragone system introduced in this section, the baseline open-Dragone design has larger number of detectors that leads to better sensitivity, and has lower weight from the focal plane since the physical size is smaller than that of the cross-Dragone.

5.2 Mechanical Design of Focal Plane

We were tasked to provide a mechanical design of the PICO's focal plane, given the optical layout shown in Figure 5.8. Modules with the same color, except for the

purple one near the center, host identical three-frequency sinuous antenna/lenslet pixels for PICO's 21-462 GHz bands. The purple rhombus module near the center hosts three different single-frequency horn-coupling pixels for PICO's highest frequency channels 555, 666, 799 GHz. For more details about the optics and pixel distribution, see Young et al. [115].

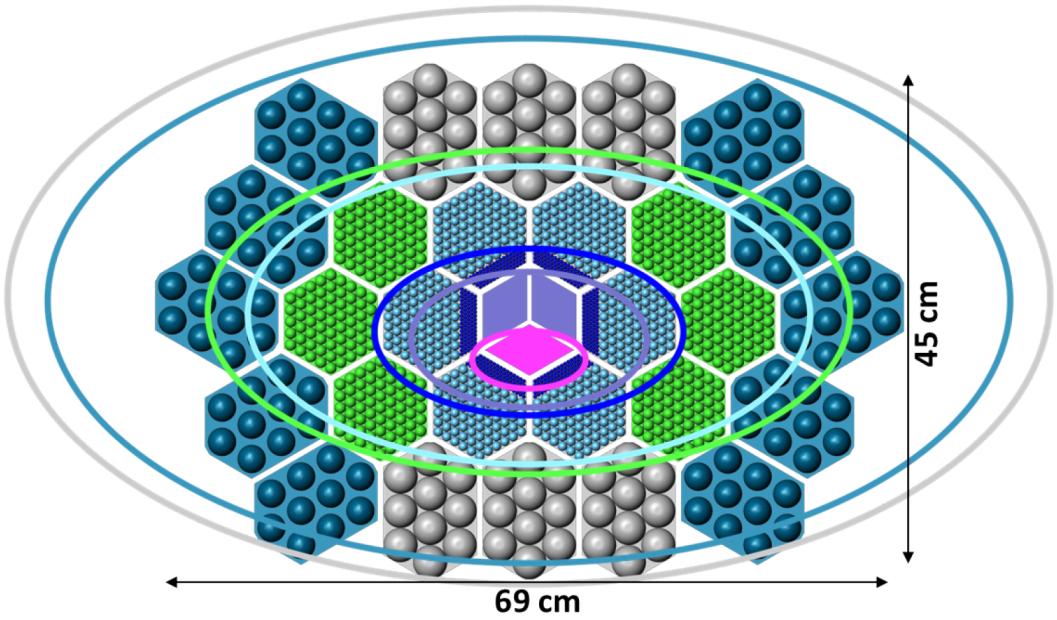

Figure 5.8: Optical layout of PICO focal plane, with Strehl = 0.8 contours for each pixel type [115].

PICO's focal plane is planned to be actively cooled to 0.1 K. There were several goals of designing a mechanical model for PICO's focal plane:

- Finding a mounting solution.
- Figuring out physical configuration of detector modules that enables integration of time-domain multiplexer (TDM) readout wafers and detector wafers.
- Providing heat sink between mounting frame and detector arrays.
- Estimating the total weight of the focal plane.

5.2.1 Detector Modules

For all modules, indium bump bonding was chosen as the bonding strategy to electrically connect the detectors to the underneath TDM wafers. Compared to wire bonding, indium bump bonding does not require bond pads at the edge of detector wafers. This is especially advantageous when the numbers of detectors per wafer are high and spare edge areas are limited on the detector wafers, which is the case for PICO detector modules.

It turned out that the indium bumps were able to provide enough heat sinking power for the detector arrays. We decided to heat sink the TDM wafers to the mounting frame, and heat sink the detector wafers to the TDM wafers using indium bumps. I estimated that all the indium bumps together could provide over 20 μW heat sinking power at 0.1 K between the TDM wafers and detector wafers given a temperature difference of 10 mK between the two. To make such an estimation, one needs to calculate the thermal conductance, which is equal to kA/L, where k is the thermal conductivity, A is the area and L is thickness. I assumed that each indium bump was a cylinder with 20 μm in diameter and 10 μm in height. Given roughly 26 K indium bumps, the total area $A \approx 4.7$ cm^2. Assuming a backshort layer in between, two layers of bump bonding gave $L =$ 20 μm. As far as the conductivity of Indium at 0.1 K was concerned, there was no measured data available in literature. I extrapolated from measure data at higher temperatures [121] to 0.1 K and obtained a value of 9.9E-7 W cm^{-1} K^{-1}. Indium is superconducting below 3 K, and my extrapolation followed an empirical temperature dependence for superconducting indium found in [122].

Given the theme of using indium bump bonding, we were to design physical configuration for each pixel type.

For the highest-frequency module (purple one in Figure 5.8), the design process was straightforward. The dimensions to be determined are shown in the panel (a) of Figure 5.9: horn aperture d, horn length L, waveguide width b and waveguide length t. For each band, the high-pass waveguides define the lowest band frequency ν_{low}, while metal-mesh filter defines the highest frequency ν_{high}. We assumed

$d = 3.108w_0$, where w_0 is the beam waist; $L = 4 \times 0.3 \times d^2/\lambda$, reaching the maximum effective area of a conical horn [123]; $b = 1.84\pi c/\nu_{low}$, where ν_{low} is the lowest frequency in a band; $t > 4\lambda$, so that the waves below the cutoff frequencies decay exponentially to almost 0. The results are summarized in Table 5.4 and the design is shown in the panel (b) of Figure 5.9. The material was assumed to be silicon, with metal-coated feed horns.

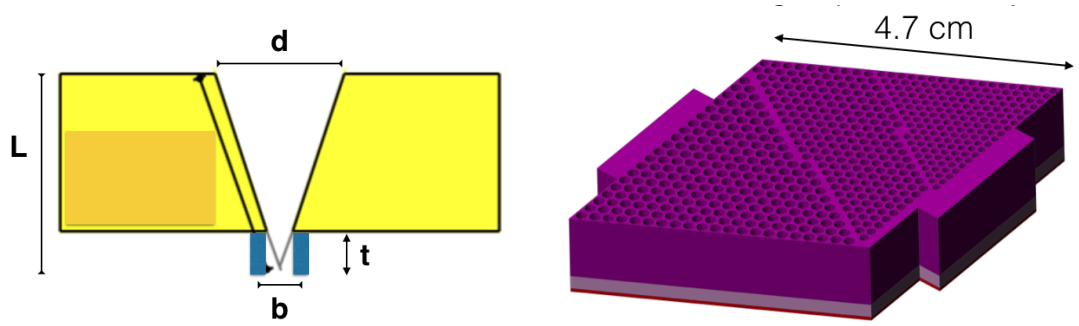

(a) (b)

Figure 5.9: (a) Dimensions for a feed horn. (b) The silicon detector module of the highest frequency channels 555, 666, 799 GHz, with conical horns and waveguides.

Freq [GHz]	d [mm]	L [mm]	b [mm]	t [mm]
555	1.69	11.8	0.36	2.5
666	1.41	11.8	0.30	2.5
799	1.18	11.8	0.25	2.5

Table 5.4: Designed dimensions for the feed horns on the purple module. The definitions of letters are given in the panel (a) of Figure 5.9.

For the other lenslet modules at lower frequencies, they followed a same stacking configuration shown in Figure 5.10. The length of the lenslet wafer extension L was calculated using $L/R = 0.46$ [124]. A backshort attenuation layer was required in between the detector wafer and TDM wafer, to control the backlobe. Inspired by Staguhn et al. [125], we came up with an idea using through-wafer vias and non-resonance metal-plated cavity. The attenuation of the GHz waves

was achieved by cavity with impedance matching, while through-wafer vias connected the detector wafer and TDM wafer. The backshort/bonding layer was assumed to be $\lambda/5$ thick, where λ was the wavelength of the central band in each three-frequency pixel.

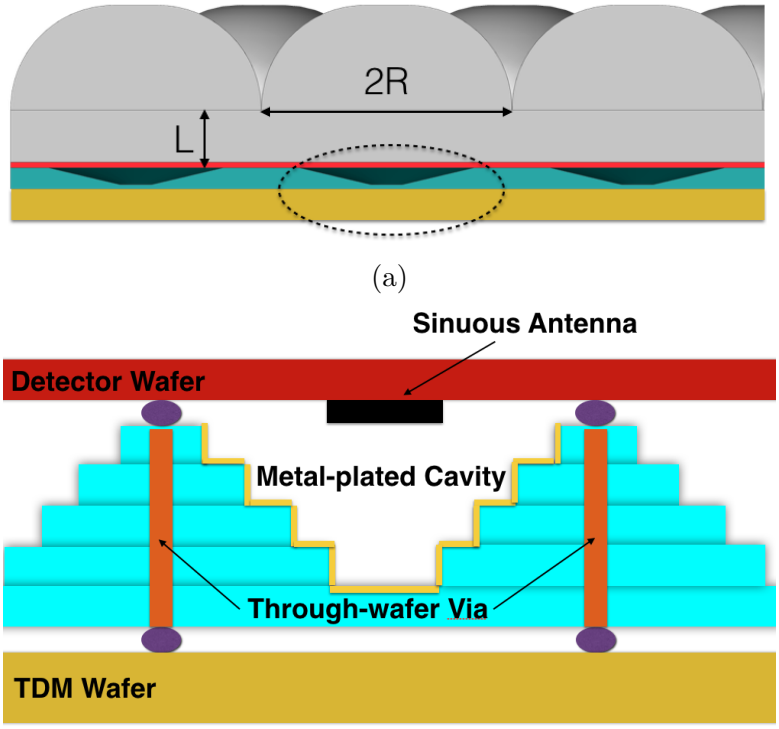

Figure 5.10: (a) All-silicon based lenslet module stack: (from top to bottom) lenslet wafer (grey), detector wafer (red), backshort/bonding wafer (cyan), TDM wafer (yellow). (b) A zoom-in of the dashed circle in panel (a) to show the backshort/bonding configuration.

5.2.2 Clamping-down Mounting Frame

We adopted a "clamping-down" strategy for designing the mounting frame, similar to some other experiments using lenslet modules [126, 127]. Figure 5.11 shows the implementation. We added at least three side extensions on each module, as shown

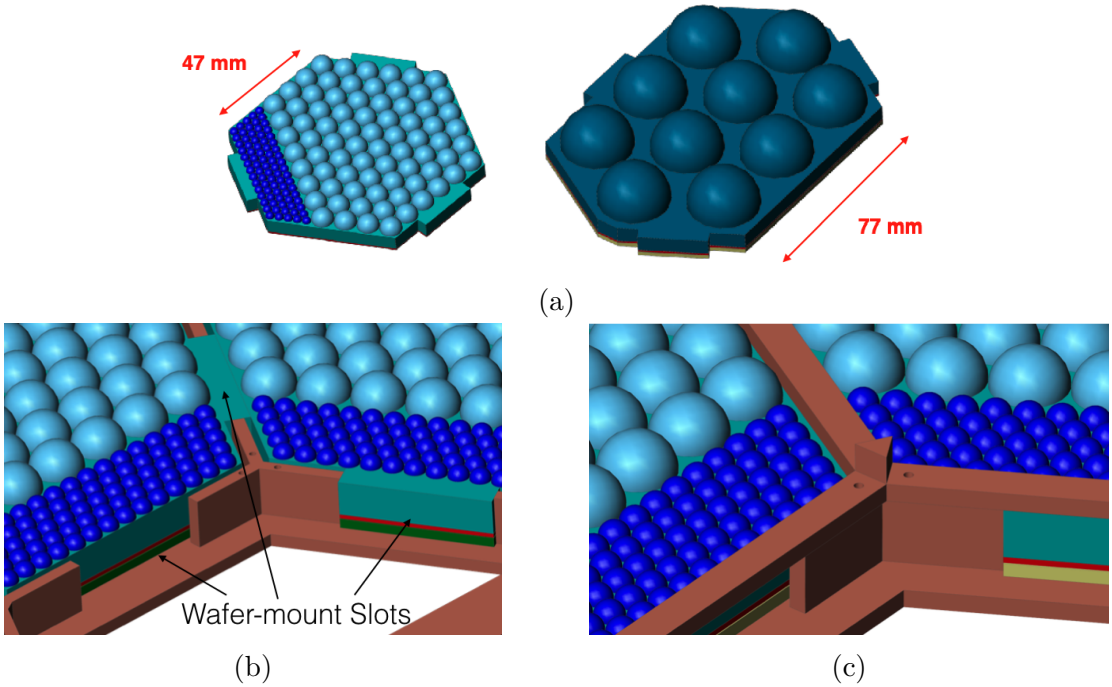

Figure 5.11: (a) Examples of lenslets wafers with extensions; left: Wafer of pixel D (75/108/155 GHz), E (186/268/385 GHz); right: wafer of pixel B (25/36/52 GHz). (b) Wafers sit on the bottom frame. (c) Top frame is clamped down.

in the panel (a); the extrusion length is 4 mm to fill the gap between neighboring wafers. We let the extensions sit in the wafer-mount slots on the "bottom frame" and then clamp down the "top frame" to press on the extensions, as shown in the panel (b) and (c).

Bottom frame and top frame were assumed to use copper or invar as the base material to machine. Invar has larger specific heat than copper (0.97 vs 0.01 J kg^{-1} K^{-1}) [128]. Each frame would be machined from a single bulk for the entire focal plane. The thickness of the copper/invar was assumed to be 80 mils or 2 mm, which we believed is strong enough; more careful engineering investigation was beyond the scope of the study. Differential thermal contractions were considered since the focal plane would operate below 1 K. The relative linear expansion coefficient between 300K and 4K is -0.33% for copper and -0.05% for invar [128], while it is about -0.02% for silicon. We left enough space between silicon lenslet modules and frame walls to avoid any damage to the modules due to thermal contractions, as shown in panel (b) of Figure 5.11.

The overall mechanical design of PICO focal plane is shown in Figure 5.12. Note that we aligned the detector modules to the top frame, not to the bottom frame, such that the tops of all lenslets are on the optical focal plane in the optical design [115]. Since different modules have different overall thicknesses as discussed earlier, the distances between different modules and the bottom plate are not the same, as shown in the panel (b).

Each module was assumed to have a metal-mesh low-pass filter on top of it. To determine the thickness required at different frequencies, I measured the EBEX metal-mesh filters and fit the data between the thickness and the frequency with a power-law function, as shown in Figure 5.13. I calculated the thickness of each filter using this formula at the highest band of each three-frequency pixel type. .

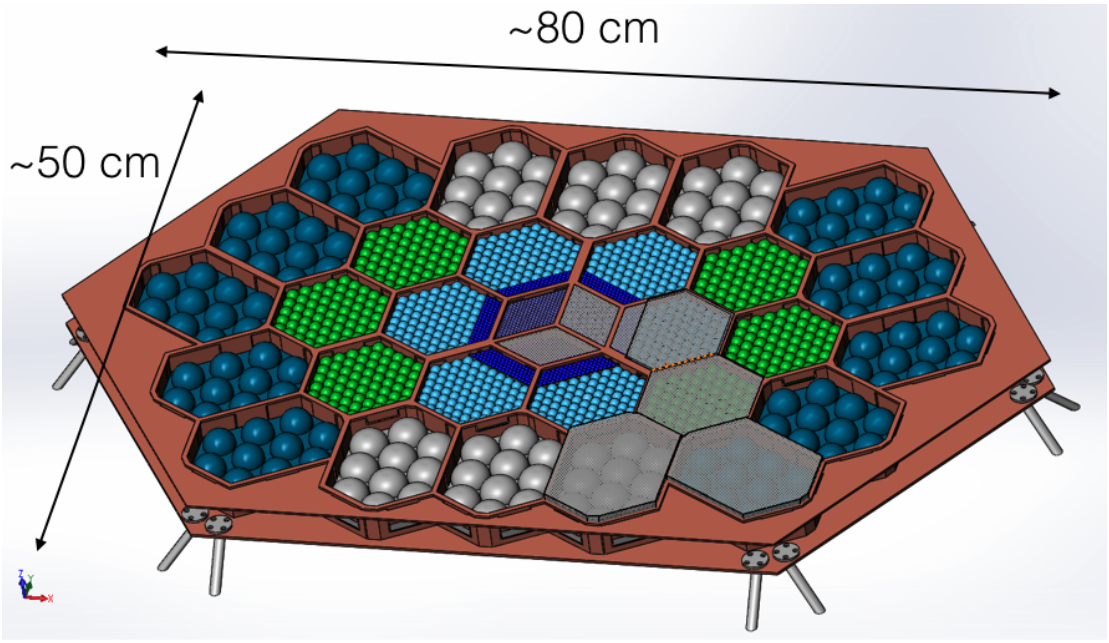

(a)

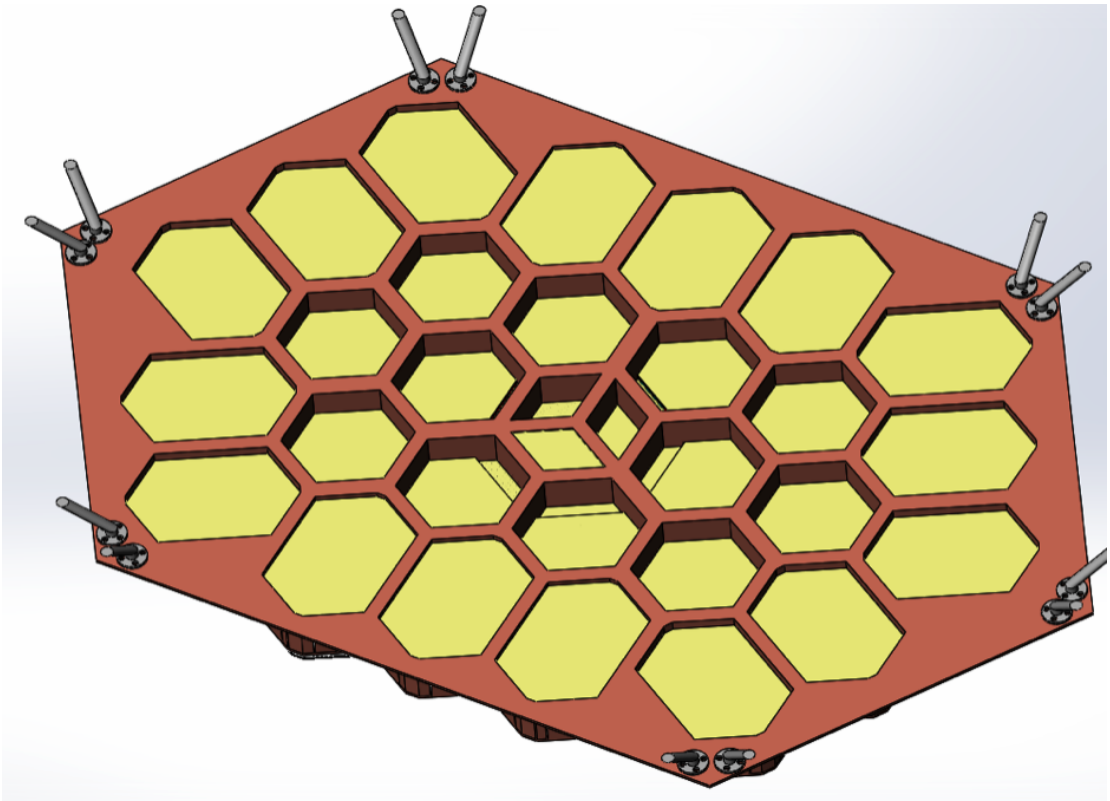

(b)

Figure 5.12: Top (a) and bottom (b) views of the PICO focal plane. Some example metal-mesh low-pass filters (grey transparent plates) sit on the top frame for illustration purpose.

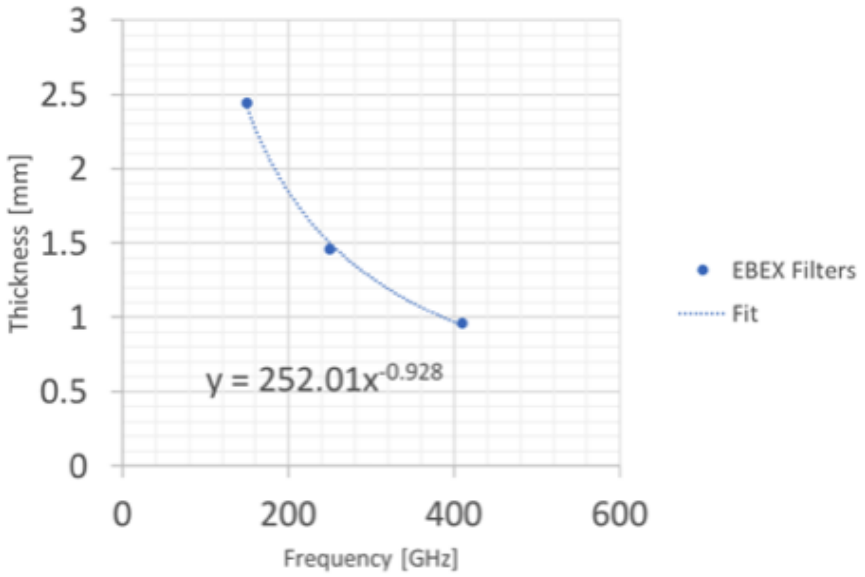

Figure 5.13: Metal-mesh filters' thickness vs frequency based on EBEX filters.

5.2.3 Weight Estimation

With the 3D model shown in Figure 5.12 built in SolidWorks, we were able to estimate the masses of all components. I assumed the densities: $\rho_{copper} = 8.9 \times 10^3$ kg/m^3, $\rho_{invar} = 8.1 \times 10^3$ kg/m^3, $\rho_{silicon} = 2.33 \times 10^3$ kg/m^3. The density of the EBEX metal mesh filters were measured to be 0.91×10^3 kg/m^3. The results are shown in Table 5.5.

Component	Weight [kg]
Mounting frame (cover/invar)	10.06/9.15
Lenslet/feed-horn wafers + detector wafers (silicon)	5.05
TDM wafers (silicon, 2mm thick)	0.95
Backshort/bonding wafers (silicon)	0.12
Metal-mesh filters (1 layer)	0.98
Total (cover/invar)	17.16/16.25

Table 5.5: Designed dimensions for the feed horns on the purple module. The definitions of letters are given in the panel (a) of Figure 5.9.

Chapter 6

One Large Aperture vs. Multiple Small Apertures for a Balloon-borne Instrument

Compared to a telescope with same optical design but smaller aperture (and thus smaller overall physical size), a telescope with larger aperture provides better angular resolution, and enables higher sensitivity because of the larger number of detectors it can support. Nevertheless, for an instrument to be designed, if the angular resolution is not a limit and the sensitivity is the primary design driver, it is interesting to compare two options: one large-aperture telescope vs. multiple small-aperture telescopes within the instrument.

Tau Surveyor is a proposed balloon-borne instrument that we designed to constrain the optical depth to reionzation τ with an estimated precession of $\sigma(\tau) \leq 0.0035$ (currently $\sigma(\tau) = 0.006$ [129]), and to provide a definitive larger than 3σ measurement of the absolute mass scale of the neutrinos ($\sigma\left(\sum m_\nu\right) = 17$ meV vs. currently $\sigma\left(\sum m_\nu\right) > 50$ meV [130]). These constraints are enabled primarily by measuring the E-mode polarization of the CMB over large angular scales, or multipole moment $\ell \leq 20$ in terms of the spherical multiple moments [131]. Such measurement does not require a large aperture; for example, a small 15 cm

aperture can provide roughly 1-degree angular resolution at 150 GHz, which is sufficient for observing the CMB at $\ell < 100$. Optimizing the sensitivity was the primary goal when we were designing an optical system for Tau Surveyor.

Since a balloon-borne instrument has upper limits on the allowed weight and overall size, optimally using the cryogenic space to pack telescope(s) in the instrument is essential for improving the number of detectors to optimize the sensitivity. From a dimensional point of view, the occupied space by a telescope with an aperture D is proportional to D^3. Given a limited volume of space, naively speaking the number of telescopes N_t that an instrument can house is proportional to $1/D^3$. As a result, if we assume that the focal plane area per telescope A_{FP} is proportional to D^2, the total focal plane area combining all N_t telescopes, denoted as A_{tot-FP}, follows the relation $A_{tot-FP} = N_t \times A_{FP} \propto 1/D$. This suggests that the total number of detectors in an instrument with multiple small-aperture telescopes may exceed that in an instrument with one large-aperture telescope.

This chapter discusses a trade study on the choice of the optical system that I conducted for the Tau Surveyor, between having one $D = 40$ cm cross-Dragone telescope or multiple $D = 15$ cm cross-Dragone telescopes within one cryostat. The comparisons in terms of the focal plane area, sensitivity, and various other considerations between the two options are discussed.

6.1 Focal Plane Area

The optical designs are based on the same cross Dragone configuration shown in Figure 6.1, except with different aperture sizes $D = 15$ and 40 cm.

Tau Surveyor has six frequency bands that are distributed into three types of feedhorn-coupled, polarization-sensitive, dual-color pixels [132], each with four transition edge sensor (TES) bolometers. I designed the frequency bands based on a number of criteria: (1) each pixel has roughly octave bandwidth, i.e. the ν_{high} of the higher frequency band should be about $2\times$ the ν_{low} of the lower-frequency band within a pixel; (2) no band overlap exists between the two bands in one

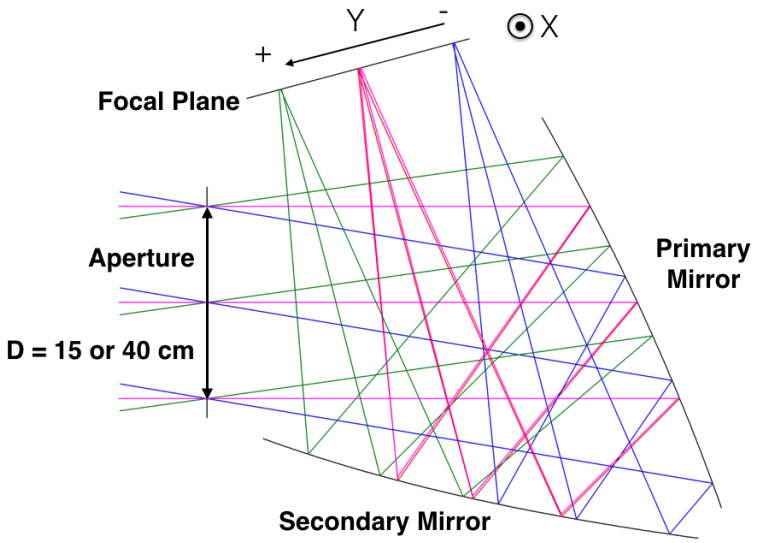

Figure 6.1: The optical designs for Tau Surveyor with D =15 or 40 cm; F-number is 3.

pixel; (3) the lowest band is at 150 GHz, and there should be two bands at > 300 GHz for characterizing foregrounds; (3) the fractional bandwidths should be as large as possible for having large signal-to-noise ratio. The information of the bands is given in Table 6.1

Pixel type	Freq [GHz]	Fractional bandwidth	ν_{low}	ν_{high}
A	150	33%	125	175
	220	33%	184	256
B	180	33%	150	210
	260	33%	217	303
C	310	20%	279	341
	380	30%	342	418

Table 6.1: Tau Surveyor's pixels and frequency bands.

We define the DLFOV for each pixel such that within the DLFOV the Strehl ratio is no less than 0.8 at the highest frequency of that pixel. I calculated the DLFOV for all three pixel types for both $D = 15$ and 40 cm systems in CodeV. The results are shown in Table 6.2 in terms of the major/minor axes on the elliptical

focal plane. The definitions of X and Y directions are given in Figure 6.1. Note that for the $D = 15$ cm system, the limit in the Y direction was due to the vignetting not the Strehl ratio for all pixels.

Pixel type	$D = 15$ cm		$D = 40$ cm		Area Ratio
A	X	33 cm	X	45 cm	1 : 3.0
	Y	18 cm	Y	40 cm	
B	X	30 cm	X	37 cm	1 : 2.2
	Y	18 cm	Y	32 cm	
C	X	23 cm	X	37 cm	1 : 2.9
	Y	18 cm	Y	32 cm	

Table 6.2: The major/minor axes of the available DLFOV on the focal plane. The ratio between focal plane areas are given.

The results above reveals that due to aberrations (quantified by the Strehl ratio) the assumption mentioned in the introduction that the focal plane area per telescope A_{FP} is proportional to D^2 is wrong. Based on this assumption, the ratio of A_{FP} between $D = 15$ cm and $D = 40$ cm should be $1 : 7$. Given the results shown in Table 6.2, it seems that the actual ratio is close to $1/D$ instead and depends on the frequency. Small-aperture telescopes have advantages in this regard, since their focal plane may be not constrained by aberrations at all, such as in the Y direction in the case of $D = 15$ cm.

However, it turned out that the advantage of small-aperture telescopes gained from the optical efficiency significantly surrendered to the packing inefficiency. Given some weight and size limits, we designed a cryostat that packed one $D = 40$ cm telescope and could hold 385 liters of liquid helium for 41-day observation, as shown in the panel (a) of Figure 6.2. We tried to design another cryostat to hold the same amount of liquid helium and to have as many $D = 15$ cm telescopes as possible. All the small telescopes needed to point to the 'front', because the 'back' of a balloon-borne instrument has baffles and solar panels that deal with the sun light; no direct sun light was allowed to enter the optics. The maximum number of small telescopes we achieved was three, as shown in the panel (b)

and (c), a much smaller number than the naive estimation based on dimensional scaling $(40/15)^3 \approx 19$.

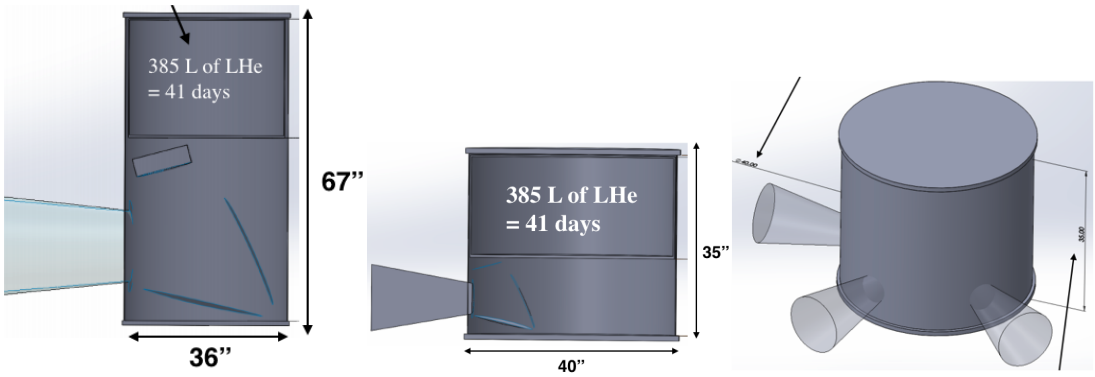

(a) (b) (c)

Figure 6.2: Packing of (a) one $D = 40$ cm and (b)(c) three $D = 15$ cm cross-Dragone systems into cryostats that supports 41 days of observation on a balloon-borne instrument.

We compare the total focal plane area A_{tot-FP} provided by each instrument. For one-telescope $D = 40$ cm system, A_{tot-FP} is just the focal plane area of the $D = 40$ cm telescope for pixel A, because we populate lowest-frequency pixels near the edge and highest-frequency pixels near the center on a focal plane; $A_{tot-FP} \approx 1400$ cm^2. For the three-telescope design with $D = 15$ cm, we assume that each telescope has only one type of pixel for fabrication simplicity, so A_{tot-FP} is the sum of all three telescopes; $A_{tot-FP} \approx 1200$ cm^2.

6.2 Sensitivity

We quantify the sensitivity of a CMB telescope in terms of array noise equivalent temperature (NET) in $\mu K \cdot \sqrt{sec}$ at each of the frequency bands. The array NET is equal to the NET of a single detector divided by the square root of the number of detectors.

Both NET per detector and the number of detectors per focal plane are functions of pixel size. In the NET calculation, the beam waist to pixel diameter ratio

was assumed to be [133]

$$\omega_0 = 0.6435a = \frac{D_{pixel}}{3.108}, \tag{6.1}$$

where ω_0 is $1/e^2$ beam waist, a is the radius of the feed horn, and $D_{pixel} = 2a$ is the pixel diameter. Panel (a) of Figure 6.3 shows my calculation on the NET per detector for the $D = 15$ cm telescope. Larger pixel leads to smaller beam half-angle $\theta = \lambda/(\pi\omega_0)$ and therefore less optical loading from the instrument. In panel (b), I show the calculated number of bolometers versus the pixel diameter given the available focal plane area from last section. In the calculation, I assumed hexagonal packing arrangement, which gives an area density of 0.9069, and I also assumed a 0.2 mm clearance between neighboring pixels.

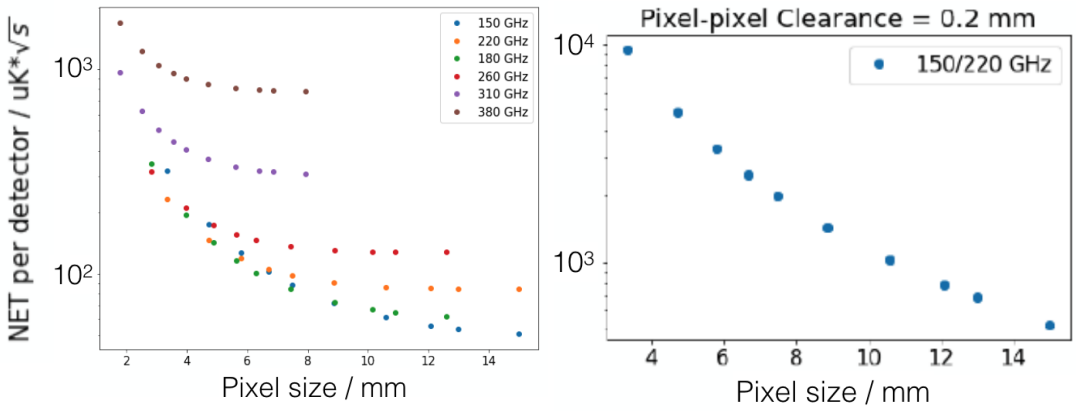

Figure 6.3: (a) NET per detector as a function of pixel diameter for every frequency band. (b) Number of bolometers as a function of pixel diameter, given the focal plane area for the pixel A (150/220 GHz) calculated based on the dimensions shown in Table 6.2. Both plots are for $D = 15$ cm telescope.

The optimal pixel size for each pixel was obtained by first calculating the array NETs versus pixel size based on $NET_{array} = NET_{bolo}/\sqrt{\#\text{ of bolos}}$, and then maximizing the mapping speed, defined as $\sum 1/NET^2_{array}$. One example is shown in Figure 6.4. With the obtained optimal pixel sizes $D_{pixel} = [7.5$ mm, 6.3 mm, 3.1 mm] for pixel type A, B and C respectively, we counted that the

three-telescope instrument would have 24,580 detectors, while the one-telescope instrument would have 22,980 detectors. Considering the pressure on the readout system from such many detectors, and given the fact that slightly larger pixels had only small decreases in mapping speed, we decided to use D_{pixel} = [8.9 mm, 7.5 mm, 4.0 mm] instead; the total number of detectors dropped to 16,116 and 13,668 in three- and one-telescope systems respectively.

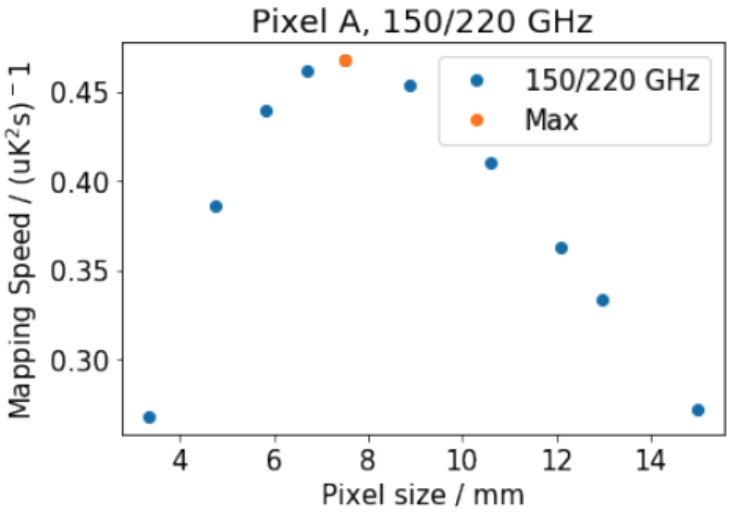

Figure 6.4: Mapping speed versus pixel diameter calculated for pixel A on D = 15 cm telescope. At D_{pixel} = 7.5 mm, the mapping speed is optimized.

The only difference in the NET per detector calculation between the $D = 40$ cm telescope and $D = 15$ cm telescope was the material assumed for the vacuum window. We assumed to use high-resistivity Floating-zone (FZ) silicon as the vacuum window material for $D = 15$ cm telescopes, and to use high density polyethylene (HDPE) for $D = 40$ cm telescope. High-resistivity FZ silicon is a good vacuum window material for millimeter-wave instruments because of its low absorptive loss [25]. However, currently FZ silicon is limited by its size up to 20 cm in diameter. This different choice of the vacuum window material resulted in different optical loadings. For example, in the 150 GHz band, the total optical power was 0.50 pW for the $D = 15$ cm telescope while it was 0.56 pW for the

$D = 40$ cm telescope.

A comparison of the sensitivity between two options in each frequency band is summarized in Table 6.3. Assuming a 65% sky coverage and 480-hr observation time, we estimated the polarization map depth of 11.58 μK·arcmin for the three-telescope design and 9.98 μK·arcmin by the one-telescope design. The deeper map depth that the one-telescope design would achieve is attributed to more 150 GHz detectors it has than the three-telescope design. The low-frequency bands have lower NET_{array} and therefore have higher weight in determining the map depth.

		$D = 15$ cm			$D = 40$ cm		
D_{pixel}	Freq	NET_{bolo}	# of bolos	NET_{array}	NET_{bolo}	# of bolos	NET_{array}
[mm]	[GHz]	$[\mu K \cdot \sqrt{s}]$	-	$[\mu K \cdot \sqrt{s}]$	$[\mu K \cdot \sqrt{s}]$	-	$[\mu K \cdot \sqrt{s}]$
8.9	150	72	1444	1.9	77	3374	1.3
	220	90	1444	2.4	106	3374	1.8
7.5	180	84	1846	2.0	93	1416	2.5
	260	136	1846	3.2	164	1416	4.4
4.0	310	407	4768	5.9	490	2044	10.8
	380	905	4768	13.1	1113	2044	24.6
-	-	Total	16116	-	Total	13668	-

Table 6.3: Sensitivity for three-telescope and one-telescope options.

6.3 Discussion and Conclusion

In this trade study, we learned that a large-aperture optical system is affected more by aberrations compared to small-aperture systems with similar design; increasing aperture size linearly does not increase the DLFOV quadratically.

We designed a three-telescope instrument with $D = 15$ cm telescopes and a one-telescope instrument with $D = 40$ cm telescope for Tau Surveyor. The three-telescope design provided higher sensitivity per detector in all frequency bands than the one-telescope design, thanks to the use of FZ silicon for the vacuum window. However, due to the difficulty of packing multiple small-aperture

(D = 15 cm) telescopes into a balloon-borne cryostat, the total focal plane area supported by the three-telescope design was less than that provided by one $D = 40$ cm telescope. As a result, there was much less (1444 vs. 3374) 150/220 GHz pixels in the three-telescope design compared to the one-telescope design. The final calculation of the polarization map depth concluded that the three-telescope design was an inferior option for Tau Surveyor.

Another critical disadvantage of the three-telescope design was that the scans of the sky by three telescopes would not completely overlap. The reason to have multiple frequency bands in the first place was to let them overlap and be able to clean the foregrounds using the information from different frequencies. It is a great challenge to co-align multiple small-aperture telescopes in a balloon-borne instrument.

In addition, having multiple telescopes has some obvious cons from hardware development perspective. HWP is arguably necessary for controlling the systematics for a large angular scale experiment, such as Tau Surveyor. Having multiple telescopes means the need to build multiple rotating HWPs. In terms of the testing, not only the testing of HWP, but also of focal plane, pointing etc., it would become very time-consuming when there are multiple telescopes.

In conclusion, for a balloon-borne experiment given current technologies, the option of having multiple small-aperture cross-Dragone telescopes within one instrument did not show clear advantages over having one large-aperture cross-Dragone telescope. Instead, many practical disadvantages exists for a multiple-telescope instrument. Nevertheless, it may be possible one day to fully utilize the optical advantage of small-aperture systems, if future battery technology will enable a Polar-night experiment and will make packing much easier.

Chapter 7

Characterization of Multichroic Bolometers Optimized for Balloon-Borne Platforms

Polarization sensitive sinuous antenna multichroic pixel (SAMP) is a technology that has already been deployed by the ground-based telescopes POLARBEAR2 [11] and SPT-3G [10]. One advantage of SAMP is that each pixel has multiple TES bolometers operating in different polarization and frequency bands, therefore increasing the optical throughput without increasing the focal plane size. To use this technology in balloon-borne platforms, which fly in space-like environment above most of the atmosphere, modification is needed to optimize the detectors due to significantly different radiative load from the atmosphere. At float, the radiative power absorbed by the detectors in balloon-borne telescopes is roughly a factor of 10 smaller compared to that in ground-based telescopes and is dominated by the instrument.

Our collaboration team, before I joined, developed new 'meander' legs for connecting the TES to the thermal bath [134]; see panel (c) and (d) in Figure 7.1. The function of these leges is to dump the energy from the TES to the lower-temperature thermal bath, keeping the TES from saturation. Compared to the

straight legs of the TES designed for the ground-based telescopes, such meander legs decrease the average thermal conductance $\overline{G}$ because of their longer thermal lengths. Smaller $\overline{G}$ results in decreased phonon noise and therefore increases the detector sensitivity. In the 150 GHz band, our collaboration successfully decreased $\overline{G}$ from $\sim$ 70 pW/K to the required 9 pW/K for IDS, a proposed balloon-borne experiment [134]. Further development in improving the detector yield, as well as in investigating the coupling between a lenslet and detector chip was needed when I joined the team.

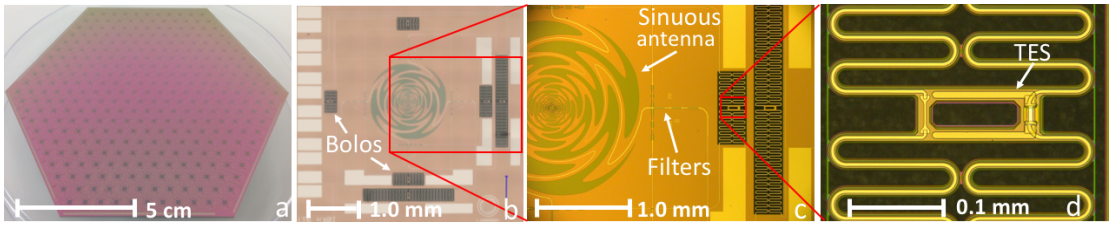

Figure 7.1: (a) A prototype wafer with SAMPs. (b) A three-color (150/250/320 GHz) SAMP; the sinuous antenna is in the center and is connected to 6 bolometers (black strips), one for each polarization and frequency. (c) On-wafer microfabricated band-definition filters are located between the antenna and the bolometers. (d) "Meander" legs that connect the TES to the thermal bath are developed for the lower thermal conductance. Original photos were provided by our collaborators Ben Westbrook and Aritoki Suzuki.

In this chapter, I review the basics of TES and SAMP, and report the key results of my dark and optical characterization tests of the detectors that were fabricated by our collaborators at UC Berkeley. I followed the experimental methodologies described in Kate Raach's PhD thesis [135] using the same EBEX test cryostat (ETC), so I skip some details in that regard.

7.1 Basics of TES and SAMP

7.1.1 TES Bolometer and Saturation Power

TES bolometer measures the power of incident radiation via exploiting the strongly temperature-dependent resistance of the superconducting phase transition. While operating a TES bolometer, a bias voltage is applied to provide electrical power $P_{elec} = V_{bias}^2/R$, where R is the resistance of the TES. When the temperature of TES changes around the superconducting critical temperature T_c due to power dissipation in the bolometer, the electrical power experiences a negative feedback as following

$$\frac{dP_{elec}}{dT} = -\frac{V_{bias}^2}{R^2}\frac{dR}{dT} = -\alpha\frac{P_{elec}}{T_c}, \tag{7.1}$$

where α is logarithmic slope of superconducting transition $\alpha \equiv \frac{T_c}{R}\frac{dR}{dT} = \frac{d\log R}{d\log T} > 0$. This negative feedback allows locking the TES onto a sharp transition phase at T_c.

From the perspective of conservation of energy, the total power going into the TES, which consists of the optical loading and the electrical power, is equal to the power dumping out to the thermal bath at T_{bath}. Mathematically,

$$P_{in} = P_{opt} + P_{elec} = \overline{G}(T_c - T_{bath}) \equiv P_{sat}, \tag{7.2}$$

where $\overline{G}$ is the average thermal conductance. We define P_{sat} as the maximal power the bolometer can absorb before saturation; a P_{in} that is larger than P_{sat} heats up the TES from transition state to normal state. Therefore, when designing a TES bolometer, P_{sat} is picked such that it is a factor of few larger than the expected P_{opt}, allowing P_{elec} to have room to provide negative feedback. However, P_{sat} should not be unnecessarily large because increasing P_{sat} (by increasing $\overline{G}$) will increase phonon noise. For IDS, we calculated a 0.2 pW optical load in the 150 GHz band, and include a 0.4 pW margin to account for the known challenge of assembling a cryostat to the theoretical specifications. Assuming a safety factor

of 2.5, we set a target P_{sat} at 1.5 pW for the 150 GHz band.

Note that for a given TES, $\overline{G}$ and P_{sat} are functions of T_c and T_{bath} (because the thermal conductivity changes with respect to temperature). Suppose that we measure $P_{sat,1}$ at $T_{bath,1}$ and $P_{sat,2}$ at $T_{bath,2}$. The scaling relationship between the saturation power measured at two different bath temperatures is

$$\frac{P_{sat,1}}{P_{sat,2}} = \frac{T_c^{n+1} - T_{bath,1}^{n+1}}{T_c^{n+1} - T_{bath,2}^{n+1}}, \tag{7.3}$$

where n is an index for thermal conductivity where $n = 1$ for electron based conduction and $n = 3$ for phonon heat transfer. For the detectors we were developing, an average value of 2.6 for n was measured [134].

7.1.2 Lenslet Coupled SAMP

The basic configuration of a lenslet coupled SAMP is shown in Figure 7.2. A silicon or alumina hemispherical lenslet with some extension on the botoom focuses the normally incident radiation to the sinuous antenna at the center of the pixel. The broadband sinuous antenna absorbs the focused light in orthogonal polarizations. The niobium microstrips over silicon nitride couple the antenna to the TES passing through band-defining filters, as shown in the panel (c) of Figure 7.1. The SAMP I was testing had six TES bolometers on each pixel at 150, 250, 320 GHz in two orthogonal polarizations.

7.2 Dark Characterization

In the dark characterization tests, detector chips were enclosed in a light-tight box which was heat sunk to the thermal bath measured at $\sim$ 323 mK. No lenslet was used in dark tests. The detector signals were read out using digital frequency domain multiplexer (DfMUX) electronics. I performed characterizations on the critical temperature T_c, normal resistance R_n, saturation power P_{sat} and average

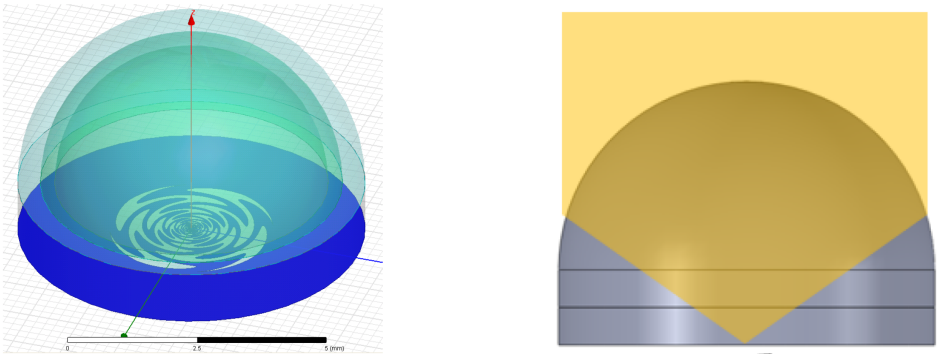

(a) (b)

Figure 7.2: CAD of a lenslet coupling radiation to a sinuous antenna. These nice pictures were taken from our collaborator Aritoki Suzuki's PhD thesis [124].

thermal conductance $\overline{G}$ of the detectors.

(In Run07 for internal reference) I measured three detector chips, which had $6 \times 3 = 18$ detectors in total. 15 out of 18 were found through network analysis; the other three most likely had bad wire bonding connections. By conducting Lorentzian fitting to the network analysis peaks, I found the R_n for the remaining 15 bolometers.

I obtained the measurements of T_c for 13 bolometers out of the 15 found above; one bolometer behaved like a normal resistor and another one was not measured successfully due to some non-stability of the SQUID (superconducting quantum interference device) that was used. For the measurement of T_c, a negligible bias voltage 5 nV_{rms} was applied to enable a measurable current signal. By slowly changing the bath temperature, less than 5 mK/min, from around 600 mK to 370 mK and then back to 600 mK, the resistance was measured, as shown in Figure 7.3. It was extremely important to change T_{bath} slowly and in two directions (going down and up), because (1) the resolution in temperature needed to be high enough to characterize the sharp transition and (2) the temperature of bolometers were readout using the measured T_{bath}. If changing too fast, the measured T_{bath} would not track the temperature of bolometers accurately, and R vs T curves in the panel (c) of Figure 7.3 would have a bigger gap in apparent T_c between the data

obtained during the cooling-down and the warming-up.

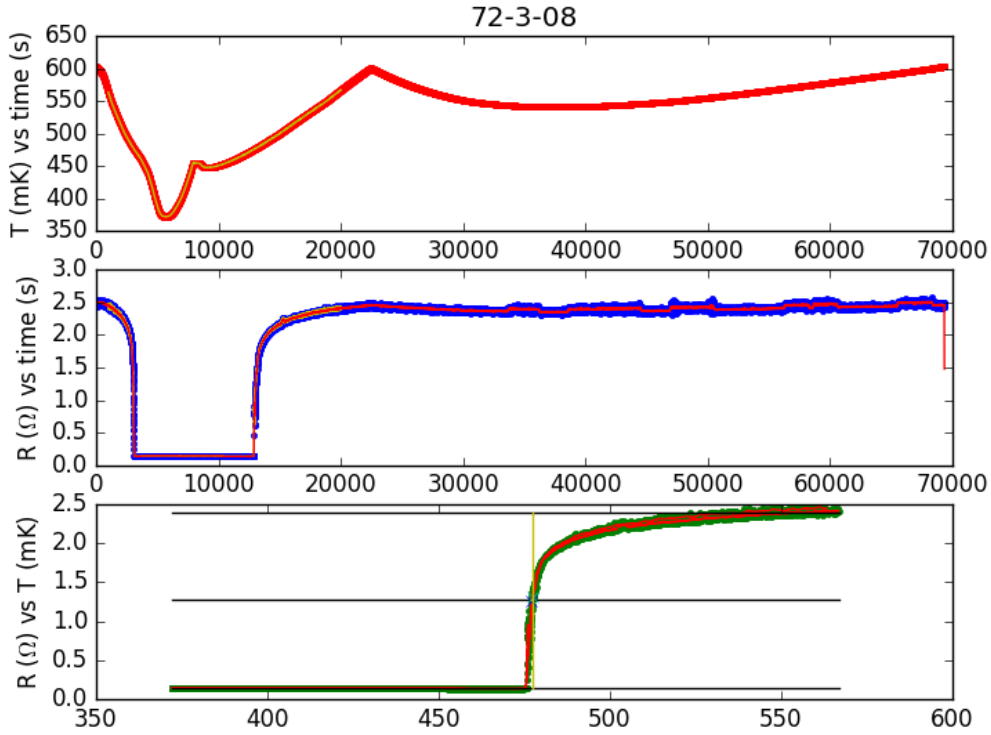

Figure 7.3: Example of T_c measurement result. The upper panel shows the change of T_{bath} as a function of time. The middle panel shows the measured resistance during the same time. The measurement could have been terminated after the first 20,000 seconds. The lower panel plots the resistance vs T_{bath} measured at the same time, showing a clear superconducting phase transition around 475 mK.

In the dark tests, because of the low enclosure bath temperature (323 mK), we neglected the radiative power on the bolometers. According to Eq. 7.2, $P_{sat} = P_{elec}$ when $P_{opt} = 0$. So I measured the P_{sat} at this bath temperature by measuring the P_{elec} at the transition. Figure 7.4 gives an example of such measurement. I plotted the P_{sat} against the meander leg linear length in Figure 7.5; the data followed an expected $1/L$ trend nicely. With the measured P_{sat}, as well as the measured T_c, T_{bath}, I calculated the average thermal conductance using Eq. 7.2.

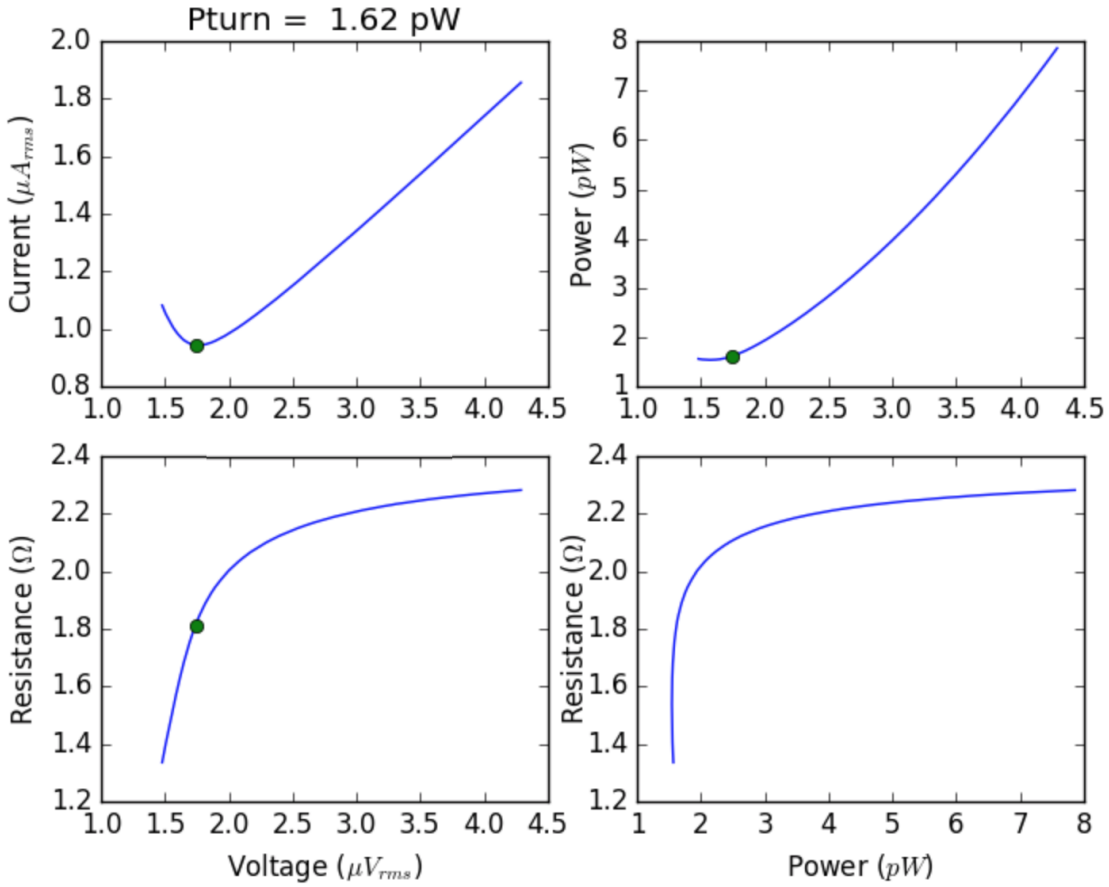

Figure 7.4: Example of P_{sat} measurement. Above super transition, the current followed voltage nearly linearly and the resistance was approximately flat around 2.2 Ω. As the TES began to superconduct, the resistance dropped sharply and the current experienced a turnaround. In the superconducting transition, the power (top right) was roughly kept as a fixed level by the negative feedback explained in Section 7.1.1. The electrical power at the turning point (dark green) was deemed as a good representation of P_{sat}.

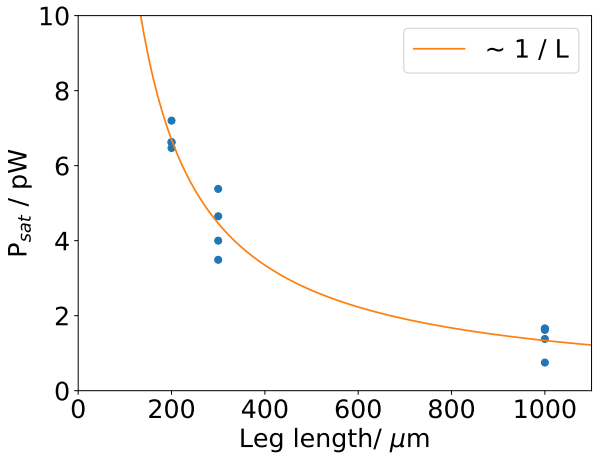

Figure 7.5: Measured P_{sat} vs leg length. The orange curve fits the data with a linear function of the reciprocal of leg length.

The average values of all the measurements described above, and the meander leg length are summarized in Table 7.1. The results indicated good agreement to the design.

Freq [GHz]	Meander leg [μm]	T_c [mK]	Rn [Ω]	P_{sat} [pW]	$\bar{G}$ [pW/K]
150	1000	473	2.8	1.4	9.3
250	300	459	2.9	4.4	34
320	200	483	3.2	6.7	42

Table 7.1: Average values of the measurements in each frequency band. T_{bath} = 323 mK.

7.3 Optical Characterization

In the optical characterization tests, an AR-coated (centered at 165 GHz; not optimized for IDS pixel), 1/2-inch alumina lenslet was assembled by our collaborators at UC Berkeley to one of the detector chips that had been tested in the dark characterizations. Panel (a) of Figure 7.6 shows a drawing of a similar assembly

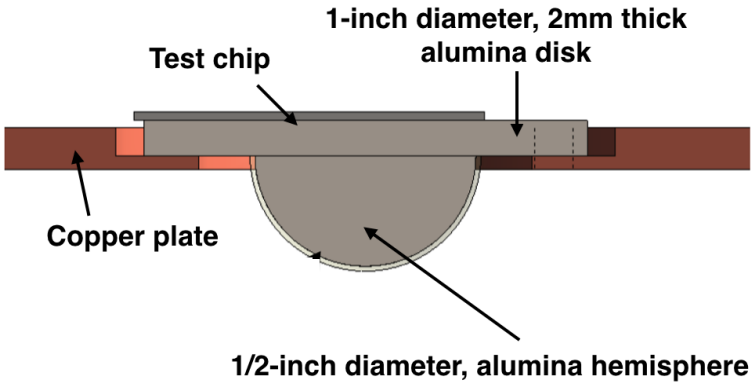

(a)

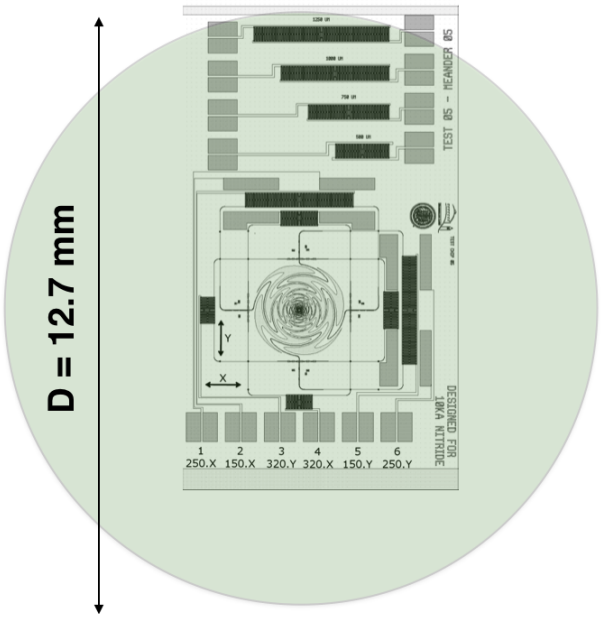

(b)

Figure 7.6: (a) Drawing of a similar Lenslet-chip test assembly provided by Aritoki Suzuki. (b) Test chip layout with lenslet's projection (green circle).

to illustrate the configuration. The copper plate was heat sunk to the thermal bath. The center of the lenslet was aligned to the center of the sinuous antenna, as shown in the panel (b) where the green shaded area is a projection of the lenslet onto the chip layout. On the same chip, within the lenslet's projection, there were four other independent meander legged TES bolometers that were not coupled to any sinuous antenna. They were legacy designs during the development of the low-conductance meander legs.

Karl Young, another graduate student in the Cosmolab at UMN working on this project, designed an experimental setup that integrated the lenslet assembly into the ETC; see Figure 7.7. We controlled the temperature of the blackbody to adjust the optical load. Our goal was to measure the optical efficiency for each bolometer defined by $\epsilon = P_{opt}/P_{BB}$, where P_{opt} is the actual optical load absorbed by the bolometer and P_{BB} is the theoretical prediction of optical load from the blackbody into the bolometer. Because the optical load $P_{opt} = P_{sat} - P_{elec}$ according to Eq. 7.2, we can rewrite the optical efficiency as:

$$\epsilon = \frac{P_{opt}}{P_{BB}} = \frac{P_{sat} - P_{elec}}{P_{BB}}. \tag{7.4}$$

Therefore,

$$P_{elec} = P_{sat} - \epsilon P_{BB}. \tag{7.5}$$

Since the saturation power P_{sat} of a TES bolometer is a constant (at fixed bath temperature), the optical efficiency is the slope of P_{elec} versus P_{BB}. We adjusted the temperature of the blackbody to provide different P_{BB} and measured P_{elec} at each temperature. We calculated the P_{BB} using the measured temperature of the blackbody and assuming λ^2 throughput, single polarization for each bolometer, frequency bands from both measurement and simulation provided by our collaborators at UC Berkeley, and blackbody emissivity of 1. We measured P_{elec} at the superconducting transition in the exactly same way described in the dark tests. We found the optical efficiency by fitting the data of P_{elec} versus P_{BB} with the linear relationship in Eq. 7.5.

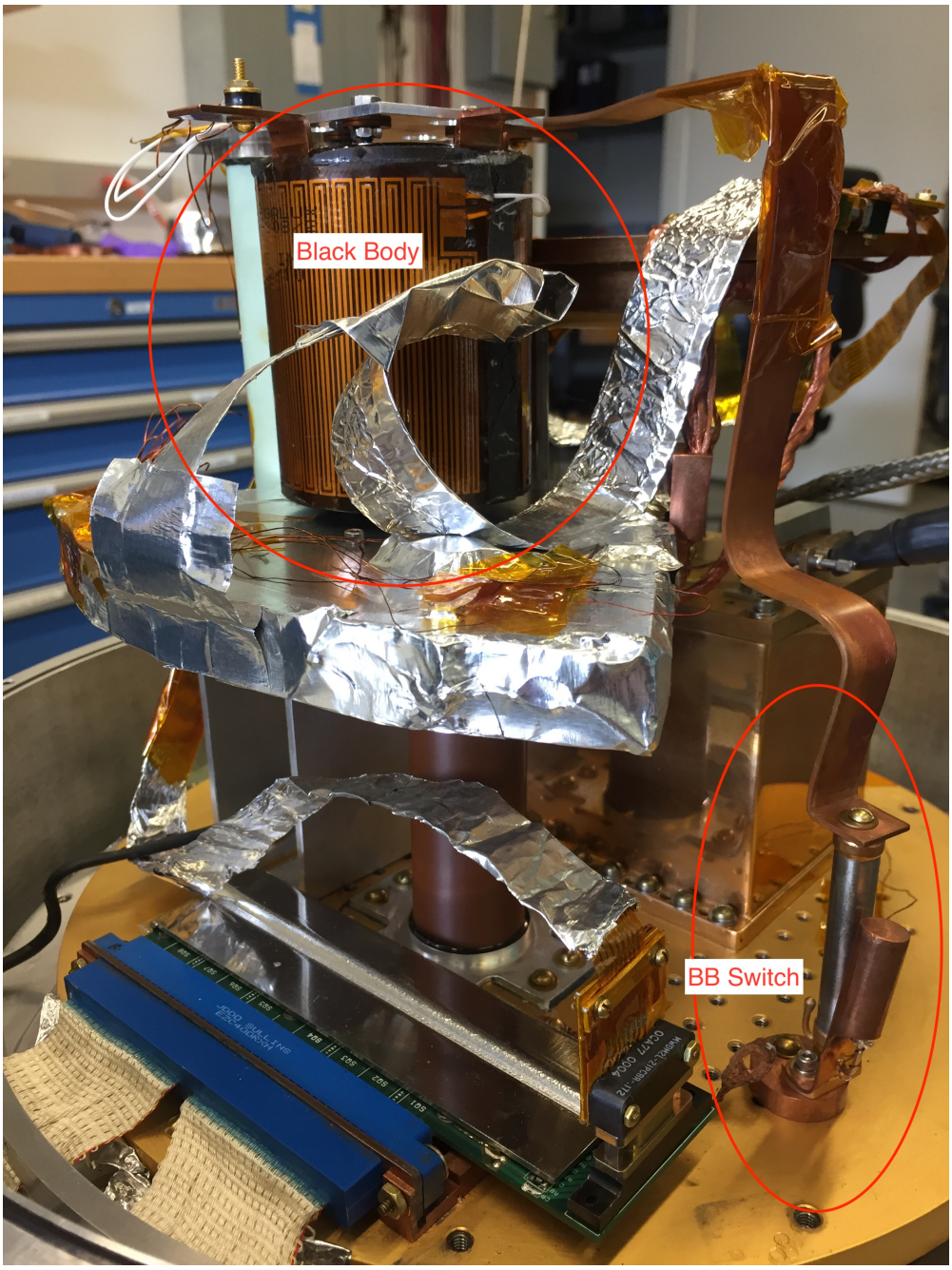

Figure 7.7: The optical efficiency setup designed by Karl Young. A blackbody made by Kate Raach [135] was several millimeters above the enclosure box in which we had the lenslet assembly and LC board for readout. The lenslet was directly facing up the center of the black body. The box was aluminum taped leaving only the lenslet exposed to ensure good light tightness except through the lenslet.

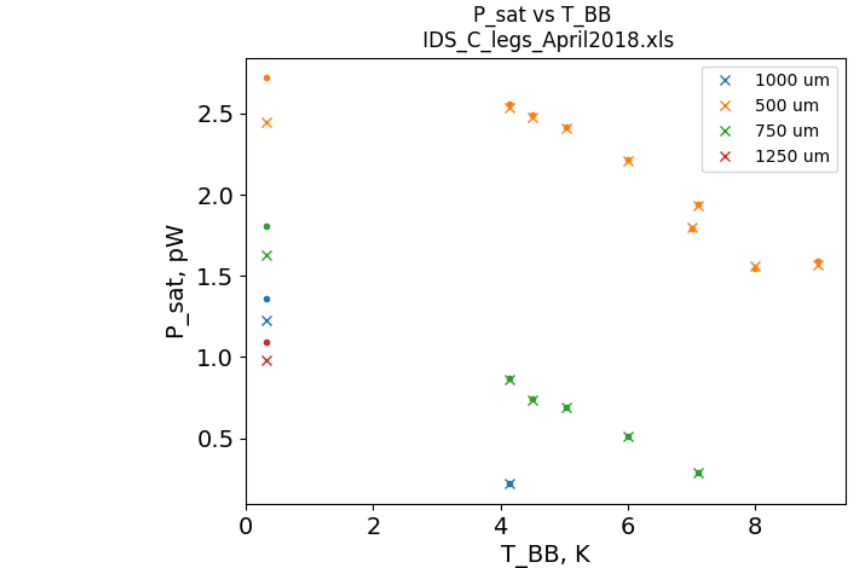

(a)

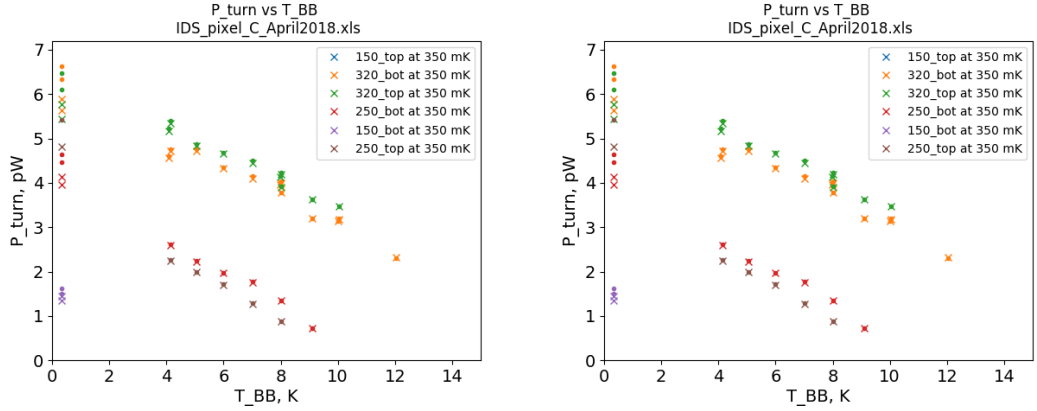

(b) (c)

Figure 7.8: Measured P_{elec} vs the blackbody temperature T_{BB} for **(a)** four meander legged TES bolometers that were not coupled to antenna; for **(b)** antenna coupled SAMP bolometers; for **(c)** the same SAMP bolometers after cutting the transmission lines to the sinuous antenna in another experimental run. The points were the actual measured values while the crosses were the expected values normalized to $T_{bath} = 350$ mK based on Eq. 7.3. The data at $T_{BB} = 350$ mK were extrapolated from the dark tests.

The optical efficiency was expected to be around 50% based on the past data for the lenslet coupled SAMP. However, An experiment (Run08 for internal reference), which was led by Karl Young and assisted by me, measured higher than 100% optical efficiencies on almost all of the test bolometers, suggesting the existence of excess optical loading on the bolometers.

We conducted two other verification runs (Run09 and Run10 for internal reference) to investigate the possible excess loading. In the Run09, we decided to include the four independent meander legged TES on the same chip, as shown in the panel (b) of Figure 7.6. Since they were not coupled to any antenna, they were not expected to respond to the optical loading. Surprisingly, the data shown in the panel (a) of Figure 7.8 suggested that these isolated bolometers did respond to the optical loading in a behavior as if they were coupled to antenna; for example the bolometer with the longest leg length (1250 μm) and therefore with smallest P_{sat} was already saturated at $T_{BB} = 4$K. In Run10, I physically cut the transmission lines that connected the bolometers to the sinuous antenna. Panel (b) and (c) show the measurements of the tested bolometers before (Run09) and after (Run10) cutting the transmission lines. The results again supported the idea of direct coupling to the bolometers not through the sinuous antenna.

Some preliminary simulation done by our collaborators at UC Berkeley suggested possible sidelobes from the lenslet that focused the radiation to non-center locations. More investigation on the direct interaction between the meander legs and radiation may be helpful to solve the puzzle.

References

[1] Arno A Penzias and Robert Woodrow Wilson. A measurement of excess antenna temperature at 4080 mc/s. *The Astrophysical Journal*, 142:419–421, 1965.

[2] Scott Dodelson. *Modern cosmology*. Elsevier, 2003.

[3] A. D. Linde. A new inflationary universe scenario: A possible solution of the horizon, flatness, homogeneity, isotropy and primordial monopole problems. *Physics Letters B*, 108:389–393, February 1982.

[4] A. H. Guth and S. Pi. Fluctuations in the new inflationary universe. *Phys. Rev. Lett.*, 49:1110–1113, October 1982.

[5] R. Allison, P. Caucal, E. Calabrese, J. Dunkley, and T. Louis. Towards a cosmological neutrino mass detection. *Phys. Rev. D*, 92:123535, Dec 2015.

[6] Frank H. Shu, Fred C. Adams, and Susana Lizano. Star formation in molecular clouds: Observation and theory. *Annual Review of Astronomy and Astrophysics*, 25(1):23–81, 1987, https://doi.org/10.1146/annurev.aa.25.090187.000323.

[7] Linda J Tacconi, Reinhard Genzel, and Amiel Sternberg. The evolution of the star-forming interstellar medium across cosmic time. *Annual Review of Astronomy and Astrophysics*, 58:157–203, 2020.

[8] Event Horizon Telescope Collaboration et al. First m87 event horizon telescope results. i. the shadow of the supermassive black hole. *arXiv preprint arXiv:1906.11238*, 2019.

[9] N. Galitzki, A. Ali, K. S. Arnold, P. C. Ashton, J. E. Austermann, C. Baccigalupi, T. Baildon, D. Barron, J. A. Beall, S. Beckman, S. M. M. Bruno, S. Bryan, P. G. Calisse, G. E. Chesmore, Y. Chinone, S. K. Choi, G. Coppi, K. D. Crowley, K. T. Crowley, A. Cukierman, M. J. Devlin, S. Dicker, B. Dober, S. M. Duff, J. Dunkley, G. Fabbian, P. A. Gallardo, M. Gerbino, N. Goeckner-Wald, J. E. Golec, J. E. Gudmundsson, E. E. Healy, S. Henderson, C. A. Hill, G. C. Hilton, S.-P. P. Ho, L. A. Howe, J. Hubmayr, O. Jeong, B. Keating, B. J. Koopman, K. Kiuchi, A. Kusaka, J. Lashner, A. T. Lee, Y. Li, M. Limon, M. Lungu, F. Matsuda, P. D. Mauskopf, A. J. May, N. McCallum, J. McMahon, F. Nati, M. D. Niemack, J. L. Orlowski-Scherer, S. C. Parshley, L. Piccirillo, M. Sathyanarayana Rao, C. Raum, M. Salatino, J. S. Seibert, C. Sierra, M. Silva-Feaver, S. M. Simon, S. T. Staggs, J. R. Stevens, A. Suzuki, G. Teply, R. Thornton, C. Tsai, J. N. Ullom, E. M. Vavagiakis, M. R. Vissers, B. Westbrook, E. J. Wollack, Z. Xu, and N. Zhu. The Simons Observatory: instrument overview. In *Society of Photo-Optical Instrumentation Engineers (SPIE) Conference Series*, volume 10708 of *Society of Photo-Optical Instrumentation Engineers (SPIE) Conference Series*, page 1070804, July 2018, 1808.04493.

[10] B. A. Benson, P. A. R. Ade, Z. Ahmed, S. W. Allen, K. Arnold, J. E. Austermann, A. N. Bender, L. E. Bleem, J. E. Carlstrom, C. L. Chang, H. M. Cho, J. F. Cliche, T. M. Crawford, A. Cukierman, T. de Haan, M. A. Dobbs, D. Dutcher, W. Everett, A. Gilbert, N. W. Halverson, D. Hanson, N. L. Harrington, K. Hattori, J. W. Henning, G. C. Hilton, G. P. Holder, W. L. Holzapfel, K. D. Irwin, R. Keisler, L. Knox, D. Kubik, C. L. Kuo, A. T. Lee, E. M. Leitch, D. Li, M. McDonald, S. S. Meyer, J. Montgomery, M. Myers, T. Natoli, H. Nguyen, V. Novosad, S. Padin, Z. Pan, J. Pearson,

C. Reichardt, J. E. Ruhl, B. R. Saliwanchik, G. Simard, G. Smecher, J. T. Sayre, E. Shirokoff, A. A. Stark, K. Story, A. Suzuki, K. L. Thompson, C. Tucker, K. Vanderlinde, J. D. Vieira, A. Vikhlinin, G. Wang, V. Yefremenko, and K. W. Yoon. SPT-3G: a next-generation cosmic microwave background polarization experiment on the South Pole telescope. In *Society of Photo-Optical Instrumentation Engineers (SPIE) Conference Series*, volume 9153 of *Society of Photo-Optical Instrumentation Engineers (SPIE) Conference Series*, page 1, July 2014, 1407.2973.

[11] T. Matsumura, P. Ade, K. Arnold, D. Barron, J. Borrill, S. Chapman, Y. Chinone, M. Dobbs, J. Errard, G. Fabbian, A. Ghribi, W. Grainger, N. Halverson, M. Hasegawa, K. Hattori, M. Hazumi, W. L. Holzapfel, Y. Inoue, S. Ishii, Y. Kaneko, B. Keating, Z. Kermish, N. Kimura, T. Kisner, W. Kranz, A. T. Lee, F. Matsuda, H. Morii, M. J. Myers, H. Nishino, T. Okamura, E. Quealy, C. Reichardt, P. L. Richards, D. Rosen, C. Ross, A. Shimizu, M. Sholl, P. Siritanasak, P. Smith, N. Stebor, R. Stompor, A. Suzuki, J.-i. Suzuki, S. Takada, K.-i. Tanaka, T. Tomaru, and O. Zahn. POLARBEAR-2 optical and polarimeter designs. In *Society of Photo-Optical Instrumentation Engineers (SPIE) Conference Series*, volume 8452 of *Society of Photo-Optical Instrumentation Engineers (SPIE) Conference Series*, page 3, September 2012.

[12] M. Niemack and ACTPol Collaboration. ACTPol: A New Instrument to Measure CMB Polarization with the Atacama Cosmology Telescope. In *American Astronomical Society Meeting Abstracts*, volume 221 of *American Astronomical Society Meeting Abstracts*, page 105.04, January 2013.

[13] Cosmic Microwave Background Stage 4 Concept Definition Task Force – Report to the AAAC. https://bit.ly/2OCamU4, October 2017.

[14] T. Matsumura, Y. Akiba, K. Arnold, J. Borrill, R. Chendra, Y. Chinone, A. Cukierman, T. de Haan, M. Dobbs, A. Dominjon, T. Elleflot,

J. Errard, T. Fujino, H. Fuke, N. Goeckner-wald, N. Halverson, P. Harvey, M. Hasegawa, K. Hattori, M. Hattori, M. Hazumi, C. Hill, G. Hilton, W. Holzapfel, Y. Hori, J. Hubmayr, K. Ichiki, J. Inatani, M. Inoue, Y. Inoue, F. Irie, K. Irwin, H. Ishino, H. Ishitsuka, O. Jeong, K. Karatsu, S. Kashima, N. Katayama, I. Kawano, B. Keating, A. Kibayashi, Y. Kibe, Y. Kida, K. Kimura, N. Kimura, K. Kohri, E. Komatsu, C. L. Kuo, S. Kuromiya, A. Kusaka, A. Lee, E. Linder, H. Matsuhara, S. Matsuoka, S. Matsuura, S. Mima, K. Mitsuda, K. Mizukami, H. Morii, T. Morishima, M. Nagai, T. Nagasaki, R. Nagata, M. Nakajima, S. Nakamura, T. Namikawa, M. Naruse, K. Natsume, T. Nishibori, K. Nishijo, H. Nishino, T. Nitta, A. Noda, T. Noguchi, H. Ogawa, S. Oguri, I. S. Ohta, C. Otani, N. Okada, A. Okamoto, A. Okamoto, T. Okamura, G. Rebeiz, P. Richards, S. Sakai, N. Sato, Y. Sato, Y. Segawa, S. Sekiguchi, Y. Sekimoto, M. Sekine, U. Seljak, B. Sherwin, K. Shinozaki, S. Shu, R. Stompor, H. Sugai, H. Sugita, T. Suzuki, A. Suzuki, O. Tajima, S. Takada, S. Takakura, K. Takano, Y. Takei, T. Tomaru, N. Tomita, P. Turin, S. Utsunomiya, Y. Uzawa, T. Wada, H. Watanabe, B. Westbrook, N. Whitehorn, Y. Yamada, N. Yamasaki, T. Yamashita, M. Yoshida, T. Yoshida, and Y. Yotsumoto. LiteBIRD: Mission Overview and Focal Plane Layout. *Journal of Low Temperature Physics*, 184:824–831, August 2016.

[15] S. W. Henderson, R. Allison, J. Austermann, T. Baildon, N. Battaglia, J. A. Beall, D. Becker, F. De Bernardis, J. R. Bond, E. Calabrese, S. K. Choi, K. P. Coughlin, K. T. Crowley, R. Datta, M. J. Devlin, S. M. Duff, J. Dunkley, R. Dünner, A. van Engelen, P. A. Gallardo, E. Grace, M. Hasselfield, F. Hills, G. C. Hilton, A. D. Hincks, R. Hložek, S. P. Ho, J. Hubmayr, K. Huffenberger, J. P. Hughes, K. D. Irwin, B. J. Koopman, A. B. Kosowsky, D. Li, J. McMahon, C. Munson, F. Nati, L. Newburgh, M. D. Niemack, P. Niraula, L. A. Page, C. G. Pappas, M. Salatino, A. Schillaci, B. L. Schmitt, N. Sehgal, B. D. Sherwin, J. L. Sievers, S. M. Simon, D. N.

Spergel, S. T. Staggs, J. R. Stevens, R. Thornton, J. Van Lanen, E. M. Vavagiakis, J. T. Ward, and E. J. Wollack. Advanced ACTPol Cryogenic Detector Arrays and Readout. *Journal of Low Temperature Physics*, 184:772–779, August 2016, 1510.02809.

[16] Howard Hui, P. A. R. Ade, Z. Ahmed, R. W. Aikin, K. D. Alexander, D. Barkats, S. J. Benton, C. A. Bischoff, J. J. Bock, R. Bowens-Rubin, J. A. Brevik, I. Buder, E. Bullock, V. Buza, J. Connors, J. Cornelison, B. P. Crill, M. Crumrine, M. Dierickx, L. Duband, C. Dvorkin, J. P. Filippini, S. Fliescher, J. Grayson, G. Hall, M. Halpern, S. Harrison, S. R. Hildebrandt, G. C. Hilton, K. D. Irwin, J. Kang, K. S. Karkare, E. Karpel, J. P. Kaufman, B. G. Keating, S. Kefeli, S. A. Kernasovskiy, J. M. Kovac, C.-L. Kuo, K. Lau, N. A. Larsen, E. M. Leitch, M. Lueker, K. G. Megerian, L. Moncelsi, T. Namikawa, C. B. Netterfield, H. T. Nguyen, R. O'Brient, R. W. Ogburn IV, S. Palladino, C. Pryke, B. Racine, S. Richter, R. Schwarz, A. Schillaci, C. D. Sheehy, A. Soliman, T. St. Germaine, Z. K. Staniszewski, B. Steinbach, R. V. Sudiwala, G. P. Teply, K. L. Thompson, J. E. Tolan, C. Tucker, A. D. Turner, C. Umilt, A. G. Vieregg, A. Wandui, A. C. Weber, D. V. Wiebe, J. Willmert, C. L. Wong, W. L. K. Wu, E. Yang, K. W. Yoon, and C. Zhang. BICEP Array: a multi-frequency degree-scale CMB polarimeter. In Jonas Zmuidzinas and Jian-Rong Gao, editors, *Millimeter, Submillimeter, and Far-Infrared Detectors and Instrumentation for Astronomy IX*, volume 10708, pages 1 – 15. International Society for Optics and Photonics, SPIE, 2018.

[17] Y. Inoue, P. Ade, Y. Akiba, C. Aleman, K. Arnold, C. Baccigalupi, B. Barch, D. Barron, A. Bender, D. Boettger, J. Borrill, S. Chapman, Y. Chinone, A. Cukierman, T. de Haan, M. A. Dobbs, A. Ducout, R. Dnner, T. Elleflot, J. Errard, G. Fabbian, S. Feeney, C. Feng, G. Fuller, A. J. Gilbert, N. Goeckner-Wald, J. Groh, G. Hall, N. Halverson, T. Hamada, M. Hasegawa, K. Hattori, M. Hazumi, C. Hill, W. L. Holzapfel, Y. Hori,

L. Howe, F. Irie, G. Jaehnig, A. Jaffe, O. Jeong, N. Katayama, J. P. Kaufman, K. Kazemzadeh, B. G. Keating, Z. Kermish, R. Keskitalo, T. S. Kisner, A. Kusaka, M. Le Jeune, A. T. Lee, D. Leon, E. V. Linder, L. Lowry, F. Matsuda, T. Matsumura, N. Miller, K. Mizukami, J. Montgomery, M. Navaroli, H. Nishino, H. Paar, J. Peloton, D. Poletti, G. Puglisi, C. R. Raum, G. M. Rebeiz, C. L. Reichardt, P. L. Richards, C. Ross, K. M. Rotermund, Y. Segawa, B. D. Sherwin, I. Shirley, P. Siritanasak, N. Stebor, R. Stompor, J. Suzuki, A. Suzuki, O. Tajima, S. Takada, S. Takatori, G. P. Teply, A. Tikhomirov, T. Tomaru, N. Whitehorn, A. Zahn, and O. Zahn. POLARBEAR-2: an instrument for CMB polarization measurements. In Wayne S. Holland and Jonas Zmuidzinas, editors, *Millimeter, Submillimeter, and Far-Infrared Detectors and Instrumentation for Astronomy VIII*, volume 9914, pages 372 – 380. International Society for Optics and Photonics, SPIE, 2016.

[18] He Gao, Congzhan Liu, Zhangwei Li, Yang Liu, Yongping Li, Siyu Li, Hong Li, Guanhua Gao, Fangjun Lu, and Xinmin Zhang. Introduction to the detection technology of Ali CMB polarization telescope. *Radiation Detection Technology and Methods*, 1(2):12, Jul 2017.

[19] A. N. Bender, P. A. R. Ade, Z. Ahmed, A. J. Anderson, J. S. Avva, K. Aylor, P. S. Barry, R. Basu Thakur, B. A. Benson, L. S. Bleem, S. Bocquet, K. Byrum, J. E. Carlstrom, F. W. Carter, T. W. Cecil, C. L. Chang, H.-M. Cho, J. F. Cliche, T. M. Crawford, A. Cukierman, T. de Haan, E. V. Denison, J. Ding, M. A. Dobbs, S. Dodelson, D. Dutcher, W. Everett, A. Foster, J. Gallicchio, A. Gilbert, J. C. Groh, S. T. Guns, N. W. Halverson, A. H. Harke-Hosemann, N. L. Harrington, J. W. Henning, G. C. Hilton, G. P. Holder, W. L. Holzapfel, N. Huang, K. D. Irwin, O. B. Jeong, M. Jonas, A. Jones, T. S. Khaire, L. Knox, A. M. Kofman, M. Korman, D. L. Kubik, S. Kuhlmann, C.-L. Kuo, A. T. Lee, E. M. Leitch, A. E. Lowitz, S. S. Meyer, D. Michalik, J. Montgomery, A. Nadolski, T. Natoli, H. Ngyuen, G. I.

Noble, V. Novosad, S. Padin, Z. Pan, J. Pearson, C. M. Posada, W. Quan, S. Raghunathan, A. Rahlin, C. L. Reichardt, J. E. Ruhl, J. T. Sayre, E. Shirokoff, G. Smecher, J. A. Sobrin, A. A. Stark, K. T. Story, A. Suzuki, K. L. Thompson, C. Tucker, L. R. Vale, K. Vanderlinde, J. D. Vieira, G. Wang, N. Whitehorn, W. L. K. Wu, V. Yefremenko, K. W. Yoon, and M. R. Young. Year two instrument status of the SPT-3G cosmic microwave background receiver. In *Society of Photo-Optical Instrumentation Engineers (SPIE) Conference Series*, volume 10708 of *Society of Photo-Optical Instrumentation Engineers (SPIE) Conference Series*, page 1070803, July 2018, 1809.00036.

[20] Y. Sekimoto, P. Ade, K. Arnold, J. Aumont, J. Austermann, C. Baccigalupi, A. Banday, R. Banerji, S. Basak, S. Beckman, M. Bersanelli, J. Borrill, F. Boulanger, M. L. Brown, M. Bucher, E. Calabrese, A. Challinor, Y. Chinone, F. Columbro, A. Cukierman, D. Curtis, P. de Bernardis, M. de Petris, M. Dobbs, T. Dotani, L. Duband, A. Ducout, K. Ebisawa, T. Elleflot, H. Eriksen, J. Errard, R. Flauger, C. Franceschet, U. Fuskeland, K. Ganga, J. R. Gao, T. Ghigna, J. Grain, A. Gruppuso, N. Halverson, P. Hargrave, T. Hasebe, M. Hasegawa, M. Hattori, M. Hazumi, S. Henrot-Versille, C. Hill, Y. Hirota, E. Hivon, D. T. Hoang, J. Hubmayr, K. Ichiki, H. Imada, H. Ishino, G. Jaehnig, H. Kanai, S. Kashima, Y. Kataoka, N. Katayama, T. Kawasaki, R. Keskitalo, A. Kibayashi, T. Kikuchi, K. Kimura, T. Kisner, Y. Kobayashi, N. Kogiso, K. Kohri, E. Komatsu, K. Komatsu, K. Konishi, N. Krachmalnicoff, C. L. Kuo, N. Kurinsky, A. Kushino, L. Lamagna, A. T. Lee, E. Linder, B. Maffei, M. Maki, A. Mangilli, E. Martinez-Gonzalez, S. Masi, T. Matsumura, A. Mennella, Y. Minami, K. Mistuda, D. Molinari, L. Montier, G. Morgante, B. Mot, Y. Murata, A. Murphy, M. Nagai, R. Nagata, S. Nakamura, T. Namikawa, P. Natoli, T. Nishibori, H. Nishino, F. Noviello, C. O'Sullivan, H. Ochi, H. Ogawa, H. Ogawa, H. Ohsaki, I. Ohta, N. Okada, G. Patanchon, F. Piacentini, G. Pisano, G. Polenta, D. Poletti, G. Puglisi, C. Raum, S. Realini, M. Remazeilles, H. Sakurai, Y. Sakurai, G. Savini, B. Sherwin, K. Shinozaki, M. Shiraishi, G. Signorelli,

G. Smecher, R. Stompor, H. Sugai, S. Sugiyama, A. Suzuki, J. Suzuki, R. Takaku, H. Takakura, S. Takakura, E. Taylor, Y. Terao, K. L. Thompson, B. Thorne, M. Tomasi, H. Tomida, N. Trappe, M. Tristram, M. Tsuji, M. Tsujimoto, S. Uozumi, S. Utsunomiya, N. Vittorio, N. Watanabe, I. Wehus, B. Westbrook, B. Winter, R. Yamamoto, N. Y. Yamasaki, M. Yanagisawa, T. Yoshida, J. Yumoto, M. Zannoni, and A. Zonca. Concept design of the LiteBIRD satellite for CMB B-mode polarization. In *Society of Photo-Optical Instrumentation Engineers (SPIE) Conference Series*, volume 10698 of *Society of Photo-Optical Instrumentation Engineers (SPIE) Conference Series*, page 106981Y, August 2018.

[21] The EBEX Collaboration, A. M. Aboobaker, P. Ade, D. Araujo, F. Aubin, C. Baccigalupi, C. Bao, D. Chapman, J. Didier, M. Dobbs, C. Geach, W. Grainger, S. Hanany, K. Helson, S. Hillbrand, J. Hubmayr, A. Jaffe, B. Johnson, T. Jones, J. Klein, A. Korotkov, A. Lee, L. Levinson, M. Limon, K. MacDermid, T. Matsumura, A. D. Miller, M. Milligan, K. Raach, B. Reichborn-Kjennerud, I. Sagiv, G. Savini, L. Spencer, C. Tucker, G. S. Tucker, B. Westbrook, K. Young, and K. Zilic. The EBEX Balloon-borne Experiment – Optics, Receiver, and Polarimetry. *Ap. J. Suppl.*, 239:7, November 2018, 1703.03847.

[22] Y Inoue. *The thermal design of the polarbear-2 experiment*. PhD thesis, Master's thesis, The Graduate University for Advanced Studies, 2012.

[23] Yuki Inoue, Takaho Hamada, Masaya Hasegawa, Masashi Hazumi, Yasuto Hori, Aritoki Suzuki, Takayuki Tomaru, Tomotake Matsumura, Toshifumi Sakata, Tomoyuki Minamoto, et al. Two-layer anti-reflection coating with mullite and polyimide foam for large-diameter cryogenic infrared filters. *Applied optics*, 55(34):D22–D28, 2016.

[24] James W. Lamb. Miscellaneous data on materials for millimetre and submillimetre optics. *International Journal of Infrared and Millimeter Waves*,

17(12):1997–2034, Dec 1996.

[25] V. V. Parshin, R. Heidinger, B. A. Andreev, A. V. Gusev, and V. B. Shmagin. Silicon as an advanced window material for high power gyrotrons. *International Journal of Infrared and Millimeter Waves*, 16(5):863–877, May 1995.

[26] M. V. Jacob, J. Mazierska, K. Leong, and J. Krupka. Microwave properties of low-loss polymers at cryogenic temperatures. *IEEE Transactions on Microwave Theory Techniques*, 50(2):474–480, Feb 2002.

[27] R. Heidinger. Dielectric loss of alumina between 95 and 330 K at ECRH frequencies. *Journal of Nuclear Materials*, 173:243–246, September 1990.

[28] J. Molla, A. Ibarra, J. Margineda, J. M. Zamarro, and A. Hernandez. Dielectric property measurement system at cryogenic temperature and microwave frequencies. *IEEE Transactions on Instrumentation and Measurement*, 42(4):817–821, Aug 1993.

[29] Guglielmo Ventura and Mauro Perfetti. *Thermal Properties of Solids at Room and Cryogenic Temperatures*. Springer, 2014.

[30] Frank Pobell. *Matter and methods at low temperatures*, volume 2. Springer, 2007.

[31] C. L. Choy, E. L. Ong, and F. C. Chen. Thermal diffusivity and conductivity of crystalline polymers. *Journal of Applied Polymer Science*, 26(7):2325–2335, 1981, https://onlinelibrary.wiley.com/doi/pdf/10.1002/app.1981.070260719.

[32] C. J. Glassbrenner and Glen A. Slack. Thermal Conductivity of Silicon and Germanium from 3K to the Melting Point. *Physical Review*, 134(4A):1058–1069, May 1964.

[33] Nist: Properties of solid materials from cryogenic- to room-temperatures.

[34] Max Born and Emil Wolf. *Principles of Optics: Electromagnetic Theory of Propagation, Interference and Diffraction of Light (7th Edition)*. Cambridge University Press, 7th edition, 1999.

[35] A. Gonzalez, Y. Uzawa, K. Kaneko, S. Saito, and Y. Fujii. Improvements in ALMA Band 10 Optics: Influence of IR Filters and Solutions. *IEEE Transactions on Terahertz Science and Technology*, 3:50–55, January 2013.

[36] A. Gonzalez, V. Tapia, R. Finger, C.-D. Huang, S. Asayama, and Y.-D. Huang. ALMA Band 1 Optics (35-50 GHz): Tolerance Analysis, Effect of Cryostat Infrared Filters and Cold Beam Measurements. *Journal of Infrared, Millimeter, and Terahertz Waves, Volume 38, Issue 10, pp.1215-1231*, 38:1215–1231, October 2017.

[37] Sky McKinley and Megan Levine. Cubic spline interpolation. *College of the Redwoods*, 45(1):1049–1060, 1998.

[38] Rolf Schaumann, Mac Elwyn Van Valkenburg, and Haiqiao Xiao. *Design of analog filters*, volume 1. Oxford University Press New York, 2001.

[39] P Marchand and L Marmet. Binomial smoothing filter: A way to avoid some pitfalls of least-squares polynomial smoothing. *Review of scientific instruments*, 54(8):1034–1041, 1983.

[40] PB Clapham and MC Hutley. Reduction of lens reflexion by the "moth eye" principle. *Nature*, 244(5414):281–282, 1973.

[41] Yi-Fan Huang, Surojit Chattopadhyay, Yi-Jun Jen, Cheng-Yu Peng, Tze-An Liu, Yu-Kuei Hsu, Ci-Ling Pan, Hung-Chun Lo, Chih-Hsun Hsu, Yuan-Huei Chang, et al. Improved broadband and quasi-omnidirectional anti-reflection properties with biomimetic silicon nanostructures. *Nature nanotechnology*, 2(12):770–774, 2007.

[42] Federico Lora Gonzalez and Michael J. Gordon. Bio-inspired, sub-wavelength surface structures for ultra-broadband, omni-directional anti-reflection in the mid and far ir. *Opt. Express*, 22(11):12808–12816, Jun 2014.

[43] Claudia Brückner, Boris Pradarutti, Olaf Stenzel, Ralf Steinkopf, Stefan Riehemann, Gunther Notni, and Andreas Tünnermann. Broadband antireflective surface-relief structure for thz optics. *Opt. Express*, 15(3):779–789, Feb 2007.

[44] R. Takaku, S. Hanany, H. Imada, H. Ishino, N. Katayama, K. Komatsu, K. Konishi, M. Kuwata-Gonokami, T. Matsumura, K. Mitsuda, H. Sakurai, Y. Sakurai, Q. Wen, N. Y. Yamasaki, K. Young, and J. Yumoto. Broadband, millimeter-wave anti-reflective structures on sapphire ablated with femto-second laser. *Journal of Applied Physics*, 128(22):225302, 2020, https://doi.org/10.1063/5.0022765.

[45] Philippe Lalanne and Dominique Lemercier-Lalanne. On the effective medium theory of subwavelength periodic structures. *Journal of Modern Optics*, 43(10):2063–2085, 1996.

[46] Hemant Kumar Raut, V. Anand Ganesh, A. Sreekumaran Nair, and Seeram Ramakrishna. Anti-reflective coatings: A critical, in-depth review. *Energy Environ. Sci.*, 4:3779–3804, 2011.

[47] R. W. Klopfenstein. A transmission line taper of improved design. *Proceedings of the IRE*, 44:31 – 35, 1956.

[48] Eric B. Grann, M. G. Moharam, and Drew A. Pommet. Optimal design for antireflective tapered two-dimensional subwavelength grating structures. *J. Opt. Soc. Am. A*, 12(2):333–339, Feb ts.

[49] Rytov, SM. Electromagnetic properties of a finely stratified medium. *SOVIET PHYSICS JETP-USSR*, 2(3):466–475, 1956.

[50] R. Bräuer and O. Bryngdahl. Design of antireflection gratings with approximate and rigorous methods. *Appl. Optics*, 33:7875–7882, December 1994.

[51] Eric B Grann, MG Moharam, and Drew A Pommet. Artificial uniaxial and biaxial dielectrics with use of two-dimensional subwavelength binary gratings. *JOSA A*, 11(10):2695–2703, 1994.

[52] Hisao Kikuta, Yasushi Ohira, Hayao Kubo, and Koichi Iwata. Effective medium theory of two-dimensional subwavelength gratings in the non-quasi-static limit. *JOSA A*, 15(6):1577–1585, 1998.

[53] E. Hecht. *Optics 4th Edition*. Addison-Wesley, 1998.

[54] SR Dicker, PAR Ade, J Aguirre, JA Brevik, HM Cho, R Datta, MJ Devlin, B Dober, D Egan, J Ford, et al. Mustang2: a large focal plan array for the 100 meter green bank telescope. In *Millimeter, Submillimeter, and Far-Infrared Detectors and Instrumentation for Astronomy VII*, volume 9153, page 91530J. International Society for Optics and Photonics, 2014.

[55] H. A. Kishawy and A. Hoseini. *Machining difficult to cut materials: Basic principles and challenges*. 2195-0911. Springer International Publishing, 1 edition, 2019.

[56] L. A. O. Araujo, C. R. Foschini, R. G. Jasinevícius, and C. A. Fortulan. Precision dicing of hard materials with abrasive blade. *The International Journal of Advanced Manufacturing Technology*, 86(9):2885–2894, Oct 2016.

[57] J. Li and G. W. Hastings. *Chapter 5 Oxide Bioceramics: Inert Ceramic Materials in Medicine and Dentistry*, pages 339–352. Springer New York, New York, NY, 2016.

[58] S. Juodkazis, K. Nishimura, H. Misawa, T. Ebisui, R. Waki, S. Matsuo, and T. Okada. Control over the crystalline state

of sapphire. *Advanced Materials*, 18(11):1361–1364, 2006, https://onlinelibrary.wiley.com/doi/pdf/10.1002/adma.200501837.

[59] T. Matsumura, K. Young, Q. Wen, S. Hanany, H. Ishino, Y. Inoue, Hazumi M., J. Koch, H. Suttman, and V. Schütz. Millimeter-wave broadband antireflection coatings using laser ablation of subwavelength structures. *Appl. Opt.*, 55(13):3502–3509, May 2016.

[60] Viktor Schütz, Karl Young, Tomotake Matsumura, Shaul Hanany, Jürgen Koch, Oliver Suttmann, Ludger Overmeyer, and Qi Wen. Laser processing of sub-wavelength structures on sapphire and alumina for millimeter wavelength broadband anti-reflection coatings. *Journal of Laser Micro Nanoengineering*, 11(2):204–209, 1 2016.

[61] T Matsumura, R Takaku, S Hanany, H Imada, H Ishino, N Katayama, Y Kobayashi, K Komatsu, K Konishi, M Kuwata-Gonokami, et al. Prototype demonstration of the broadband anti-reflection coating on sapphire using a sub-wavelength structure. In *29th IEEE International Symposium on Space Terahertz Technology, ISSTT 2018*, pages 26–28, 2018.

[62] T Matsumura, R Takaku, S Hanany, H Imada, H Ishino, N Katayama, Y Kobayashi, K Komatsu, K Konishi, M Kuwata-Gonokami, et al. Prototype demonstration of the broadband anti-reflection coating on sapphire using a sub-wavelength structure. In *29th IEEE International Symposium on Space Terahertz Technology, ISSTT 2018*, pages 26–28, 2018.

[63] R. Takaku, T. Matsumura, H. Sakurai, K. Konishi, H. Imada, S. Hanany, K. Young, Q. Wen, Y. Sakurai, N. Katayama, K. Mitsuda, N. Yamasaki, K. Komatsu, H. Ishino, J. Yumoto, and M. Kuwata-Gonokami. Demonstration of broadband anti-reflection coating on sapphire based on mm-wave sub-wavelength structures. In *2019 44th International Conference on Infrared, Millimeter, and Terahertz Waves (IRMMW-THz)*, pages 1–2, Sep. 2019.

[64] Karl Young, Qi Wen, Shaul Hanany, Hiroaki Imada, Jürgen Koch, Tomotake Matsumura, Oliver Suttmann, and Viktor Schütz. Broadband millimeter-wave anti-reflection coatings on silicon using pyramidal sub-wavelength structures. *Journal of Applied Physics*, 121(21), June 2017.

[65] Qi Wen, Elena Fadeeva, Shaul Hanany, Jrgen Koch, Tomotake Matsumura, Ryota Takaku, and Karl Young. Picosecond laser ablation of millimeter-wave subwavelength structures on alumina and sapphire. *Optics & Laser Technology*, 142:107207, 2021.

[66] Rafael R Gattass and Eric Mazur. Femtosecond laser micromachining in transparent materials. *Nature photonics*, 2(4):219–225, 2008.

[67] Roger H. French. Electronic Band Structure of Al2O3, with Comparison to Alon and AIN. *Journal of the American Ceramic Society*, 73(3):477–489, 1990, https://ceramics.onlinelibrary.wiley.com/doi/pdf/10.1111/j.1151-2916.1990.tb06541.x.

[68] B. C. Stuart, M. D. Feit, S. Herman, A. M. Rubenchik, B. W. Shore, and M. D. Perry. Nanosecond-to-femtosecond laser-induced breakdown in dielectrics. *Phys. Rev. B*, 53:1749–1761, Jan 1996.

[69] Daniel Nieto, Justo Arines, Gerard M O'Connor, and María Teresa Flores-Arias. Single-pulse laser ablation threshold of borosilicate, fused silica, sapphire, and soda-lime glass for pulse widths of 500 fs, 10 ps, 20 ns. *Applied optics*, 54(29):8596–8601, 2015.

[70] Laurent Gallais, D-B Douti, Mireille Commandre, G Batavičiūtė, Egidjus Pupka, M Ščiuka, Linas Smalakys, Valdas Sirutkaitis, and A Melninkaitis. Wavelength dependence of femtosecond laser-induced damage threshold of optical materials. *Journal of Applied Physics*, 117(22):223103, 2015.

[71] Zhanliang Sun, Matthias Lenzner, and Wolfgang Rudolph. Generic incubation law for laser damage and ablation thresholds. *Journal of Applied Physics*, 117(7):073102, 2015.

[72] JM Liu. Simple technique for measurements of pulsed gaussian-beam spot sizes. *Optics letters*, 7(5):196–198, 1982.

[73] Ting-Hsuan Chen, Romain Fardel, and Craig B Arnold. Ultrafast z-scanning for high-efficiency laser micro-machining. *Light: Science & Applications*, 7(4):17181–17181, 2018.

[74] Jianhui Su, Caiwang Tan, Zhuolun Wu, Laijun Wu, Xiangtao Gong, Bo Chen, Xiaoguo Song, and Jicai Feng. Influence of defocus distance on laser joining of cfrp to titanium alloy. *Optics & Laser Technology*, 124:106006, 2020.

[75] Gangxian Zhu, Dichen Li, Anfeng Zhang, Gang Pi, and Yiping Tang. The influence of laser and powder defocusing characteristics on the surface quality in laser direct metal deposition. *Optics & Laser Technology*, 44(2):349–356, 2012.

[76] University Imaging Center, University of Minnesota.

[77] Mary Lou P. Bailey, Andrew T. Pierce, Aaron J. Simon, Devin T. Edwards, Gerald J. Ramian, Nikolay I. Agladze, and Mark S. Sherwin. Narrow-band water-based absorber with high return loss for terahertz spectroscopy. *IEEE Transactions on Terahertz Science and Technology*, 5(6):961–966, 2015.

[78] Joerg Schille, Lutz Schneider, Andrè Streek, Sascha Kloetzer, and Udo Loeschner. High-throughput machining using a high-average power ultrashort pulse laser and high-speed polygon scanner. *Optical Engineering*, 55(9):1 – 10, 2016.

[79] Uli Engelhardt, Jens Hildenhagen, and Klaus Dickmann. Micromachining using high-power picosecond lasers. *Laser Technik Journal*, 8(5):32–35, 2011, https://onlinelibrary.wiley.com/doi/pdf/10.1002/latj.201190056.

[80] P Balling and J Schou. Femtosecond-laser ablation dynamics of dielectrics: basics and applications for thin films. *Reports on Progress in Physics*, 76(3):036502, feb 2013.

[81] Baerbel Rethfeld, Dmitriy S Ivanov, Martin E Garcia, and Sergei I Anisimov. Modelling ultrafast laser ablation. *Journal of Physics D: Applied Physics*, 50(19):193001, apr 2017.

[82] J. Furmanski, A. M. Rubenchik, M. D. Shirk, and B. C. Stuart. Deterministic processing of alumina with ultrashort laser pulses. *Journal of Applied Physics*, 102(7):073112, 2007, https://doi.org/10.1063/1.2794376.

[83] G. Raciukaitis, M. Brikas, Paulius Gecys, Bogdan Voisiat, and Mindaugas Gedvilas. Use of high repetition rate and high power lasers in microfabrication: How to keep the efficiency high? *Journal of Laser Micro / Nanoengineering*, 4, 12 2009.

[84] B. Neuenschwander, B. Jaeggi, M. Schmid, and G. Hennig. Surface structuring with ultra-short laser pulses: Basics, limitations and needs for high throughput. *Physics Procedia*, 56:1047 – 1058, 2014. 8th International Conference on Laser Assisted Net Shape Engineering LANE 2014.

[85] P. Boerner, M. Hajri, T. Wahl, J. Weixler, and K. Wegener. Picosecond pulsed laser ablation of dielectric rods: Angle-dependent ablation process model for laser micromachining. *Journal of Applied Physics*, 125(23):234902, 2019, https://doi.org/10.1063/1.5092812.

[86] Gediminas Raciukaitis, Marijus Brikas, and Mindaugas Gedvilas. Efficiency aspects in processing of metals with high-repetition-rate ultra-short-pulse

lasers. *International Congress on Applications of Lasers & Electro-Optics*, 2008(1):M403, 2008, https://lia.scitation.org/doi/pdf/10.2351/1.5061377.

[87] Beat Neuenschwander, Guido F. Bucher, Christian Nussbaum, Benjamin Joss, Martin Muralt, Urs W. Hunziker, and Peter Schuetz. Processing of metals and dielectric materials with ps-laserpulses: results, strategies, limitations and needs. In Hiroyuki Niino, Michel Meunier, Bo Gu, Guido Hennig, and Jan J. Dubowski, editors, *Laser Applications in Microelectronic and Optoelectronic Manufacturing XV*, volume 7584, pages 99 – 112. International Society for Optics and Photonics, SPIE, 2010.

[88] B. Jaeggi, B. Neuenschwander, M. Schmid, M. Muralt, J. Zuercher, and U. Hunziker. Influence of the pulse duration in the ps-regime on the ablation efficiency of metals. *Physics Procedia*, 12:164 – 171, 2011. Lasers in Manufacturing 2011 - Proceedings of the Sixth International WLT Conference on Lasers in Manufacturing.

[89] Beat Neuenschwander, Beat Jaeggi, Marc Schmid, Vincent Rouffiange, and Paul-E. Martin. Optimization of the volume ablation rate for metals at different laser pulse-durations from ps to fs. In Guido Hennig, Xianfan Xu, Bo Gu, and Yoshiki Nakata, editors, *Laser Applications in Microelectronic and Optoelectronic Manufacturing (LAMOM) XVII*, volume 8243, pages 43 – 55. International Society for Optics and Photonics, SPIE, 2012.

[90] S Preuss, A Demchuk, and M Stuke. Sub-picosecond uv laser ablation of metals. *Applied physics A*, 61(1):33–37, 1995.

[91] Stefan Nolte, Cl Momma, H Jacobs, A Tünnermann, Boris N Chichkov, Bernd Wellegehausen, and Herbert Welling. Ablation of metals by ultrashort laser pulses. *JOSA B*, 14(10):2716–2722, 1997.

[92] MJJ Schmidt, DKY Low, and L Li. Laser ablation of a b4c–polysiloxane composite. *Applied surface science*, 186(1-4):271–275, 2002.

[93] D Eversole, B Luk'yanchuk, and A Ben-Yakar. Plasmonic laser nanoablation of silicon by the scattering of femtosecond pulses near gold nanospheres. *Applied Physics A*, 89(2):283–291, 2007.

[94] Adela Ben-Yakar and Robert L Byer. Femtosecond laser ablation properties of borosilicate glass. *Journal of applied physics*, 96(9):5316–5323, 2004.

[95] Sophocles J. Orfanidis. *Electromagnetic Waves and Antennas*. Online, http://eceweb1.rutgers.edu/ orfanidi/ewa/, 2016. Accessed 31 Dec 2020.

[96] Edward D Palik. *Handbook of optical constants of solids*, volume 3. Academic press, 1998.

[97] S Küper and M Stuke. Femtosecond uv excimer laser ablation. *Applied Physics B*, 44(4):199–204, 1987.

[98] S. Preuss, M. Späth, Y. Zhang, and M. Stuke. Time resolved dynamics of subpicosecond laser ablation. *Applied Physics Letters*, 62(23):3049–3051, 1993, https://doi.org/10.1063/1.109135.

[99] D. Puerto, J. Siegel, W. Gawelda, M. Galvan-Sosa, L. Ehrentraut, J. Bonse, and J. Solis. Dynamics of plasma formation, relaxation, and topography modification induced by femtosecond laser pulses in crystalline and amorphous dielectrics. *J. Opt. Soc. Am. B*, 27(5):1065–1076, May 2010.

[100] William H Press, H William, Saul A Teukolsky, William T Vetterling, A Saul, and Brian P Flannery. *Numerical recipes 3rd edition: The art of scientific computing*. Cambridge university press, 2007.

[101] D. Ashkenasi, R. Stoian, and A. Rosenfeld. Single and multiple ultrashort laser pulse ablation threshold of Al2O3 (corundum) at different etch phases. *Applied Surface Science*, 154-155:40 – 46, 2000.

[102] Daniel Nieto, Justo Arines, Gerard M. O'Connor, and María Teresa Flores-Arias. Single-pulse laser ablation threshold of borosilicate, fused silica, sapphire, and soda-lime glass for pulse widths of 500 fs, 10 ps, and 20 ns. *Appl. Opt.*, 54(29):8596–8601, Oct 2015.

[103] W. Perrie, A. Rushton, M. Gill, P. Fox, and W. O'Neill. Femtosecond laser micro-structuring of alumina ceramic. *Applied Surface Science*, 248(1):213 – 217, 2005. 4th International Conference on Photo-Excited Processes and Applications.

[104] X. L. Mao, W. T. Chan, M. A. Shannon, and R. E. Russo. Plasma shielding during picosecond laser sampling of solid materials by ablation in he versus ar atmosphere. *Journal of Applied Physics*, 74(8):4915–4922, 1993, https://doi.org/10.1063/1.354325.

[105] R. Vilar, S.P. Sharma, A. Almeida, L.T. Cangueiro, and V. Oliveira. Surface morphology and phase transformations of femtosecond laser-processed sapphire. *Applied Surface Science*, 288:313 – 323, 2014.

[106] M E Shaheen, J E Gagnon, and B J Fryer. Experimental study on 785 nm femtosecond laser ablation of sapphire in air. *Laser Physics Letters*, 12(6):066103, apr 2015.

[107] Shaul Hanany, Marcelo Alvarez, Emmanuel Artis, Peter Ashton, Jonathan Aumont, Ragnhild Aurlien, Ranajoy Banerji, R. Belen Barreiro, James G. Bartlett, Soumen Basak, Nick Battaglia, Jamie Bock, Kimberly K. Boddy, Matteo Bonato, Julian Borrill, François Bouchet, François Boulanger, Blakesley Burkhart, Jens Chluba, David Chuss, Susan E. Clark, Joelle Cooperrider, Brendan P. Crill, Gianfranco De Zotti, Jacques Delabrouille, Eleonora Di Valentino, Joy Didier, Olivier Doré, Hans K. Eriksen, Josquin Errard, Tom Essinger-Hileman, Stephen Feeney, Jeffrey Filippini, Laura Fissel, Raphael Flauger, Unni Fuskeland, Vera Gluscevic, Krzysztof M. Gorski, Dan Green, Brandon Hensley, Diego Herranz, J. Colin Hill, Eric

Hivon, Renée Hložek, Johannes Hubmayr, Bradley R. Johnson, William Jones, Terry Jones, Lloyd Knox, Al Kogut, Marcos López-Caniego, Charles Lawrence, Alex Lazarian, Zack Li, Mathew Madhavacheril, Jean-Baptiste Melin, Joel Meyers, Calum Murray, Mattia Negrello, Giles Novak, Roger O'Brient, Christopher Paine, Tim Pearson, Levon Pogosian, Clem Pryke, Giuseppe Puglisi, Mathieu Remazeilles, Graca Rocha, Marcel Schmittfull, Douglas Scott, Peter Shirron, Ian Stephens, Brian Sutin, Maurizio Tomasi, Amy Trangsrud, Alexander van Engelen, Flavien Vansyngel, Ingunn K. Wehus, Qi Wen, Siyao Xu, Karl Young, and Andrea Zonca. PICO: Probe of Inflation and Cosmic Origins. *arXiv e-prints*, page arXiv:1902.10541, Feb 2019, 1902.10541.

[108] J. M. Lamarre, J. L. Puget, F. Bouchet, P. A. R. Ade, A. Benoit, J. P. Bernard, J. Bock, P. De Bernardis, J. Charra, F. Couchot, J. Delabrouille, G. Efstathiou, M. Giard, G. Guyot, A. Lange, B. Maffei, A. Murphy, F. Pajot, M. Piat, I. Ristorcelli, D. Santos, R. Sudiwala, J. F. Sygnet, J. P. Torre, V. Yurchenko, and D. Yvon. The Planck High Frequency Instrument, a 3rd generation CMB experiment, and a full sky submillimeter survey. In S. Hanany and K. A. Olive, editors, *the proceedings of the workshop on "The Cosmic Microwave Background and its Polarization," New Astronomy Reviews*. Elsevier, 2003. astro-ph/0308075.

[109] Decadal Survey on Astronomy and Astrophysics 2020 (Astro2020).

[110] C. Dragone. Offset Multireflector Antennas with Perfect Pattern Symmetry and Polarization Discrimination. *Bell Syst. Tech. J.*, 57:2663–2684, 178.

[111] C. Dragone. A First-Order Treatment of Aberrations in Cassegrainian and Gregorian antennas. *IEEE Transactions on Antennas and Propagation*, 30(3):331–339, 1982.

[112] C. Dragone. First-Order Correction of Aberrations in Cassegrainian and

Gregorian antennas. *IEEE Transactions on Antennas and Propagation*, 31:764–775, 1983.

[113] J. Bock, A. Aljabri, A. Amblard, D. Baumann, M. Betoule, T. Chui, L. Colombo, A. Cooray, D. Crumb, P. Day, C. Dickinson, D. Dowell, M. Dragovan, S. Golwala, K. Gorski, S. Hanany, W. Holmes, K. Irwin, B. Johnson, B. Keating, C.-L. Kuo, A. Lee, A. Lange, C. Lawrence, S. Meyer, N. Miller, H. Nguyen, E. Pierpaoli, N. Ponthieu, J.-L. Puget, J. Raab, P. Richards, C. Satter, M. Seiffert, M. Shimon, H. Tran, B. Williams, and J. Zmuidzinas. Study of the Experimental Probe of Inflationary Cosmology (EPIC)-Intemediate Mission for NASA's Einstein Inflation Probe. *ArXiv e-prints*, June 2009, 0906.1188.

[114] Huan Tran, Brad Johnson, Mark Dragovan, James Bock, Abdullah Aljabri, Alex Amblard, Daniel Bauman, Marc Betoule, Talso Chui, Loris Colombo, et al. Optical design of the epic-im crossed dragone telescope. In *Space Telescopes and Instrumentation 2010: Optical, Infrared, and Millimeter Wave*, volume 7731, page 77311R. International Society for Optics and Photonics, 2010.

[115] Karl Young, Marcelo Alvarez, Nicholas Battaglia, Jamie Bock, Jullian Borrill, David Chuss, Brendan Crill, Jacques Delabrouille, Mark Devlin, Laura Fissel, Raphael Flauger, Daniel Green, Kris Gorski, Shaul Hanany, Richard Hills, Johannes Hubmayr, Bradley Johnson, William Jones, Lloyd Knox, Alan Kogut, Charles Lawrence, Tomotake Matsumura, James McGuire, Jeff McMahon, Roger O'Brient, Clement Pryke, Brian M. Sutin, Xin Zhi Tan, Amy Trangsrud, Qi Wen, and Gianfranco De Zotti. Optical design of PICO: a concept for a space mission to probe inflation and cosmic origins. In Makenzie Lystrup, Howard A. MacEwen, Giovanni G. Fazio, Natalie Batalha, Nicholas Siegler, and Edward C. Tong, editors, *Space Telescopes and Instrumentation 2018: Optical, Infrared, and Millimeter Wave*, volume

10698, pages 1242 – 1253. International Society for Optics and Photonics, SPIE, 2018.

[116] CodeV, Synopsys.

[117] Space Exploration Technologies Corp. *Falcon 9 Launch Vehicle: Payload User's Guide, Rev 2*. Space Exploration Technologies Corp., October 2015.

[118] J. Delabrouille et al. Exploring cosmic origins with CORE: Survey requirements and mission design. *JCAP*, 4:014, April 2018, 1706.04516.

[119] Hajime Sugai, Shingo Kashima, Kimihiro Kimura, Tomotake Matsumura, Masanori Inoue, Makoto Ito, Toshiyuki Nishibori, Yutaro Sekimoto, Hirokazu Ishino, Yuki Sakurai, et al. Optical designing of litebird. In *Space Telescopes and Instrumentation 2016: Optical, Infrared, and Millimeter Wave*, volume 9904, page 99044H. International Society for Optics and Photonics, 2016.

[120] Jon E. Gudmundsson, Patricio A. Gallardo, Roberto Puddu, Simon R. Dicker, Alexandre E. Adler, Aamir M. Ali, Andrew Bazarko, Grace E. Chesmore, Gabriele Coppi, Nicholas F. Cothard, Nadia Dachlythra, Mark Devlin, Rolando Dünner, Giulio Fabbian, Nicholas Galitzki, Joseph E. Golec, Shuay-Pwu Patty Ho, Peter C. Hargrave, Anna M. Kofman, Adrian T. Lee, Michele Limon, Frederick T. Matsuda, Philip D. Mauskopf, Kavilan Moodley, Federico Nati, Michael D. Niemack, John Orlowski-Scherer, Lyman A. Page, Bruce Partridge, Giuseppe Puglisi, Christian L. Reichardt, Carlos E. Sierra, Sara M. Simon, Grant P. Teply, Carole Tucker, Edward J. Wollack, Zhilei Xu, and Ningfeng Zhu. The simons observatory: modeling optical systematics in the large aperture telescope. *Appl. Opt.*, 60(4):823–837, Feb 2021.

[121] Ray Radebaugh. Thermal conductance of indium solder joints at low temperatures. *Review of Scientific Instruments*, 48(1):93–94, 1977.

[122] Ronald J Sladek. Thermal conductivity of indium-thallium alloys at low temperatures. *Physical Review*, 97(4):902, 1955.

[123] AP King. The radiation characteristics of conical horn antennas. *Proceedings of the IRE*, 38(3):249–251, 1950.

[124] Aritoki Suzuki. *Multichroic bolometric detector architecture for cosmic microwave background polarimetry experiments*. University of California, Berkeley, 2013.

[125] Johannes Staguhn, Samuel H Moseley, Ari Brown, Gene Hilton, Kent Irwin, Stephen Maher, Karwan Rostem, Elmer Sharp, and Edward Wollack. Development of a robust, efficient process to produce scalable, superconducting kilopixel far-ir detector arrays. In *Millimeter, Submillimeter, and Far-Infrared Detectors and Instrumentation for Astronomy IX*, volume 10708, page 107081V. International Society for Optics and Photonics, 2018.

[126] A Suzuki, Peter AR Ade, Yoshiki Akiba, D Alonso, K Arnold, J Aumont, C Baccigalupi, D Barron, S Basak, S Beckman, et al. The litebird satellite mission: Sub-kelvin instrument. *Journal of Low Temperature Physics*, 193(5):1048–1056, 2018.

[127] Joshua A Sobrin, PAR Ade, Zeeshan Ahmed, AJ Anderson, JS Avva, R Basu Thakur, AN Bender, BA Benson, JE Carlstrom, FW Carter, et al. Design and characterization of the spt-3g receiver. In *Millimeter, Submillimeter, and Far-Infrared Detectors and Instrumentation for Astronomy IX*, volume 10708, page 107081H. International Society for Optics and Photonics, 2018.

[128] Frank Pobell. *Matter and methods at low temperatures*, volume 2. Springer, 2007.

[129] L Pagano, J-M Delouis, S Mottet, J-L Puget, and L Vibert. Reionization

optical depth determination from planck hfi data with ten percent accuracy. *Astronomy & Astrophysics*, 635:A99, 2020.

[130] N. Aghanim, Y. Akrami, M. Ashdown, J. Aumont, C. Baccigalupi, M. Ballardini, A. J. Banday, R. B. Barreiro, N. Bartolo, and et al. Planck 2018 results. *Astronomy & Astrophysics*, 641:A6, Sep 2020.

[131] D. J. Watts, G. E. Addison, C. L. Bennett, and J. L. Weiland. Beyond optical depth: Future determination of ionization history from the cosmic microwave background. *The Astrophysical Journal*, 889(2):130, jan 2020.

[132] John P Nibarger, James A Beall, Dan Becker, Joe Britton, Hsiao-Mei Cho, Anna Fox, Gene C Hilton, Johannes Hubmayr, Dale Li, Jeff McMahon, et al. An 84 pixel all-silicon corrugated feedhorn for cmb measurements. *Journal of Low Temperature Physics*, 167(3):522–527, 2012.

[133] RJ Wylde. Millimetre-wave gaussian beam-mode optics and corrugated feed horns. In *IEE Proceedings H (Microwaves, Optics and Antennas)*, volume 131, pages 258–262. IET, 1984.

[134] François Aubin, Shaul Hanany, Bradley R Johnson, Adrian Lee, Aritoki Suzuki, Benjamin Westbrook, and Karl Young. Developments of highly multiplexed, multi-chroic pixels for balloon-borne platforms. *Journal of Low Temperature Physics*, 193(3):298–304, 2018.

[135] Kate Raach. *Characterization, Optimization, and Operation of TES Bolometers for EBEX*. PhD thesis, University of Minnesota, 2018.

Appendix A

Glossary and Acronyms

Care has been taken in this thesis to minimize the use of jargon and acronyms, but this cannot always be achieved. This appendix contains a list of acronyms and their meaning.

A.1 Acronyms

ARC anti-reflection coatings

CMB cosmic microwave background

CGI continuous-gradient index

DLFOV diffraction-limited field of view

EM electromagnetic

FZ Floating-zone

HDPE high density polyethylene

HIM high-index materials

HWP half-wave plate

LZH Lazer Zentrum Hannover

MCP multi-color pixel

MPI multi-photon ionization

MSM millimeter and sub-millimeter

NET noise equivalent temperature

SAMP sinuous antenna multichroic pixel

SWS sub-wavelength structures

TES transition edge sensor

TDM time-domain multiplexer

TMM Transfer Matrix Method

UMN University of Minnesota